Copyright

by

Zhuang Sun

2019

The Dissertation Committee for Zhuang Sun Certifies that this is the approved version of the following Dissertation:

INVESTIGATION OF COUPLED CHEMO-HYDRO-MECHANICAL PROCESSES WITH DISCRETE ELEMENT MODELING

Committee:

Matthew T. Balhoff, Supervisor

D. Nicolas Espinoza, Co-Supervisor

Maša Prodanović

John T. Foster

Somnath Mondal

INVESTIGATION OF COUPLED CHEMO-HYDRO-MECHANICAL PROCESSES WITH DISCRETE ELEMENT MODELING

by

Zhuang Sun

Dissertation

Presented to the Faculty of the Graduate School of

The University of Texas at Austin

in Partial Fulfillment

of the Requirements

for the Degree of

DOCTOR OF PHILOSOPHY

The University of Texas at Austin

August 2019

Dedication

To my wife Hewei Tang

Acknowledgements

I would like to express my deepest appreciation to my advisors, Drs. Matthew Balhoff and Nicolas Espinoza for their strong support and excellent guidance during my PhD program. They taught me not only how to become a good scholar but also a better human being. Without their help and encouragement, this work would not have been possible. I would like to extend my deepest gratitude to my committee members, Drs. Maša Prodanović, John Foster and Somnath Mondal for their valuable comments and advice, and their time going through this dissertation.

Special thanks go to Dr. Thomas Dewers for providing me with the idea of DEM modeling of indentation test, Drs. John Killough and Hewei Tang for the valuable discussions on the depletion-induced grain crushing and reservoir compaction, Dr. Hongtao Yang for sharing his expertise and ideas on the pore-scale simulations with me, Jenny Ryu for sharing her coupled-geomechanics reservoir model, and Xiaojin Zheng for the insightful discussions on clay smear and fault reactivation.

I want to acknowledge the Center for Frontiers of Subsurface Energy Security and the ExxonMobil Upstream Research Company for providing financial support. I also want to acknowledge the high performance computing system from Texas Advanced Computing Center (TACC).

I would like to thank my colleagues Pengpeng Qi, Ke Xu, Peixi Zhu, Yujing Du, Miguel Mejia, Lucas Mejia, James Riddle, Yashar Mehmani, Alex Cui, Chiyu Xie, Shayan Tavassoli, Zihao Li, Moises Velasco, and my good friends Rencheng Dong, Peidong Zhao, Han Jiang, and many others I do not cite explicitly.

Finally, I take this opportunity to express the gratitude to my wife, Dr. Hewei Tang. I cannot be where I am today without you! Thank you so much for always providing me with unconditional support and love!

Abstract

INVESTIGATION OF COUPLED CHEMO-HYDRO-MECHANICAL PROCESSES WITH DISCRETE ELEMENT MODELING

Zhuang Sun, Ph.D.

The University of Texas at Austin, 2019

Supervisors: Matthew T. Balhoff and D. Nicolas Espinoza

Geological storage of CO_2 is proposed as a near-term economically viable approach to mitigate CO_2 emissions, and is an example of the coupled chemo-hydro-mechanical processes. Although CO_2 injection and enhanced oil recovery are viewed as mature technologies in the oil and gas industry, investigation of all possible implications is necessary for secure and effective long-term CO_2 storage. The injection of a large volume of CO_2 into target storage formations is usually associated with a number of geomechanical processes that are initiated at the pore scale. Therefore, a pore-scale geomechanical model, i.e. Discrete Element Method (DEM), is of great importance to better understand the underlying pore-scale processes and mechanisms that govern the large-scale CO_2 geological storage. In this work, we concentrate on several significant pore-scale coupled phenomena.

Firstly, CO_2 injection into geological formations involves chemo-mechanical processes and shifts the geochemical equilibrium between the minerals and resident brine, which subsequently induces mineral-brine-CO_2 reactions and affects CO_2 storage mechanical integrity. We utilize a numerical model that couples the Discrete Element

Method (DEM) and the Bonded-Particle Model (BPM) to perform simulations on synthetic rocks that mimic tested rock samples. Numerical results, in agreement with experimental evidence, show that both cement and particle dissolution significantly contribute to rock weakening in sandstones with carbonate/hematite cements and pore-filling carbonate.

Secondly, reservoir compaction involves hydro-mechanical processes that induce changes in porosity and permeability, and is a significant concern for the oil and gas production. We develop a grain crushing model based on the DEM to investigate the changes in porosity and permeability under the reservoir stress path. Grain crushing is shown to be the dominant mechanism for significant changes in porosity and permeability under a high effective stress. Samples consisting of large and soft grains tend to be more readily compacted.

Finally, fluid injection in the subsurface may induce fractures and is another common hydro-mechanical process. We couple the Discrete Element Method (DEM) to solve for the mechanics of a solid granular medium and the Computational Fluid Dynamics (CFD) to model fluid flow and drag forces. We validate the resolved CFD-DEM numerical model against experiments from the literature and investigate the impact of physical properties and injection parameters. This work reveals how the pore-scale processes contribute to fluid-driven fracture initiation.

Table of Contents

List of Tables

List of Figures

Chapter 1: Introduction

Geological CO_2 storage is a technology proposed to curb anthropogenic greenhouse gas emissions into the atmosphere. Deep sedimentary formations, such as oil and gas depleted reservoirs and deep saline aquifers, have been recognized as suitable geological targets with sufficient capacity and injectivity (Bachu, 2008; Benson and Cole, 2008; Bickle, 2009). Recent experience including pilot projects and commercial operations has demonstrated the feasibility of CO_2 sequestration in deep sedimentary formations (Michael et al., 2010). Nevertheless, securing a large volume of CO_2 will require a deep understanding of the complex physical processes that govern the long-term effective CO_2 storage (Rutqvist et al., 2016).

The injection of a large volume of CO_2 into deep sedimentary formations may be associated with a number of geomechanical processes (Rutqvist, 2012). Concerns of these geomechanical processes originated in the early 1990s (Holloway and Savage, 1993). Later, some CO_2 injection sites, for instance the In Salah CO_2 storage project in Algeria, exhibited significant geomechanical changes as a result of the pressure disturbance and site-specific geomechanical conditions (White, 2009; Rutqvist et al., 2010; Zhou et al., 2010; Verdon et al., 2011). A number of studies indicated that geomechanics could be the major concern for a large-scale CO_2 storage (Rutqvist and Tsang, 2002; Streit and Hillis, 2004; Hawkes et al., 2005). Geomechanical aspects, including reservoir stress and strain, well integrity, ground surface deformation, fracture initiation and propagation, fault reactivation and notable seismic events, are critical for a secure long-term CO_2 storage (Rutqvist, 2012). Therefore, it is of great importance to perform the geomechanical risk assessment at the early stage of CO_2 injection.

Geomechanical modeling is an important approach to reveal and predict the mechanical behavior of rocks. All geomechanical processes are initiated at the pore scale. However, it is impossible to solve the pore-scale governing equations at the field scale (Fig. 1.1). Hence, a continuum formulation based on spatial length scales much larger than pore sizes (i.e. representative elemental volume) is often necessary, which requires various constitutive parameters accounting the aggregate effect of pore-scale processes. One of the goals of a pore-scale study is to obtain these constitutive parameters (e.g. permeability). Other goals are to identify critical parameters and processes, which control macroscopic phenomena and to validate the continuum formulation that can approximate the pore-scale results. It is generally recognized that the CO_2 storage in the subsurface involves the interactions between chemo-hydro-mechanical fields (Rutqvist et al., 2002; Zhang et al., 2016). However, it still remains challenging to characterize these processes due to a lack of knowledge regarding the underlying mechanisms. The pore-scale model employed in this study not only reveals the involved pore-scale phenomena during CO_2 geological storage but provides continuum simulations with constitutive parameters emerging from pore-scale behavior.

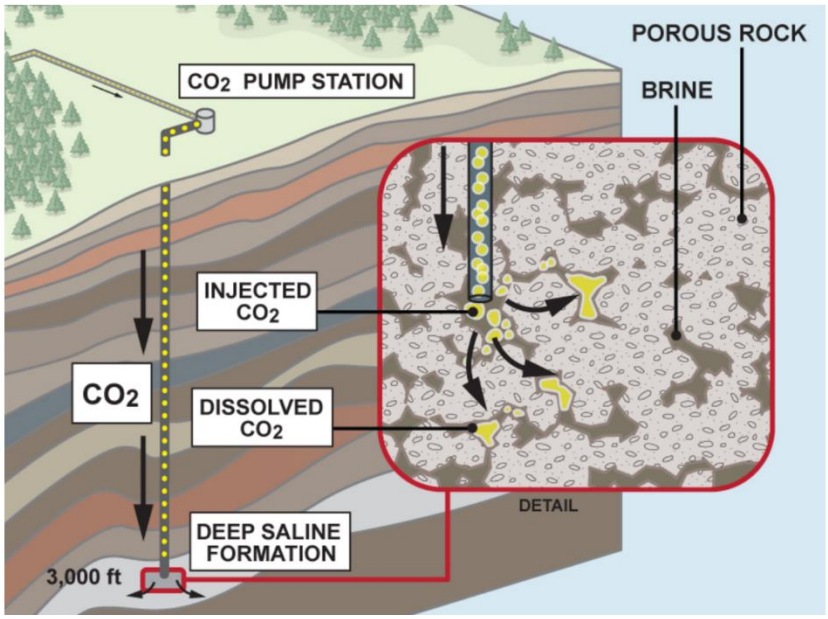

Figure 1.1: Schematic of field- and pore-scale CO_2 storage in deep saline formation (Source: Clean Air Task Force).

In this study, we focus on several significant pore-scale phenomena. Firstly, the injected CO_2 compared to other geological storage facilities (e.g. natural gas) tends to dissolve in the resident reservoir pore fluid and that results in complex interactions between the injected CO_2, the brine in the pore space, and the rock minerals (Rohmer et al., 2016). These chemical reactions may jeopardize the structural integrity of reservoir and caprock formations by altering the petrophysical and geomechanical properties such as rock permeability and strength (Rutqvist and Tsang, 2002; Renard et al., 2008; Espinoza et al., 2011; Rinehart et al., 2016). Therefore, we will develop a pore-scale model to investigate the underlying mechanisms of CO_2-related chemo-mechanical alteration in sandstones. Secondly, reservoir compaction induces changes in porosity and permeability and is a significant concern for the oil and gas production. The reservoir compaction manifests through various pore-scale processes. Grain slippage and rotation commonly occur at low

stress levels. Ductile/soft grains may experience changes in grain shape and brittle grains can fracture at high stress levels (Taylor, 1950; Gallagher et al., 1974; Zhang et al., 1990; Davies and Davies, 2001). Grain fracturing/crushing results in plastic compaction and an irreversible decrease in porosity (Menéndez et al., 1996; Wong and Baud, 1999). We will develop a pore-scale model of grain crushing to investigate the effects of reservoir compaction on porosity and permeability. Finally, the fluid injection results in fluid overpressure and a change of stress state in target formations, which may in turn drive the fluid to migrate through porous media and induce fractures. The injection-induced fracturing is a complicated phenomenon that depends on physical properties and operational parameters. Better understandings of these parameters are necessary to a number of engineering applications. We will investigate the fluid-driven fracture initiation based on pore-scale fluid-rock interactions.

This dissertation is organized as follows: chapter 2 presents sufficient background and literature review. In chapter 3, we investigate the pore-scale mechanisms of CO_2-related chemo-mechanical rock alteration through numerical modeling of indentation tests. The effects of microscopic parameters such as the cement micromechanical properties are discussed in detail. In chapter 4, we present a pore-scale model to simulate micro-scratch tests and analyze the mechanical behavior of cemented sandstone susceptible to grain cement dissolution. In chapter 5, we quantify the reservoir rock chemo-mechanical alteration by triaxial tests and show the large-scale implications of mineral dissolution under subsurface storage conditions. In chapter 6, we propose a pore-scale model of grain crushing and investigate how the reservoir compaction induces changes in porosity and permeability. Chapter 7 presents a pore-scale fracture initiation model to perform numerical simulations of fluid injection into granular media. We discuss the mechanisms of fracture initiation at the pore scale and investigate the effects of fluid viscosity, grain

micromechanical properties and principal stresses on fracture initiation. Chapter 8 covers general conclusions and provides recommendations for future work. The appendices include additional supplementary material for readers.

Chapter 2: Background and Literature Review

2.1 GEOMECHANICS OVERVIEW

We present a geomechanics overview for readers unfamiliar with this area. The concepts introduced as below are widely used in continuum models, e.g. Finite Element Method (FEM). On the contrary, the Discrete Element Method (DEM) treats these macroscopic behaviors are emergent features from simple interactions at the grain scale. Compared to the continuum models, the DEM can (1) capture the granular nature of rocks, (2) characterize discontinuities with spacing comparable to the problem length scale, and (3) capture the evolution of micromechanical processes (e.g. microcracks).

2.1.1 Elasticity

Elasticity is the ability of materials to resist and recover from deformations due to external forces. The theory of elasticity involves the concepts of stress and strain. Constitutive laws describe the material deformation in response to an applied stress. The simplest response is linear elasticity that is a linear relationship between the stress and the strain. Reservoir rocks usually contain fluid in the pore space. The theory of poroelasticity is necessary to describe the behavior of such materials.

2.1.1.2 Stress

Stress is defined as the internal force divided by the cross-sectional area on which it acts. The stress tensor identifies the stresses acting on surfaces oriented in three orthogonal directions and fully describes the stress state at a point. Fig. 2.1 shows the stress components in two dimensions: σ_x and σ_y are normal stress, τ_{xy} and τ_{yx} are shear stress. The first subscript is the face normal and the second subscript is the force direction. With no

net translational or rotational force exerting on the square, shear stress τ_{xy} is equal to τ_{yx}. The stress tensor with all nine components at a point is shown as:

$$\begin{pmatrix} \sigma_x & \tau_{xy} & \tau_{xz} \\ \tau_{yx} & \sigma_y & \tau_{yz} \\ \tau_{zx} & \tau_{zy} & \sigma_z \end{pmatrix} \tag{2.1}$$

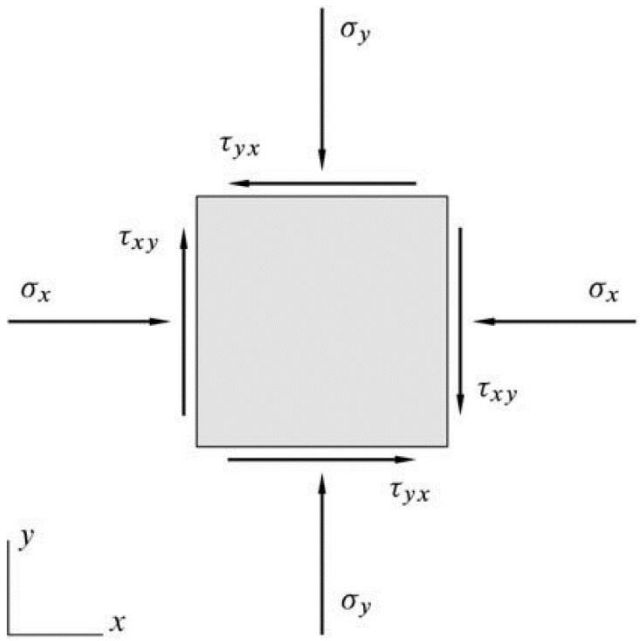

Figure 2.1: Stress components in two dimensions (Fjar et al., 2008).

For a coordinate system with special orientations, all shear components in the stress tensor vanish and that yields principal stresses (Eq. 2.2). The special orientation is called the principal axes of stress. For a simple 2D condition, the principal stresses σ_1 and σ_2 are defined as Eq. 2.3 and 2.4.

$$\begin{pmatrix} \sigma_x & \tau_{xy} \\ \tau_{yx} & \sigma_y \end{pmatrix} \rightarrow \begin{pmatrix} \sigma_1 & 0 \\ 0 & \sigma_2 \end{pmatrix} \tag{2.2}$$

$$\sigma_1 = \frac{1}{2}(\sigma_x + \sigma_y) + \sqrt{\tau_{xy}^2 + \frac{1}{4}(\sigma_x - \sigma_y)^2} \tag{2.3}$$

$$\sigma_2 = \frac{1}{2}(\sigma_x + \sigma_y) - \sqrt{\tau_{xy}^2 + \frac{1}{4}(\sigma_x - \sigma_y)^2} \tag{2.4}$$

The coordinate system is usually reoriented such that the x- and y-axes are parallel to the principal axes of stress. The stresses σ and τ in a direction θ with respective to the x-axis are given by Eq. 2.5 and 2.6.

$$\sigma = \frac{1}{2}(\sigma_1 + \sigma_2) + \frac{1}{2}(\sigma_1 - \sigma_2)\cos(2\theta) \tag{2.5}$$

$$\tau = \frac{1}{2}(\sigma_1 - \sigma_2)\sin(2\theta) \tag{2.6}$$

We can obtain the Mohr's circle by plotting σ and τ in a diagram. The Mohr's circle has a radius of $(\sigma_1 - \sigma_2)/2$ and a center point of $(\sigma_1 + \sigma_2)/2$ on the σ-axis. The Mohr's circle is a very useful tool to analyze the rock failure behavior. Fig. 2.2 shows the Mohr's circle in two dimensions. The construction of Mohr's circle in three dimensions is more complicated than in two dimensions. More details can be found elsewhere (Fjar et al., 2008; Jaeger et al., 2009).

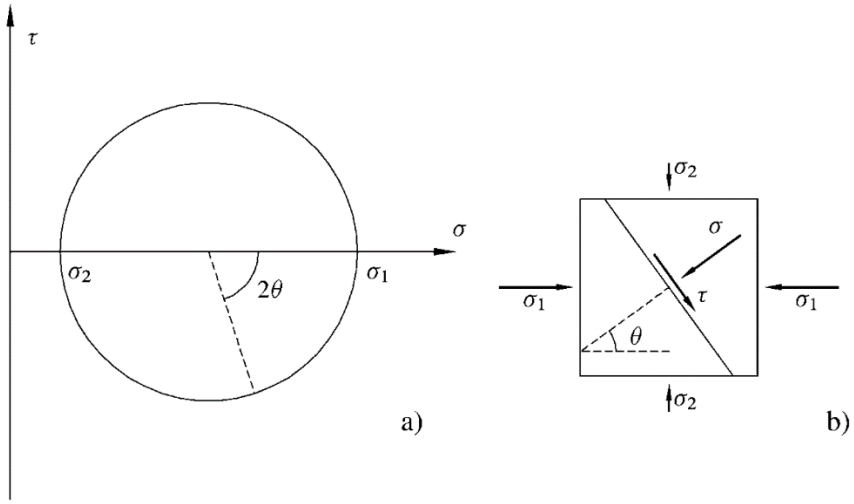

Figure 2.2: (a) Mohr's circle in two dimensions. (b) Stresses σ and τ in a direction θ relative to the σ-axis (Fjar et al., 2008).

The stress tensor changes as the orientation of coordinate system changes. However, some properties of the stress tensor remain invariant, which are known as stress invariants. For instance, the mean normal stress is a simple invariant of stress:

$$\sigma_m = \frac{\sigma_x + \sigma_y + \sigma_z}{3} \tag{2.7}$$

Other commonly used stress invariants are shown in Eq. 2.8 - 2.10. The combination of stress invariants will result in a stress invariant as well.

$$I_1 = \sigma_x + \sigma_y + \sigma_z \tag{2.8}$$

$$I_2 = -(\sigma_x\sigma_y + \sigma_y\sigma_z + \sigma_z\sigma_x) + \tau_{xy}^2 + \tau_{yz}^2 + \tau_{xz}^2 \tag{2.9}$$

$$I_3 = \sigma_x\sigma_y\sigma_z + 2\tau_{xy}\tau_{yz}\tau_{xz} - \sigma_x\tau_{yz}^2 - \sigma_y\tau_{xz}^2 - \sigma_z\tau_{xy}^2 \tag{2.10}$$

The mean normal stress σ_{m} results in uniform compression or extension. On the contrary, the distortion is a result of the deviatoric stress. The deviatoric stress is defined by subtracting the mean normal stress from the normal stress components as shown in Eq. 2.11. Eq. 2.12 - 2.14 show the invariants of stress deviation.

$$\begin{pmatrix} s_x & s_{xy} & s_{xz} \\ s_{yx} & s_y & s_{yz} \\ s_{zx} & s_{zy} & s_z \end{pmatrix} = \begin{pmatrix} \sigma_x - \sigma_m & \tau_{xy} & \tau_{xz} \\ \tau_{yx} & \sigma_y - \sigma_m & \tau_{yz} \\ \tau_{zx} & \tau_{zy} & \sigma_z - \sigma_m \end{pmatrix} \tag{2.11}$$

$$J_1 = s_x + s_y + s_z \tag{2.12}$$

$$J_2 = -(s_x s_y + s_y s_z + s_z s_x) + s_{xy}^2 + s_{yz}^2 + s_{xz}^2 \tag{2.13}$$

$$J_3 = s_x s_y s_z + 2s_{xy}s_{yz}s_{xz} - s_x s_{yz}^2 - s_y s_{xz}^2 - s_z s_{xy}^2 \tag{2.14}$$

These stress invariants are used in failure criteria in that they are independent of the choice of coordinate axes. For instance, Druker-Prager criterion uses I_1 and J_2 to define the stress space. Other stress invariants can be related to the basic invariants, for example parameters q and r:

$$q = \sqrt{3J_2} = \sqrt{\frac{3}{2}[(\sigma_1 - \sigma_m)^2 + (\sigma_2 - \sigma_m)^2 + (\sigma_3 - \sigma_m)^2]} \tag{2.15}$$

$$r = \sqrt[3]{\frac{27}{2} J_3} = \sqrt[3]{\frac{27}{2}(\sigma_1 - \sigma_m)(\sigma_2 - \sigma_m)(\sigma_3 - \sigma_m)} \tag{2.16}$$

2.1.1.2 Strain

Strain measures the relative displacement of nearby particles. We consider the strain in two dimensions as shown in Fig. 2.3. For the strains in the x-direction, the normal strain ε_x is defined as the fractional shortening of a line which is originally parallel to the x-direction; the shear strain ε_{xy} is defined as half of the increase in the angle (ψ) of two lines that are originally parallel to the x- and y-direction (Jaeger et al., 2009). Therefore, the normal strain in the x-direction is given as:

$$\begin{aligned} \varepsilon_x &= \frac{(x+\Delta x) - x - [(x+\Delta x - u(x+\Delta x)) - (x - u(x))]}{(x+\Delta x) - x} \\ &= \frac{u(x+\Delta x) - u(x)}{\Delta x} \end{aligned} \tag{2.17}$$

where u is the x-component of the displacement. For infinitesimal strains, $\Delta x \rightarrow 0$, we have:

$$\varepsilon_x = \frac{\partial u}{\partial x} \tag{2.18}$$

When the angle Ψ is very small, the shear strain in the x-direction is given as:

$$\begin{aligned} \varepsilon_{xy} &= \frac{1}{2}\tan\Psi \approx \frac{1}{2}\sin\Psi \\ &= -\frac{1}{2}\cos\left(\frac{\pi}{2} + \Psi\right) \\ &= -\frac{1}{2}\frac{\vec{P_1'} \cdot \vec{P_2'}}{|\vec{P_1'}| \cdot |\vec{P_2'}|} \end{aligned} \tag{2.19}$$

In the limit when $\Delta x \rightarrow 0$ and $\Delta y \rightarrow 0$, we neglect the high-order squares and products of the strains and find that:

$$\varepsilon_{xy} = \frac{1}{2}\left(\frac{\partial u}{\partial y} + \frac{\partial v}{\partial x}\right) \tag{2.20}$$

where *v* is the y-component of the displacement. The normal and shear strains in the y-direction are in a similar form.

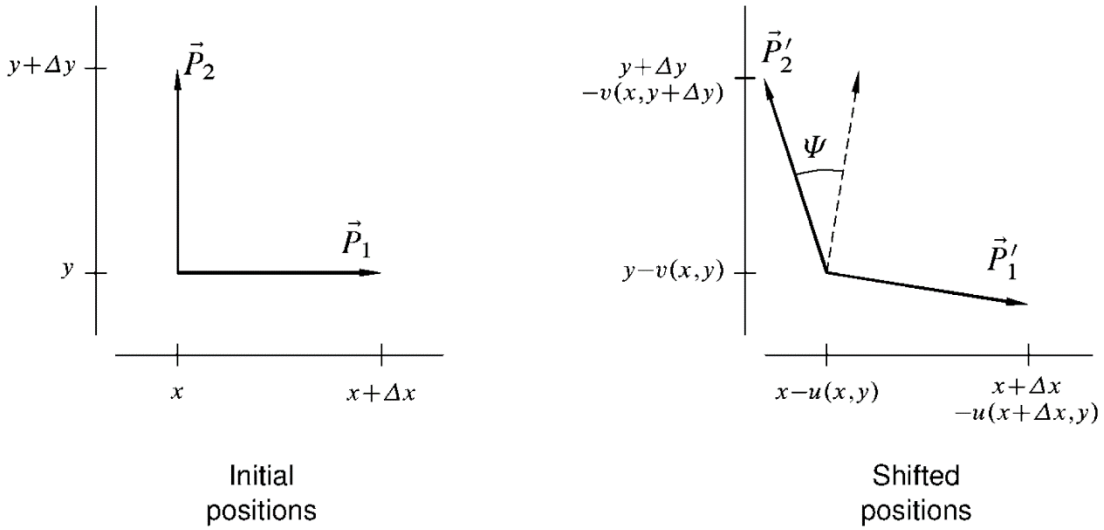

Figure 2.3: Illustration of normal and shear strain in two dimensions (Fjar et al., 2008).

In three dimensions, all strains can be defined in one mathematical notation as:

$$\varepsilon_{ij} = \frac{1}{2}\left(\frac{\partial u_i}{\partial x_j} + \frac{\partial u_j}{\partial x_i}\right) \tag{2.21}$$

where subscripts *i* and *j* denote any of the numbers 1, 2 and 3 that represent x-, y- and z-direction, respectively. For instance, $u_1 = u$ and $x_1 = x$. Eq. 2.22 shows the strain tensor. The volumetric strain ε_{vol} representing the change in volume divided by the initial volume is equal to the summation of normal strains (Eq. 2.23).

$$\begin{pmatrix} \varepsilon_{11} & \varepsilon_{12} & \varepsilon_{13} \\ \varepsilon_{21} & \varepsilon_{22} & \varepsilon_{23} \\ \varepsilon_{31} & \varepsilon_{32} & \varepsilon_{33} \end{pmatrix} \tag{2.22}$$

$$\varepsilon_{vol} = \varepsilon_{11} + \varepsilon_{22} + \varepsilon_{33} \tag{2.23}$$

2.1.1.3 Elastic moduli

The linear elasticity is a constitutive law describing the linear relationship between applied stresses and resulting strains. The material assumed linearly elastic has a reversible deformation. For a cylindrical sample, the applied axial stress is σ_1 and the resulting axial strain is ε_1. If the sample is linearly elastic, the stress-strain relationship can be described by Hooke's law:

$$\varepsilon_1 = \frac{1}{E}\sigma_1 \tag{2.24}$$

where the coefficient E is known as Young's modulus, which is one of the elastic moduli. Young's modulus describes the sample stiffness, i.e. the resistance against compression.

The applied stress also induces a radial strain ε_2. Usually, the axial strain ε_1 is positive and the radial strain ε_2 is negative. Another elastic parameter Poisson's ratio υ describes the lateral expansion relative to the longitudinal contraction:

$$\nu = -\frac{\varepsilon_2}{\varepsilon_1} \tag{2.25}$$

Eq. 2.24 and 2.25 assume only one component of stress (σ_1). In fact, every component of strain is a function of all components of stress. For isotropic materials that exhibit the same response regardless of the orientation of the applied stress, the stress-strain relationship is given by:

$$\begin{bmatrix} \sigma_x \\ \sigma_y \\ \sigma_z \\ \tau_{xy} \\ \tau_{yz} \\ \tau_{zx} \end{bmatrix} = \begin{bmatrix} \lambda+2G & \lambda & \lambda & 0 & 0 & 0 \\ \lambda & \lambda+2G & \lambda & 0 & 0 & 0 \\ \lambda & \lambda & \lambda+2G & 0 & 0 & 0 \\ 0 & 0 & 0 & 2G & 0 & 0 \\ 0 & 0 & 0 & 0 & 2G & 0 \\ 0 & 0 & 0 & 0 & 0 & 2G \end{bmatrix} \begin{bmatrix} \varepsilon_x \\ \varepsilon_y \\ \varepsilon_z \\ \varepsilon_{xy} \\ \varepsilon_{yz} \\ \varepsilon_{zx} \end{bmatrix} \tag{2.26}$$

where coefficient λ and G are elastic moduli, known as Lamé parameters. Parameter G is also called shear modulus, which represents the sample's resistance against shear deformation.

Another elastic modulus is the bulk modulus K, which is defined as the ratio of hydrostatic stress σ_p and the volumetric strain ε_{vol} (Eq. 2.27). For a hydrostatic stress state, $\sigma_p = \sigma_x = \sigma_y = \sigma_z$. The bulk modulus represents the sample's resistance against hydrostatic compression. The inverse of bulk modulus ($1/K$) is known as the compressibility.

$$K = \frac{\sigma_p}{\varepsilon_{vol}} = \lambda + \frac{2}{3}G \tag{2.27}$$

When any two of the elastic moduli, including E, υ, λ, G and K, are given, the remaining ones can be calculated, for instance, Eq. 2.27. Another commonly used elastic modulus is the plain strain modulus $E^{'}$. Considering a cylindrical sample, this is a condition of no strain in the radial direction ($\varepsilon_2 = 0$), i.e. a state of plane strain. The plain strain modulus $E^{'}$ is defined as:

$$E^{'} = \frac{\sigma_1}{\varepsilon_1} = \frac{E}{1-\upsilon^2} = \frac{2G}{1-\upsilon} \tag{2.28}$$

2.1.1.4 Effective stress

Rocks are porous media with the non-solid part also playing an important role in its mechanical behavior. Poroelasticity is a theory dealing with the interaction between solid deformation and fluid flow within a linear porous medium. Interested readers are referred to the Biot's poroelastic theory (Biot, 1941, 1962). In this section, we focus on reviewing an important concept of poroelasticity, the effective stress. The effective stress concept was firstly introduced in soil mechanics by Terzaghi in 1923 (von Terzaghi, 1923). Terzaghi stated that (1) increasing the hydrostatic stress or reducing the pore pressure results in the same amount of volume change of the material; (2) the material shear strength

is only dependent on the difference between the normal stress and the pore pressure. This indicates that the soil failure is determined by the effective stress rather than the total stress. The Terzaghi effective stress is shown as:

$$\sigma_p^{'} = \sigma_p - p_p \tag{2.29}$$

where $\sigma_p^{'}$ is the effective hydrostatic stress, σ_p is the total hydrostatic stress due to the external load, p_p is the pore pressure.

Terzaghi effective stress is a reasonable assumption for soils. However, it may underestimate the effective stress of rocks. Biot (1941) derived a more general form of effective stress based on the theory of poroelasticity:

$$\sigma_p^{'} = \sigma_p - \alpha p_p \tag{2.30}$$

where parameter α is known as the Biot coefficient. Eq. 2.30 indicates that the solid carries the $\sigma_p^{'}$ part of the total stress σ_p and the fluid carries the remaining part of αp_p. The other part of the pore pressure, $(1-\alpha)p_p$, is counteracted by the solid framework. The Biot coefficient is shown as a function of the bulk moduli of solid framework (K_{fr}) and solid grains (K_s).

$$\alpha = 1 - \frac{K_{fr}}{K_s} \tag{2.31}$$

The framework bulk modulus K_{fr} is always smaller than the solid grain bulk modulus K_s. The upper limit of K_{fr} is $(1 - \phi)\, K_s$, where ϕ is the sample porosity. Therefore, Biot coefficient α changes from ϕ to 1. For unconsolidated rocks, α is usually close to 1.

2.1.2 Failure mechanics

When the sample is subject to sufficiently large stresses, a failure will occur. Rock strength is the stress level at which a rock fails, which is dependent on the stress state. Rocks can fail in different failure modes including tensile failure, shear failure and

compaction failure. Usually before a failure, the sample goes beyond the yield point with a permanent change, which is known as the plastic behavior.

2.1.2.1 Strength

The strength of a sample is meaningful only when the stress condition is specified. In this section, we introduce the strength and other relevant concepts based on the most commonly used mechanical tests, uniaxial and triaxial tests. The uniaxial or triaxial test usually requires a cylindrical specimen with a length to diameter ratio of two. An axial stress is applied to two ends of the sample while a radial stress of different level to the circumference. The uniaxial and triaxial tests have a confining stress of zero and non-zero, respectively. Fig. 2.4 shows a schematic of the specimen and applied stress condition.

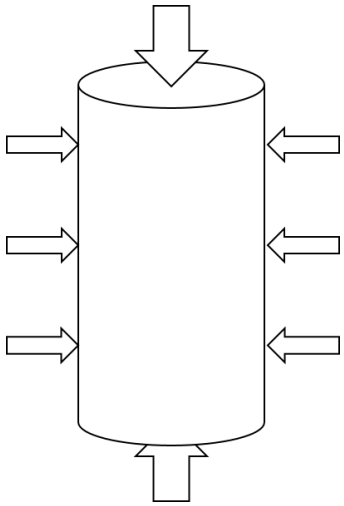

Figure 2.4: A cylindrical specimen used in the uniaxial or triaxial tests.

Fig. 2.5 shows a typical result of a uniaxial test. The axial stress (σ_z) is a function of the axial strain (ε_z) of the testing sample. As the axial strain increases, the axial stress firstly increases, then reaches the peak stress followed by a significant decrease.

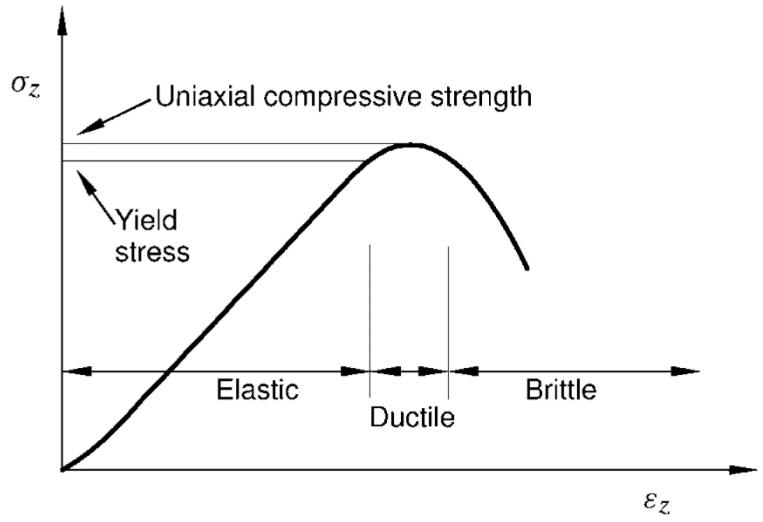

Figure 2.5: A typical stress-strain response in a uniaxial test. The ductile region could be very small (Fjar et al., 2008).

When the σ_z is relatively small, the sample shows an elastic and recoverable deformation. When the σ_z goes beyond the yield stress, a plastic deformation will occur and the stress-strain curve starts to deviate from the linear relationship. The uniaxial compressive strength is the peak stress. In the ductile region, the sample undergoes a plastic deformation but still has the capability to support an external load. On the contrary, in the brittle region, the sample rapidly loses the capability to withstand the applied stress.

For triaxial tests, we usually increase the axial stress and radial confining stress to a hydrostatic stress level. Then, the confining stress remains constant and the axial stress is increased until the sample fails. Therefore, it is customary to plot the deviatoric stress (difference between the axial stress and the confining stress) against the axial strain (Fig. 2.6).

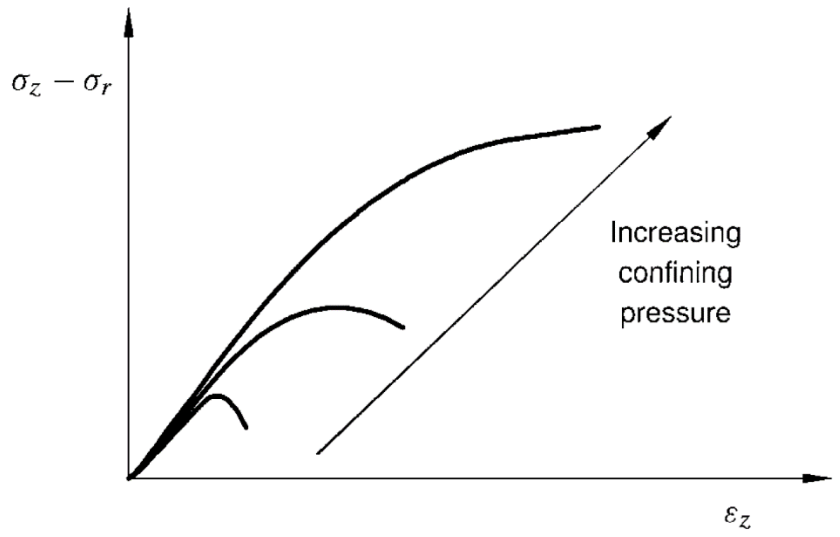

Figure 2.6: Influence of confining stress on the stress-strain response in a triaxial test (Fjar et al., 2008).

The confining stress level is shown to have a significant impact on the result of triaxial tests. The sample under a large confining stress tends to behave in the ductile region. An absence of strength is also possible for the sample under a very high level of confining stress. Samples in uniaxial and triaxial tests usually exhibit a shear failure due to the excessive shear stress. Other failure modes include tensile failure and compaction failure, which are induced by the excessive tensile and hydrostatic stresses. More details will be shown in the next section. Note that the effective stresses rather than the total stresses result in the failure behavior.

2.1.2.2 Failure modes

When the tensile stress in the sample exceeds the tensile strength T_0, tensile failure occurs. Most sedimentary rocks tend to have a very low tensile strength, usually a few MPa. For some materials, e.g. unconsolidated sands, the tensile strength can be as low as zero. The tensile failure is typically a highly localized and inhomogeneous process. The

failure planes usually initiate from pre-existing cracks and the largest crack rapidly splits the entire sample (Fig. 2.7a). The tensile failure criterion is given as:

$$\sigma' = -T_0 \tag{2.32}$$

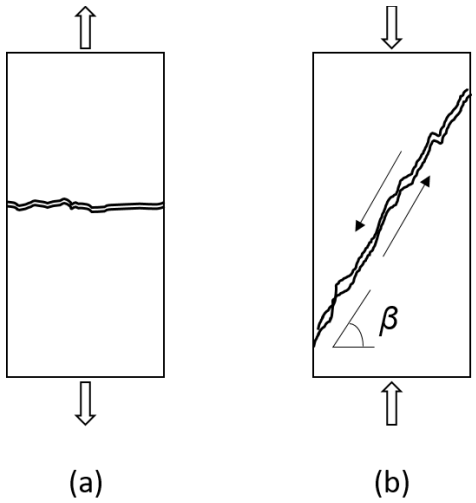

Figure 2.7: Schematic of (a) tensile failure and (b) shear failure.

When the shear stress along some planes exceeds the shear strength, shear failure occurs. The two sides of the shear failure plane move relative to each other with a friction force (Fig. 2.7b). It is known that the critical shear stress (τ_{max}) along the failure plane is a function of the stress (σ') acting normally to the plane:

$$|\tau_{max}| = f(\sigma') \tag{2.33}$$

Eq. 2.33 is known as Mohr's hypothesis which is a line separating an intact region from a failure region. This line is sometime referred to as the failure envelope. Various forms of $f(\sigma')$ correspond to various shear failure criteria. The simplest form is that $f(\sigma')$ is a constant, which is known as Tresca criterion:

$$\tau_{max} = \frac{1}{2}(\sigma_1' - \sigma_3') = S_0 \tag{2.34}$$

where S_0 is the inherent shear strength or cohesion of the material.

A more generally used shear failure criterion is the Mohr-Coulomb criterion, which assumes that:

$$\left|\tau_{\max}\right| = S_0 + \mu\sigma' = S_0 + (\tan\phi)\sigma' \tag{2.35}$$

where μ is the coefficient of internal friction and ϕ is the angle of internal friction. Therefore, the Tresca criterion is essentially a special condition of the Mohr-Coulomb criterion with $\phi = 0$. The orientation of the shear failure plane β can be related to the angle of internal friction ϕ:

$$\beta = \frac{\pi}{4} + \frac{\phi}{2} \tag{2.36}$$

The parameter ϕ in theory varies between 0° to 90°, therefore, the parameter β may change from 45° to 90°. Fig 2.8 shows the Mohr-Coulomb criterion in τ - σ' space. The Mohr's circle is in contact with the failure criterion indicating a critical stress state. The Mohr-Coulomb criterion can also be expressed in the principal σ_1 - σ_3 space as:

$$\sigma_1' = \frac{1+\sin\phi}{1-\sin\phi}\sigma_3' + 2S_0\sqrt{\frac{1+\sin\phi}{1-\sin\phi}} = q\sigma_3' + USC \tag{2.37}$$

where *USC* is the uniaxial compressive strength. Other failure criteria include the Drucker-Prager criterion (Drucker and Prager, 1952), the Griffith criterion (Griffith, 1921) etc.

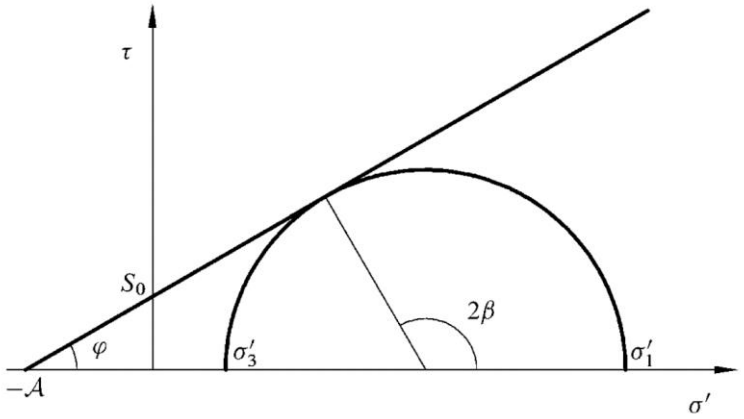

Figure 2.8: Mohr-Coulomb criterion in the space of τ and σ'. The Mohr's circle is in a critical stress state (Fjar et al., 2008).

Another failure mode is the compaction failure. A hydrostatic stress state may induce the compaction failure caused by pore collapse and grain crushing. A non-hydrostatic stress state, for instance, triaxial test with a high confining stress, may also induce the compaction failure, which is known as shear-enhanced compaction. The compaction failure is represented by an end cap in principal stress space (Fig. 2.9).

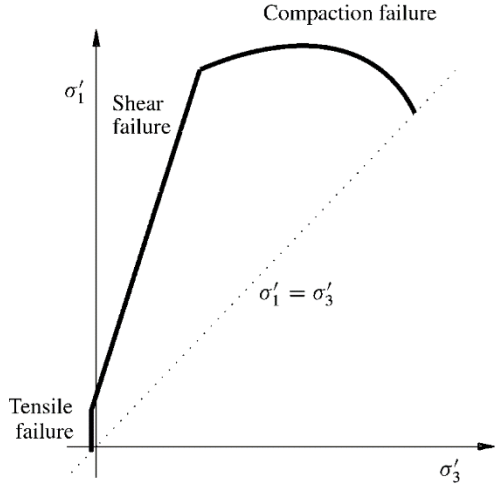

Figure 2.9: Various failure modes in principal stress space. The dashed line represents a hydrostatic stress state (Fjar et al., 2008).

The end cap is often assumed in an elliptical form (DiMaggio and Sandler, 1971; Wong et al., 1997):

$$\frac{1}{(1-\gamma)^2}\left(\frac{\sigma_m^{'}}{P^*}-\gamma\right)^2+\frac{1}{\delta^2}\left(\frac{q}{P^*}\right)^2=1 \tag{2.38}$$

where $\sigma_m^{'}$ is the mean effective stress, q is a deviatoric stress invariant, P^* is the critical effective pressure, γ (≈ 0.5) and δ (≈ 0.5-0.7) are constants. For the hydrostatic stress state, the sample shows a compaction failure when $\sigma_m^{'} = P^*$. Note that it is not trivial to plot the end cap in τ - $\sigma^{'}$ space. Therefore, the compaction failure cannot be presented the same way as the shear failure for Mohr's circle.

2.1.2.3 Plasticity

The concept of plasticity describes plastic and permanent deformation of materials. The plasticity is used to model the ductile behavior rather than the brittle behavior. The onset of plastic deformation is represented by the yield criterion. Similar to the failure criterion, a yield criterion defines the surface where plasticity is initiated. For rather ductile samples, the yield criterion is more precisely defined than the failure criterion. The total strain increment ($d\varepsilon_{ij}$) is assumed as the summation of an elastic part ($d\varepsilon_{ij}^{e}$) and a plastic part ($d\varepsilon_{ij}^{p}$):

$$d\varepsilon_{ij} = d\varepsilon_{ij}^{e} + d\varepsilon_{ij}^{p} \tag{2.39}$$

The plastic strain is permanent and will remain even with the stress relieved.

The flow rule relates the plastic strain increment ($d\varepsilon_{ij}^{p}$) to the stress increment ($d\sigma_{ij}^{'}$) shown as:

$$d\varepsilon_{ij}^{p} = d\lambda \frac{\partial g}{\partial \sigma_{ij}^{'}} \tag{2.40}$$

where g is plastic potential and λ is a scalar not specified by the flow rule. Druker found that the plastic potential g is the same as the yield surface function f for stable and strain hardening materials (Drucker and Prager, 1952). In other words, the plastic flow is known once the yield surface is specified. In this condition, the flow rule is called associated:

$$\sum_{ij} \sigma_{ij}^{'} d\varepsilon_{ij}^{p} \geq 0 \tag{2.41}$$

$$d\varepsilon_{ij}^{p} = d\lambda \frac{\partial f}{\partial \sigma_{ij}^{'}} \tag{2.42}$$

However, not all the rock materials fulfill the associated flow rule. In this condition, plastic potential and yield surface function are not identical, known as non-associated flow rule. The Mohr-Coulomb criterion is used to describe this concept. By rearranging Eq. 2.37, the yield surface function f is shown as:

$$f = \sigma_1^{'} - \frac{1-\sin\phi}{1+\sin\phi}\sigma_3^{'} - 2S_0\sqrt{\frac{1-\sin\phi}{1+\sin\phi}} \tag{2.43}$$

$$g = \sigma_1^{'} - \frac{1-\sin\psi}{1+\sin\psi}\sigma_3^{'} - 2S_0\sqrt{\frac{1-\sin\psi}{1+\sin\psi}} \tag{2.44}$$

The plastic potential g replaces the internal friction angle ϕ with the dilatancy angle ψ. It is convenient to control the dilatancy rather than change the yield criterion. The condition of $\psi > 0$, $\psi = 0$ and $\psi < 0$ correspond to dilatancy, isochoric deformation and contraction of materials.

The plastic strain can change the yield surface in the principal stress space which is known as hardening or softening. Hardening or softening describes a material that is stronger or softer, respectively, after yield. Note that ideally plastic material has a yield surface coinciding with the failure surface therefore maintains at a constant stress while deformed. The yield surface with hardening and softening is a function of not only principal stresses $\sigma_1^{'}$, $\sigma_2^{'}$ and $\sigma_3^{'}$ but a parameter κ describing the hardening effects:

$$f(\sigma_1^{'}, \sigma_2^{'}, \sigma_3^{1}, \kappa) = 0 \tag{2.45}$$

$$\kappa = \kappa\left(\int_S d\varepsilon_{ij}^{p}\right) \tag{2.46}$$

The parameter κ is a function of the plastic strain integrated over the stress path (Eq. 2.46). Fig. 2.10 shows a sketch of the hardening, i.e. the change in yield surface, in the principal stress space of $\sigma_1^{'}$ - $\sigma_3^{'}$.

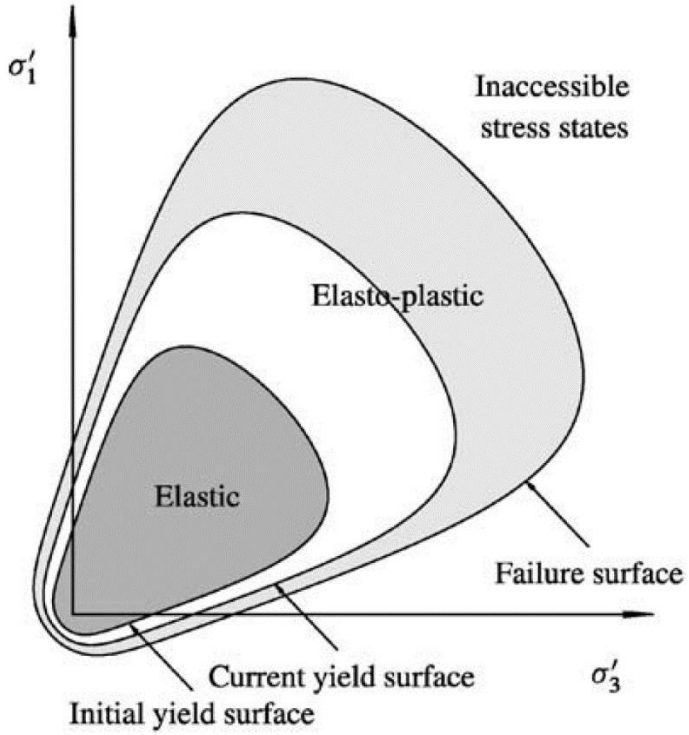

Figure 2.10: Hardening changes the yield surface in the principal stress space (Fjar et al., 2008).

2.2 PORE-SCALE MODELING

In principle, the combination of Newton's equation for particulate motion and Navier-Stokes equations for fluid flow fully describes the particle-fluid flow system. However, due to computational capability limited by the number of particles and grids, simplifications must be made (Zhu et al., 2007). The particulate phase can be modeled by either a macroscopic continuum approach or a microscopic discrete approach. For the continuum approach, balance equations together with initial and boundary conditions are necessary to describe the macroscopic behavior. This approach is efficient in computation. However, the efficiency is based on constitutive relations which have limited application. One example of a continuum approach is the two fluid model (TFM), which treats both the

fluid and solid phases as continuum media. On the other hand, discrete approaches, for instance, the discrete element method, can describe the motions of individual particles without the need for global assumptions. This section presents (1) the pore-scale geomechanical model for the solid granular medium and (2) the coupled particle-fluid flow model.

2.2.1 Pore-scale geomechanical model

The model presented here approximates the grains of rock by rigid spherical particles and represents the cements by bonds connecting grains. Discrete element code LIGGGHTS is adopted to calculate the interactions among particles (Kloss et al., 2012). The Bonded-Particle Model (BPM), which idealizes the cementation as bonds with limited strength constraining the translation and rotation of particles, is coupled with LIGGGHTS.

2.2.1.1 Discrete Element Method (DEM)

The DEM provides a tool to investigate the mechanical response of granular media. An individual grain is approximated by an idealized shape, e.g. sphere in 3D and disk in 2D. The macroscale mechanical behavior emerges from the interplay of mostly rigid particles through their contacts at the microscale (Cundall and Strack, 1979). Newton and Euler equations can describe the dynamics of the particles:

$$\begin{aligned} m_i \ddot{x}_{n,i} &= F_{n,i} \\ I_i \cdot \dot{\omega}_{n,i} + \omega_{n,i} \times I_i \cdot \omega_{n,i} &= T_{n,i} \end{aligned} \tag{2.47}$$

where m_i, $\ddot{x}_{n,i}$, I_i, $\omega_{n,i}$, $\acute{\omega}_{n,i}$ are respectively the mass, acceleration, inertia tensor, angular velocity and acceleration of the i-th body at the timestep n. $F_{n,i}$ and $T_{n,i}$ are the corresponding net force and torque acting on the body. The DEM is an explicit numerical method alternatively calculating the motion of particles and its causes, namely forces and torques. In addition to Eq. (2.47), a contact law is needed to update the dynamics.

The contact law acts as a spring-damper system where forces are decomposed into both normal and shear directions. When particles *i* and *j* contact each other, a repulsive normal force $F_{\mathrm{N,ij}}$ and a frictional tangential force $F_{\mathrm{T,ij}}$ are calculated. For spherical particles, the overlap between particles *i* and *j* is denoted as δ_{ij}:

$$\delta_{ij} = R_i + R_j - \left\| \boldsymbol{x}_i - \boldsymbol{x}_j \right\| \tag{2.48}$$

with particles *i* and *j* having radii R_{i} and R_{j} and positions $\boldsymbol{x}_{\mathrm{i}}$ and $\boldsymbol{x}_{\mathrm{j}}$. The contact force is calculated if $\delta_{\mathrm{ij}} > 0$. $F_{\mathrm{N,ij}}$ with an angle normal to the contact surface is calculated by the spring-damper model:

$$F_{N,ij} = k_N \delta_{ij} + d_N \dot{\delta}_{ij} \tag{2.49}$$

where k_{N} is the normal stiffness and d_{N} is the normal damping. k_{N} for the point contact between particles is determined from

$$k_N = 2E_c(R_1 + R_2) \tag{2.50}$$

where R_1 and R_2 are radii of two contact particles and E_{c} is the elastic modulus for the particle-particle contact. Similarly, the tangential force is computed from

$$\boldsymbol{F}_{T,ij} = -k_T \boldsymbol{\xi}_{T,ij} - d_T \boldsymbol{v}_{T,ij} \tag{2.51}$$

with the tangential stiffness k_{T}, the tangential deformation vector $\boldsymbol{\xi}_{\mathrm{T,ij}}$ in the tangential plane, the tangential damping d_{T} and the relative tangential velocity of the particles $\boldsymbol{v}_{\mathrm{T,ij}}$. $\boldsymbol{\xi}_{\mathrm{T,ij}}$ is equal to $\boldsymbol{v}_{\mathrm{T,ij}}$ multiplied by the timestep. In case of the tangential force exceeding the limit of $F_{\mathrm{T,ij}} = \mu F_{\mathrm{N,ij}}$, where μ is the friction coefficient, the tangential force is described by slipping friction

$$\boldsymbol{F}_{T,ij} = -\mu F_{N,ij} \frac{\boldsymbol{v}_{T,ij}}{\left\| \boldsymbol{v}_{T,ij} \right\|} \tag{2.52}$$

Thus, parameters of the DEM include elastic modulus E_{c}, stiffness ratio $k_{\mathrm{N}}/k_{\mathrm{T}}$, friction coefficient μ, grain mass density ρ, and grain radius R.

2.2.1.2 Bonded-Particle Model (BPM)

In the DEM the cemented material is usually represented by breakable bonds connecting particles. Some bond models are based on the transfer of normal and tangential forces until the bond breakage (Jiang et al., 2007; Utili and Nova, 2008; Wang and Leung, 2008; Ergenzinger et al., 2011; Rojek et al., 2011; Sun et al., 2016b, 2016c) whereas other models additionally incorporate the transfer of torque (Potyondy and Cundall, 2004; Wang and Alonso-Marroquin, 2009). The latter is more applicable to rock mechanics and is adopted here. The Bonded-Particle Model (BPM) in this study represents the cementation by bonds connecting the centers of bonded particles, the relative displacements and rotations of which can be decomposed into normal, tangential, bending and twisting components. Quaternion algebra, a number system describing three-dimensional rotations, is used here to calculate the deformation of bonds, which has been proven with more numerical stability and accuracy than the incremental approach (Wang and Alonso-Marroquin, 2009). An overview of the BPM is presented here for completeness; more details, including the implementation of quaternion algebra, can be found in the literatures (Potyondy and Cundall, 2004; Obermayr et al., 2013).

In a local coordinate system, the deformation of two bonded particles is denoted as $\boldsymbol{u}$, which has three components with one aligning and the other two orthogonal to the bond direction. The bond strain $\mathbf{E}$ then follows from

$$\mathbf{E} = \frac{1}{L}\boldsymbol{u} \tag{2.53}$$

where L is the length of the bond. Note that $\mathbf{E}$ has included both the compressive and tensile deformations from the relative translation. The forces between adjacent particles are calculated from the elastic modulus E_b, the shear modulus G_b and the cross-section area A_b:

$$\boldsymbol{F} = \begin{pmatrix} E_b A_b & 0 & 0 \\ 0 & G_b A_b & 0 \\ 0 & 0 & G_b A_b \end{pmatrix} \mathrm{E} \tag{2.54}$$

Additionally, local damping has also been included (without affecting the numerical solution) to guarantee the stability of simulation. With the reduced mass:

$$m_r = \frac{m_1 m_2}{m_1 + m_2} \tag{2.55}$$

the damping force is calculated as:

$$\boldsymbol{F}_d = 2D \begin{pmatrix} \sqrt{\frac{E_b A_b}{L_o} m_r} & 0 & 0 \\ 0 & \sqrt{\frac{G_b A_b}{L_o} m_r} & 0 \\ 0 & 0 & \sqrt{\frac{G_b A_b}{L_o} m_r} \end{pmatrix} \boldsymbol{V}_{12} \tag{2.56}$$

with the damping ratio D, the initial bond length L_0 and the relative velocity vector $\boldsymbol{V}_{12}$.

Similarly, the relative rotation is denoted as $\boldsymbol{\varepsilon}$, from which the curvature of the bond element is:

$$\boldsymbol{\kappa} = \frac{1}{L} \boldsymbol{\varepsilon} \tag{2.57}$$

The torque between the bonded particles is then:

$$\boldsymbol{T} = \begin{pmatrix} 2G_b J_b & 0 & 0 \\ 0 & E_b J_b & 0 \\ 0 & 0 & E_b J_b \end{pmatrix} \boldsymbol{\kappa} \tag{2.58}$$

where J_b is the second moment of the cross-section area of the bond. With the reduced moment of inertia:

$$I_r = \frac{I_1 I_2}{I_1 + I_2} \tag{2.59}$$

the damping torque $\boldsymbol{T}_d$ is calculated as

$$\boldsymbol{T}_d = \begin{pmatrix} \sqrt{\frac{2G_b J_b}{L_0} I_r} & 0 & 0 \\ 0 & \sqrt{\frac{E_b J_b}{L_0} I_r} & 0 \\ 0 & 0 & \sqrt{\frac{E_b J_b}{L_0} I_r} \end{pmatrix} \boldsymbol{\Omega}_{rel} \tag{2.60}$$

where the $\boldsymbol{\Omega}_{\text{rel}}$ is the relative angular velocity. The local forces and torques are converted into the global coordinate system and then applied on bonded particles.

Bonds break when the stresses exceed the limit resulting in irreversible damage. The axial and shear stresses of the bonds are calculated as

$$\sigma_{axial} = E_b \Gamma_x + \sqrt{(E_b \kappa_y R_b)^2 + (E_b \kappa_z R_b)^2} \tag{2.61}$$

$$\tau_{shear} = G_b \kappa_x R_b + \sqrt{(G_b \Gamma_y)^2 + (G_b \Gamma_z)^2} \tag{2.62}$$

With the axial strength σ_{c} and the shear strength τ_{c}, the bond will break when either $\sigma_{\text{axial}} > \sigma_{\text{c}}$ or $\tau_{\text{shear}} > \tau_{\text{c}}$. Note that the bonds have circular cross-sections with radius R_{b}. Apparent normal and shear stiffness $\bar{k}_{\text{N}}$ and $\bar{k}_{\text{T}}$ are determined from:

$$\bar{k}_N = \frac{E_b}{R_1 + R_2} \tag{2.63}$$

$$\bar{k}_T = \frac{G_b}{R_1 + R_2} \tag{2.64}$$

A coefficient λ is defined to transfer the bond radii R_{b} from local parameters to a global parameter (Obermayr et al., 2013). With two arbitrarily connected particles *i* and *j*, the radius of the bond $R_{\text{b,ij}}$ is:

$$R_{b,ij} = \lambda \frac{R_i + R_j}{2} \tag{2.65}$$

Thus, λ is a dimensionless parameter representing the radii of bonds. Numerically, λ ranges from 0 to 1. To summarize, parameters for the BPM include bond elastic modulus E_{b}, bond stiffness ratio $\bar{k}_{\text{N}}/\bar{k}_{\text{T}}$, bond size parameter λ, bond normal strength σ_{c} and shear strength τ_{c}.

Fig. 2.11 shows a schematic diagram of the model coupling the DEM and the BPM. The forces between bonded particles *i* and *j* shown are idealized as the spring-damper system, where the stiffness, damping and friction coefficient are the parameters of the spring, dashpot, and slip, respectively. The net force is the summation of particle force and cement force, both of which can be decomposed into normal and tangential directions (for 3D case, two tangential directions).

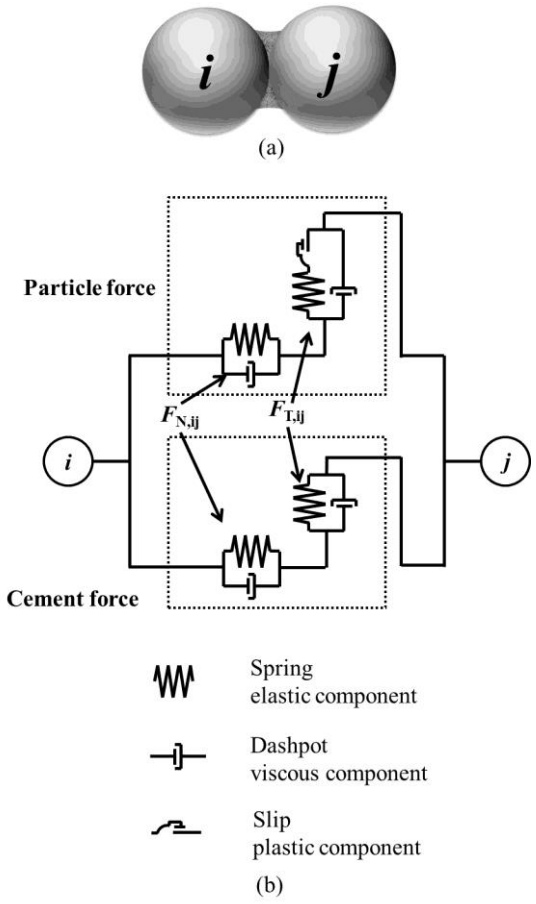

Figure 2.11: Schematic of the model coupling the DEM and the BPM.

2.2.2 Coupled particle-fluid flow model

The solid granular medium is modeled with the Discrete Element Method (DEM) and the fluid flow is solved using Computational Fluid Dynamics (CFD). This coupled method is implemented within the CFDEMcoupling, which is an interface between the discrete element code LIGGGHTS and the CFD toolbox OpenFOAM (Kloss et al., 2012).

2.2.2.1 Computational Fluid Dynamics (CFD)

Computational Fluid Dynamics (CFD) is a direct numerical simulation of the fluid flow. The techniques of CFD consist of simulations based on the Navier-Stokes (N-S) equations and Lattice Boltzmann Method (LBM). The N-S equations are derived based on Newton's second law describing the motion of a viscous fluid:

$$\rho \frac{Du}{Dt} = -\nabla p + \mu \nabla^2 u + \frac{1}{3}\mu \nabla\left(\nabla \cdot u\right) + \rho g \tag{2.66}$$

where ρ is fluid mass density, $\boldsymbol{u}$ is velocity, p is pressure, μ is fluid viscosity, t is time and g is gravity acceleration. In the traditional CFD, the N-S equations are discretized and solved in space and time using different numerical methods, i.e. finite element method, finite volume method and finite difference method.

On the other hand, the LBM solves the Boltzmann equation to simulate the fluid flow with collision models (Bhatnagar et al., 1954). The LBM simulates the streaming and collision processes of a large number of particles and the viscous fluid flow is a collective behavior of particle interactions, which is represented by probability distribution function (PDF), $f(X,V,\mathrm{t})$. The Boltzmann equation describes the evolution for the PDF:

$$\frac{\partial f(X,V,t)}{\partial t} + V \cdot \nabla f(X,V,t) = \Omega(f(X,V,t)) \tag{2.67}$$

where X is spatial position, V is velocity, t is time, and Ω is collision operator. The LBM can deal with complex boundaries therefore is very popular for simulating fluid flow through porous media (Aharonov and Rothman, 1993). However, the LBM is also rather

computationally expensive. Other CFD techniques include the volume of fluid (Raeini et al., 2012), level set method (Prodanović and Bryant, 2006), etc. Interested readers of this topic are referred to several good reviews (Keehm, 2003; Meakin and Tartakovsky, 2009).

2.2.2.2 Resolved CFD-DEM model

Numerous researchers have investigated the coupled CFD-DEM model that combines Eulerian and Lagrangian methods (Zhu et al., 2007; Prodanović et al., 2012; Han and Cundall, 2013; Mondal et al., 2016a). In this dissertation, we use the resolved CFD-DEM model which has advantages including that (1) fluid flow is fully resolved without any reduced order models (in contrast to the unresolved approach that assumes a drag law of fluid flow); (2) the model has structural rectilinear CFD meshes independent of the particle location therefore avoids grid regeneration and unstructured meshes that could be computationally expensive; (3) the model has a good scalability which enables parallel implementation. This resolved approach is applicable for large particles covering fine computational mesh cells that simulate the accurate fluid flow and fluid-solid coupling.

The resolved CFD-DEM approach models the solid phase with fictitious domain method, which is suitable for a complex geometry (particulate phase in this study) embedded in a simple domain (Shirgaonkar et al., 2009). Fig. 2.12 shows a particle within the computational domain that has uniform meshing, where Ω and Ω_s are the rectangular domain and the particle domain, Γ and Γ_s are the domain boundary and the solid particle surface. A brief introduction to the model formulation and algorithm follows. More details can be found elsewhere (Shirgaonkar et al., 2009; Hager et al., 2014).

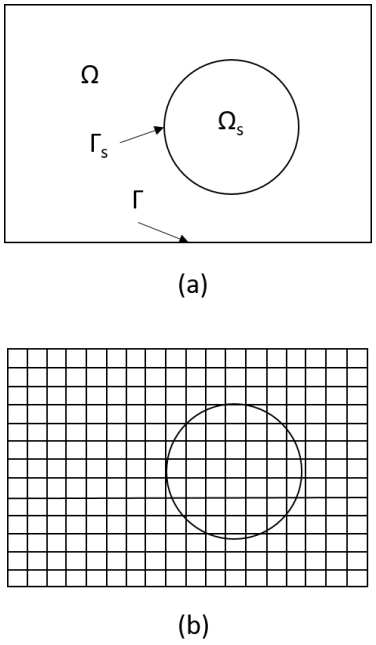

Figure 2.12: (a) A particle inside the computational domain. (b) The same domain is uniformly meshed for the resolved CFD-DEM model.

The problem is governed by a number of equations and conditions, including the momentum equation in Ω:

$$\rho_f \frac{\partial \mathbf{u}_f}{\partial t} + \rho_f (\mathbf{u}_f \cdot \nabla)\mathbf{u}_f = -\nabla p + \mu_f \nabla^2 \mathbf{u}_f \tag{2.68}$$

the continuity equation in Ω,

$$\nabla \cdot \mathbf{u}_f = 0 \tag{2.69}$$

the boundary condition on the rectangular domain boundary Γ,

$$\mathbf{u}_f = \mathbf{u}_\Gamma \tag{2.70}$$

the boundary condition on the interface Γ_s,

$$\mathbf{u}_f = \mathbf{u}_p \tag{2.71}$$

$$\sigma \cdot \hat{\mathbf{n}} = \mathbf{t}_{\Gamma_s} \tag{2.72}$$

the initial condition,

$$\mathbf{u}_f (t = 0) = \mathbf{u}_o \tag{2.73}$$

where ρ_f and μ_f are fluid mass density and viscosity, $\mathbf{u}_f$ and p are fluid velocity and pressure. $\sigma = -p\mathrm{I} + \tau$ represents the stress tensor of the fluid, which is used to calculate the traction force $\mathbf{t}_{\Gamma_s}$ acting on the particle. $\mathbf{u}_p$ is the particle velocity from the DEM model.

The algorithm of the fictitious domain method has three steps. First, we neglect the existence of particles and solve for the intermediate velocity field $\hat{\mathbf{u}}_f$ based on the Navier-Stokes equation using a finite volume CFD solver:

$$\rho_f \frac{\hat{\mathbf{u}}_f - \mathbf{u}_f^{n-1}}{\Delta t} + \rho_f (\mathbf{u}_f^{n-1} \cdot \nabla)\mathbf{u}_f^{n-1} = -\nabla \tilde{p} + \mu_f \nabla^2 \mathbf{u}_f^{n-1} \tag{2.74}$$

where superscript n-1 denotes the solution from the end of the previous time step, $\tilde{p}$ is the intermediate pressure field. When Re << 1, we can effectively solve Stokes flow neglecting the inertia term. The continuity equation results in the Poisson equation for pressure:

$$\nabla^2 \tilde{p} = -\nabla \cdot [\rho_f (\mathbf{u}^{n-1} \cdot \nabla)\mathbf{u}^{n-1}] \tag{2.75}$$

Second, we enforce the velocity of the particles on the cells representing the solid phase, which is equivalent to adding a force $\boldsymbol{f}$ to the semidiscrete Navier-Stokes equation:

$$\boldsymbol{f} = \rho_f \frac{\tilde{\mathbf{u}}_f - \hat{\mathbf{u}}_f}{\Delta t} \tag{2.76}$$

where $\tilde{\mathbf{u}}_f$ is the corrected velocity field.

The above two steps result in a discontinuity of velocity at the interface therefore violating the divergence-free condition. The third step is to remove this non-zero divergence by means of:

$$\mathbf{u}_f^n = \tilde{\mathbf{u}}_f - \nabla \phi \tag{2.77}$$

where $\mathbf{u}_f^n$ is the final velocity solution, ϕ is a scalar field calculated by:

$$\nabla^2 \phi = \nabla \cdot \tilde{\mathbf{u}}_f \tag{2.78}$$

To summarize, the algorithm consists of three steps: (1) solve the Navier-Stokes equation over the entire domain ignoring the solid phase; (2) impose motion of particles; (3) relax particle motion to project the flow field onto a divergence-free space.

The force on the particles is then calculated as:

$$\int_{\Omega_s} \eta(x,y,z,t)dV = \int_{\Omega} \eta(x,y,z,t)\xi(x,y,z,t)dV \tag{2.79}$$

where

$$\xi = \begin{cases} 1 \;\; if\,(x,y,z) \in \Omega_s \\ 0 \;\; else \end{cases} \tag{2.80}$$

$$\eta = \rho \nu_f \nabla^2 \mathbf{u}_f^{n-1} - \nabla p^{n-1} \tag{2.81}$$

which indicates that the force acting on particles consists of a viscous and a pressure component. Forces calculated from the CFD side are transferred to the DEM side to update the particle dynamics. One advantage of this approach is that two phases are represented by one flow field on the CFD side. CFD and DEM can run with different time steps to achieve an optimal behavior.

2.3 CO_2-Related Rock Chemo-Mechanical Alteration

Several challenges must be addressed before full-scale implementation of CO_2 sequestration, among them understanding underlying mechanisms of CO_2-related rock chemical alteration at storage sites. Experiments in both field and the laboratory have shown that injected CO_2 is able to alter the pH of the formation water and change the species composition through mineral dissolution and precipitation (Hovorka et al., 2006, 2013; Carroll et al., 2011; Lu et al., 2012). Fig. 2.13 shows the schematic of CO_2 sequestration and associated complexity due to the interaction between injected CO_2 and the host formation. Reaction rates of CO_2-related alteration depend on the rock mineralogy. Carbonates are more susceptible to mineral dissolution than siliceous minerals (Gunter et al., 2000; Pokrovsky et al., 2005; Le Guen et al., 2007; Assayag et al., 2009). The occurrence of geomechanical reactions initiated by CO_2 dissolution in water can have either a positive or negative impact (Kaszuba et al., 2005). On the one hand, the trapping

of CO_2 could benefit from reactions transforming the dissolved CO_2 into new carbonate minerals (Bachu et al., 2007). On the other hand, chemical reactions may jeopardize the structural integrity of reservoir and caprock formations by altering the petrophysical and geomechanical properties (Rutqvist and Tsang, 2002; Renard et al., 2008; Espinoza et al., 2011; Rinehart et al., 2016). Positive feedback mechanisms leading to rock degradation at CO_2 storage sites may facilitate leakage of CO_2 from host formations (Pruess, 2008).

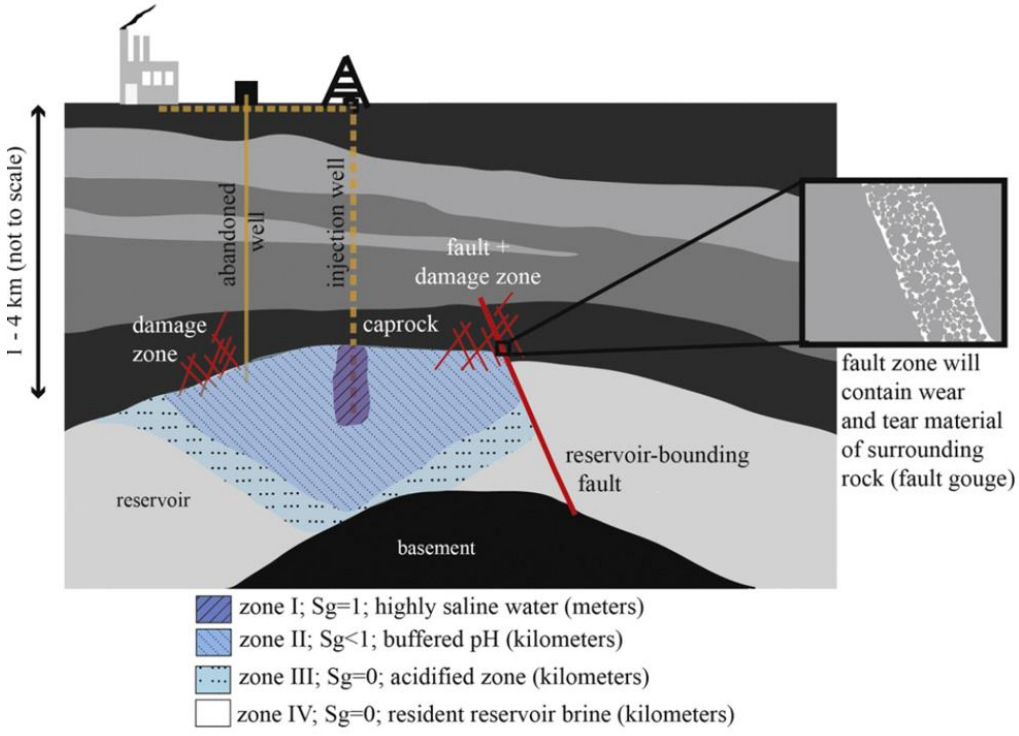

Figure 2.13: Schematic of CO_2 sequestration and associated complexity. Zones are divided based on CO_2 saturation (S_g). Various zones have different chemo-mechanical behaviors (Rohmer et al., 2016).

Experimental evidence shows that dissolution of minerals induced by exposure to CO_2-brine mixtures leads to changes in porosity and permeability (Canal et al., 2012; Carroll et al., 2013), increase of rock compaction (Le Guen et al., 2007; Liteanu et al., 2012), reduction of fracture toughness (Major et al., 2014; Sun et al., 2017; Zheng et al.,

2019), modification of yield stress locus (Rinehart et al., 2016; Bemer et al., 2016), and negligible changes in the sliding friction coefficient (Hangx et al., 2015; Bakker et al., 2016).

Fault activation and induced seismicity resulting from CO_2 storage are issues related to fluid waste disposal in the subsurface (Rutqvist, 2012; Zoback and Gorelick, 2012; Vilarrasa and Carrera, 2015; Rutqvist et al., 2016; Wang et al., 2017). Unexpectedly high magnitude microseismic events up to M = 1.2 have been observed in the Decatur project (Bauer et al., 2016). Mineral dissolution during CO_2 sequestration can induce reservoir compaction and stress relaxation; in extreme scenarios mineral dissolution may cause a compaction-driven shear failure of the reservoir (Renard et al., 2008; Shin et al., 2008; Espinoza et al., 2011; Kim and Santamarina, 2014; Stefanou and Sulem, 2014). Hence, coupled chemo-mechanical processes can contribute to further stress changes in subsurface storage formations, which would result in additional fracture reactivation and potential induced seismicity.

Core-flooding experiments are useful to document the CO_2-related rock alteration but are limited by their complexity and extended durations (Kutchko et al., 2008; Bachu and Bennion, 2009; Carroll et al., 2011, 2013; Mason et al., 2013; Liang et al., 2018). Autoclave experiments provide an alternative; however, the reaction front often penetrates just a few millimeters into the rock. Shallow alterations do not significantly affect the bulk strength of the entire core (Rimmelé et al., 2010). Micromechanical tests can measure the mechanical alteration of the reacted skin and offer an efficient tool for quantifying chemical susceptibility of rocks reacted in autoclave experiments (Sun et al., 2016a; Aman et al., 2017b).

Macroscopic rock mechanical behavior emerges from the aggregate effect of microscopic processes. Besides petrographic thin-section analyses, few studies have

attempted to explore mechanically how CO_2-related alteration develops at the grain and pore scale. The dissolution of small amounts of minerals can have a large impact on mechanical properties in some instances (Sun et al., 2018b). Laboratory tests have shown that CO_2-induced degradation of hematite-coated sandstones is likely due to the dissolution of interparticle cement (Wigley et al., 2012; Major et al., 2014). Fernandez and Santamarina (2001) showed that the effect of cementation on small-strain mechanical parameters prevails at low stress. Based on the hypothesis that CO_2 alteration tends to manifest more readily through cement alteration rather than full grain dissolution in siliceous sandstones with alterable cements, we attempt to explain the degradation of cementation due to contact with CO_2 and how it leads to changes in rock mechanical properties.

2.4 Reservoir Compaction and Grain Crushing

Reservoir compaction induces changes in porosity and permeability and could be a significant concern for the reservoir productivity. Other negative potential impacts include ground subsidence, casing buckling and shearing, sand production, and earthquakes (Sulak and Danielsen, 1988; Segall, 1989; da Silva et al., 1990; Teufel et al., 1991; Rhett and Teufel, 1992; Ostermeier, 1995; Fredrich et al., 2000; Hettema et al., 2000).

Compaction is dependent on the initial stress state and the depletion stress path. The stress path is determined by pore pressure changes, rock constitutive behavior and deformation of adjacent formations (Settari, 2002). Compaction models often assume a "one-dimensional (1-D) strain" stress path because (1) the reservoir compacts uniaxially in the vertical direction and the vertical total stress stays constant and (2) each vertical block deforms independently in reservoirs with a large areal extent with respect to the thickness (Geertsma, 1966; Teeuw, 1971; Finol and Ali, 1975; Rattia and Ali, 1981; Chase Jr. and

Dietrich, 1989; Settari and Walters, 2001; Chan, 2004). Therefore, uniaxial strain tests that mimic the reservoir compaction provide information to investigate the compaction effects on porosity and permeability.

The change in permeability induced by reservoir compaction is shown to vary widely even within a single formation (Fatt and Davis, 1952; McLatchie et al., 1958; Dobrynin, 1962). Stress-related changes in physical properties manifest through various grain-scale processes. Grain slippage and rotation commonly occur at low stress levels. Ductile/soft grains may experience changes in grain shape and brittle grains can fracture at high stress levels (Taylor, 1950; Gallagher et al., 1974; Zhang et al., 1990; Davies and Davies, 2001). Grain fracturing/crushing results in plastic compaction and an irreversible decrease in porosity as shown in Fig. 2.14 (Menéndez et al., 1996; Wong and Baud, 1999).

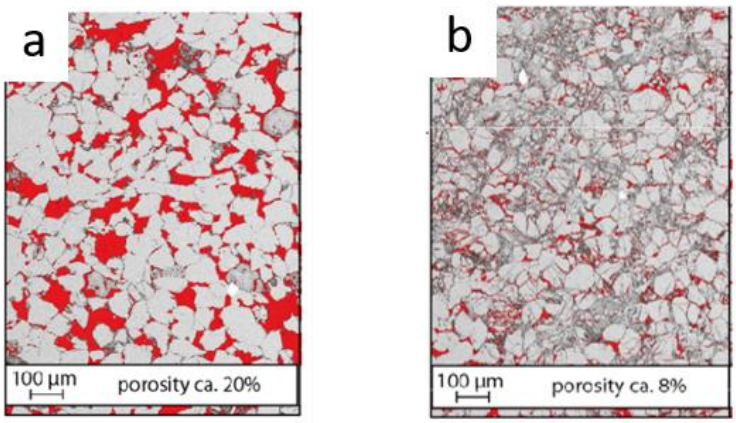

Figure 2.14: Grain crushing results in a significant reduction in porosity (Germaine and Germaine, 2009).

Spheres/discs with various packing configurations provide a useful model of granular media (Fatt, 1958; Walton, 1987). Two main approaches to investigate grain crushing based on the DEM exist. One approach is to replace the grains satisfying a predefined particle breakage criterion with a group of smaller particles (Åström and Herrmann, 1998; Tsoungui et al., 1999; Ciantia et al., 2015; Zhou et al., 2016). The other

approach describes the crushable grain as an agglomerate of bonded particles (Thornton et al., 1996; Robertson, 2000; McDowell and Harireche, 2002; Cheng et al., 2003; Lu and McDowell, 2006; Alonso et al., 2012; Cil and Alshibli, 2014). The latter approach allows handling various types of grain shape but usually is limited to simulations of a small group of particles due to the high computational cost. Besides, the Finite Element Method (FEM) can also be run on each individual particle to account for all forces exerting on the particle (Bagherzadeh Kh. et al., 2011). This approach can model non-spherical grains with shape edges but limited as a 2D investigation currently. In this study, we present a crushing model based on DEM at the grain scale and investigate the effects of compaction on reservoir permeability and productivity (Sun et al., 2018c).

2.5 FLUID-DRIVEN FRACTURE INITIATION

The injection of fluid results in fluid overpressure and a change of stress state in target formations, which may in turn drive the fluid to migrate through porous media and induce fractures. Fluid injection is involved in engineering processes such as CO_2 geological storage, grouting for ground improvement, enhanced oil recovery, waste subsurface disposal, water-flooding for hydrocarbon recovery and hydraulic fracturing (Economides and Nolte, 1989; Lake, 1989; Ayoub et al., 1992; Au et al., 2003; Tsang et al., 2008; Tong and Mohanty, 2016; He et al., 2017; Tang et al., 2017).

Although these engineering practices share a similar operation, the objectives of fluid injection may vary. For instance, hydraulic fracturing is a well stimulation technique involving the creation of localized flow path to increase the reservoir conductivity. Meanwhile, water-flooding is known as secondary recovery requiring a mitigation of localized features to maintain the reservoir pressure. Therefore, better understandings of the injection-induced fracture behavior are of great importance for various engineering

applications. In this study, we attempt to address two problems: (1) the grain-scale mechanism of fracture initiation induced by fluid flow; and (2) the effects of fluid characteristics and stress state on the injection-induced fracture initiation.

The most commonly used numerical approaches for rock mechanics problems are continuum- and discrete-based methods (Jing and Hudson, 2002; Lisjak and Grasselli, 2014). The continuum approaches, e.g., linear elastic fracture mechanics (LEFM), have been extensively used to investigate the initiation and propagation of fluid-driven fractures in cohesive host rocks (Pollard, 1973; Rubin, 1995; Yew and Weng, 2014). Discrete approaches commonly refer to the discrete element method (DEM) which treats the rock as an assembly of blocks or particles (Cundall and Strack, 1979). Neither the continuum nor the discrete approach has absolute advantages and the choice is often based on the investigated system and the problem length scale (Jing and Hudson, 2002). For instance, the concept of energy release rate commonly used in continuum approaches is usually not applicable to fracture initiation in unconsolidated formation due to its lack of tensile strength and coupled response to fluids (Zhang et al., 2013; Hoek and Martin, 2014; Feng et al., 2016; Sun and Huang, 2017; Liu et al., 2018a).

Experimental studies show that micromechanical processes characterize the fracture process in rocks (Lockner et al., 1991; Benson et al., 2008; Daigle et al., 2017). In this study, fracture initiation manifests through opening-mode particle displacement. This work uses the resolved CFD-DEM approach to study how particle-scale processes contribute to fluid-driven fracture initiation at the grain scale.

Chapter 3: Discrete Element Modeling of Indentation Tests to Investigate Mechanisms of CO_2-Related Chemo-Mechanical Rock Alteration[1]

3.1 INTRODUCTION

Indentation tests have been widely adopted to study the mechanical behavior of different materials (Oliver and Pharr, 2004; Kumar et al., 2012). The assessment of rock mechanical degradation subject to CO_2-related alteration can be easily and quickly achieved by indentation tests. In this chapter, we present a pore-scale model based on the DEM to perform numerical simulation of rock indentation tests. In the model, the degradation of cementation is ascribed to the degradation of microscopic parameters that govern particle cementation. Thus, the model can be used to provide quantitative prediction and qualitative understanding of physical parameters that affect cementation at the grain scale and therefore rock integrity when exposed to CO_2.

3.2 VERIFICATION AGAINST ANALYTICAL MODEL

In this section, the DEM-BPM model is verified against the analytical Cavity Expansion Model (CEM) (Alehossein et al., 2000). Marsh (1964) suggested the analogy between the material response under an indenter and the expansion of a spherical or cylindrical cavity. The cavity expansion model was then developed for wedge-shaped and conical indentations (Johnson, 1970). Alehossein et al. (2000) extended this model to include the indentation of rock by blunt indenters based on a set of fundamental assumptions: (1) material volume is sufficiently large; (2) problem is solved for spherical or cylindrical symmetry; (3) characterization of three distinct zones including damaged

[1] Zhuang Sun, D. Nicolas Espinoza, Matthew T. Balhoff (2016). Discrete Element Modeling of Indentation Tests to Investigate Mechanisms of CO_2-Related Chemo-Mechanical Rock Alteration. Journal of Geophysical Research: Solid Earth 121 (11), 7867-7881.
I performed the research and wrote the manuscript with support from M.T. Balhoff and D.N. Espinoza.

core, plastic shell and elastic expansion. The relationship between load and indentation depth during the indentation tests, from which the mechanical properties can be obtained, is described by a system of equations in the CEM. For the sphere indentation

$$\frac{P}{q} = \frac{1}{K_p - 1}\left[\frac{(n+1)K_p}{K_p + n}\xi_*^{n(K_p-1)/K_p} - 1\right] \tag{3.1}$$

$$\frac{d\xi_*}{d\delta} = \frac{1-\delta}{\delta(2-\delta)}\left[-\xi_* + \frac{\gamma(\delta)}{(1+\mu)\xi_*^{2/K_d} - \mu\xi_*^{-2/K_p+1}}\right] \tag{3.2}$$

$$\gamma(\delta) = \frac{\sqrt{\delta(2-\delta)}}{2\kappa(1-\delta)} \tag{3.3}$$

where P is the load exerted on the indenter; q is the uniaxial compressive strength of the rock; K_p and K_d are passive coefficient and dilatancy coefficient; n is the dimension index; ξ^* and δ are the scaled radius and scaled indentation depth; coefficient μ is determined by K_p, K_d and shear modulus of the particle G; coefficient κ is determined by G, q and K_p. K_p and K_d are respectively determined by the internal friction angle ϕ, and the dilatancy angle ψ. The detailed relationships of the coefficients can be found elsewhere (Alehossein et al., 2000). Overall, the parameters for the CEM are q, G, ϕ and ψ.

In order to verify our model against the CEM, we simulated a sphere indentation test on a cylindrical, face-centered cubic (FCC) crystal structure particle packing (porosity $\approx$ 0.26). The radii of the sphere indenter and the particles are 0.04 m and 0.001 m, respectively. The particle packing is 0.024 m in diameter and 0.048 m in height, containing 3825 particles and 20528 bonds with the bottom fixed and all other boundaries free. The model schematic is shown in Fig. 3.1a.

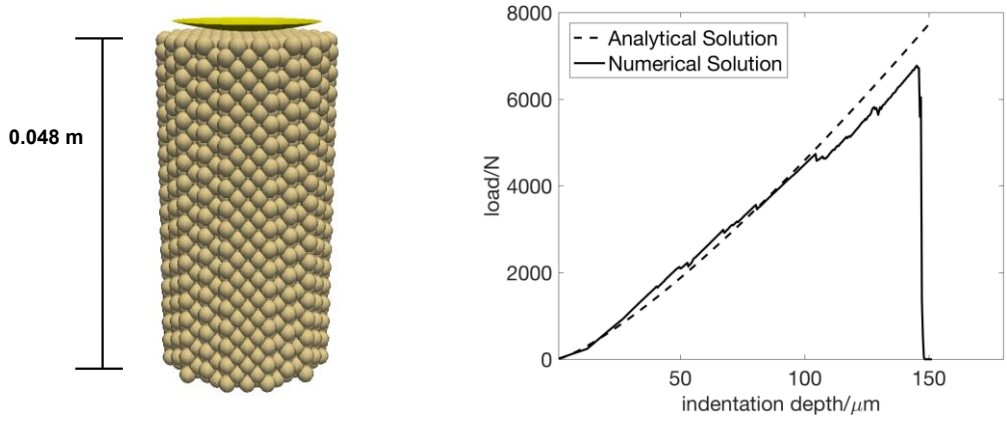

(a) (b)

Figure 3.1: (a) Schematic of the verification simulation. (b) Verification of the numerical solution against the CEM analytical solution.

The microscale parameters for particle-particle contacts and bonds are given in Table 3.1. Fig. 3.1b shows the verification of the numerical model against the CEM, the parameters of which are acquired from simulation results in Fig. 3.2. When load reaches ~ 6500 N, macrocracks induced by the accumulation of aligned microcracks fracture the entire digital sample. Similar indentation test results based on another discrete element code PFC3D have been previously observed (Zhang et al., 2011).

Table 3.1: Microscale parameters for the verification model

Particle-particle contacts	Bonds
E_c = 7 GPa	E_b = 7 GPa
k_T/k_N = 1	k_T/k_N = 1
μ = 0.5	R_b = 0.001 m
ρ = 2650 kg/m^3	σ_c = 5 MPa
	τ_c = 30 MPa

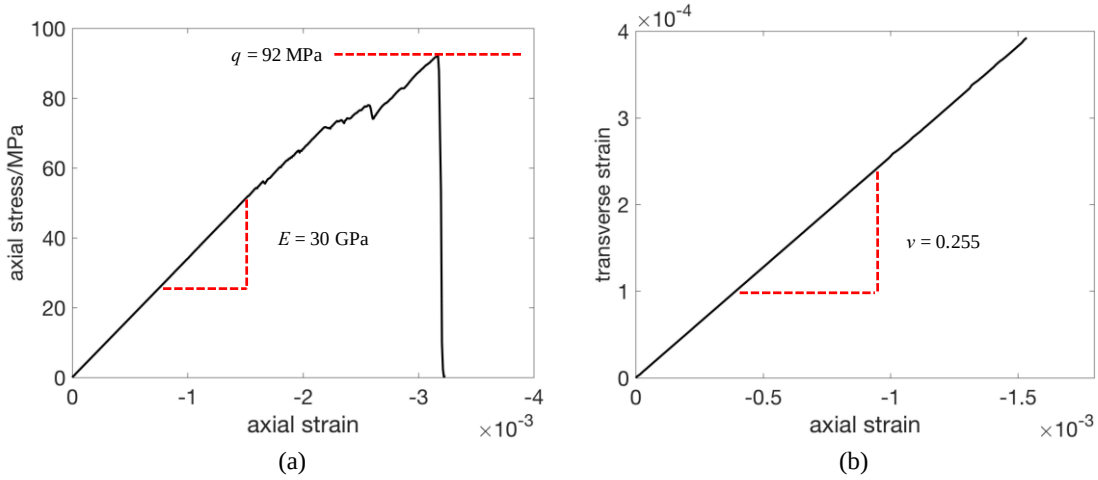

Figure 3.2: Simulation results of the uniaxial compression test.

A uniaxial compression numerical test was performed to obtain the macroscale inputs for the CEM: elastic modulus E = 30 GPa, Poisson's ratio ν = 0.255, and the uniaxial compressive strength q = 92 MPa (Fig. 3.2). The internal friction angle ϕ is 30° and the dilatancy angle ψ is 7.5°, both of which are consistent with typical sandstones (Schellart, 2000; Alejano and Alonso, 2005).

3.3 Results and Discussion

3.3.1 Validation against laboratory experiments

Recent experimental work included indentation tests conducted on two samples of Entrada sandstone, one altered by CO_2-charged brine and one unaltered (Sun et al., 2016a). The related rock outcrops were bleached by natural leakage of CO_2-brine mixture at Crystal Geyser, Utah, with evidence of cement alteration (Wigley et al., 2012; Major et al., 2014). The samples were cut into 1 inch cubes for the indentation tests. A standard Vicker's indenter was inserted into the sample until the pre-set maximum load of 5 N was reached. The grain size varied from 50 to 100 μm.

To validate our model against the load-indentation depth curves obtained from the experiments, a numerical simulation was performed using a Vicker's indenter on a randomly generated assembly of bonded particles with a uniform size distribution (50 to 100 μm) as shown in Fig. 3.3. Note that the size distribution which can also have an impact on the simulation result is out of the scope of this study (Minh and Cheng, 2013).

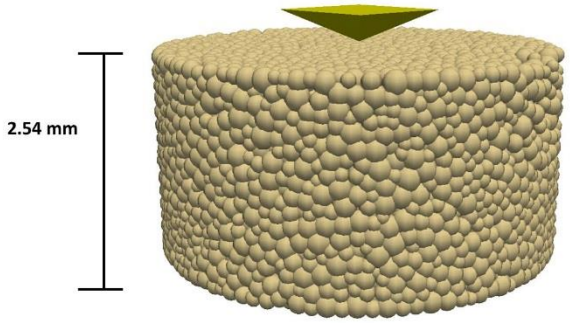

Figure 3.3: Schematic of the validation model. Packing: 5.08 mm (0.2 inch) in diameter and 2.54 mm (0.1 inch) in height; 13760 particles and 21371 bonds.

A cylindrical sample shape is adopted for computational efficiency; the damaged zone front propagates as a sphere (Alehossein et al., 2000). The sample is 5.08 mm (0.2 inch) in diameter and 2.54 mm (0.1 inch) in height with 13760 particles and 21371 bonds. The bottom is fixed and all other boundaries are free. In order to ensure that boundaries were unaffected during the indentation, a test case containing a confining wall, which prevents the outer surface from radial displacement, was implemented. The indentation test results for either free or confining boundary conditions are almost identical, which demonstrates the boundary effects are negligible in our simulations.

Parameter λ is a dimensionless parameter representing the radii of bonds, i.e. the degree of cementation. With two arbitrarily connected particles i and j, the radius of the bond $R_{b,ij} = \lambda(R_i + R_i)/2$. Note that λ can be defined in other ways; for example, Potyondy

and Cundall (2004) use $\min(R_i + R_j)$ instead of $(R_i + R_j)/2$. The viability of this λ definition to reproduce the cement behavior was demonstrated in the literature (Obermayr et al., 2013). Numerically, λ ranges from 0 (no cementation) to 1 (full cementation).

To investigate the mechanism of CO_2-related alteration, the following assumptions are made:

- Chemical alteration manifests through the alteration of cements rather than the dissolution of rigid grains based on experimental observations and field work (Wigley et al., 2012; Major et al., 2014). These studies suggest that altered Entrada sandstone rocks have been "bleached" losing their color and hematite grain coating and cement. Grain reduction is also a possibility and impacts mechanical changes as shown by DEM simulations by Shin and Santamarina (2009). Our analysis in this chapter, however, does not include the possibility of full grain dissolution.
- Both particle-particle and bond-particle contacts elastic moduli are assumed constant and equal to 7 GPa, which corresponds to a Hertzian contact with quartz particles and deformation δ/R about 0.2.
- The size of cements (parameterized by λ) reduces, while all other properties are invariant, after the CO_2-alteration. This assumption is based on CO_2-related reactions only occurring at the surface of cements.

Using the microscopic parameters provided in Table 3.2, results of the unaltered sandstone were produced. The stiffness ratio is set to maintain a physically-reasonable Poisson's ratio (< 0.5). The particle density ρ is equal to quartz density. We assume a typical friction coefficient $\mu = 0.5$. All these parameters are constant throughout this study. The calibrations of the bond normal strength σ_c and the bond tangential strength τ_c were performed against the experimental indentation test on unaltered sandstone resulting on a good qualitative fitting with $\lambda = 0.5$. Typical values of σ_c and τ_c vary from 5 MPa to 50

MPa for sandstones (Thomas and Slate, 1963; Hobbs, 1964; Cho et al., 2007; Hsieh et al., 2008; Zhang and Wong, 2012). The indenter is implemented as a wall with stiffness several magnitudes larger than the particle stiffness. As a result, the stiffness used to calculate the forces between them is only determined by the particle stiffness. The indenter velocity is constant and low enough to make sure the sample undergoes quasi-static deformation during the indentation.

Table 3.2: Microscale parameters for the validation model

Particle-particle contacts	Bonds
E_c = 7 GPa	E_b = 7 GPa
k_T/k_N = 2	$\bar{k}_T / \bar{k}_N$ = 2
μ = 0.5	λ = 0.5
ρ = 2650 kg/m^3	σ_c = 10 MPa
	τ_c = 40 MPa

The validation result is shown in Fig. 3.4. The numerical result reproduces both the loading and unloading processes. Hysteresis is the result of the unrecoverable plastic deformation during indentation, which might be represented by microcracks at the grain scale. Fig. 3.4b shows number of broken bonds from simulations and supports this hypothesis. Initially, the indentation is elastic with no bond breakage; shortly after microcrack appears, indentation continues with irreversible damage. Comparison of Figures 3.4a and 3.4b shows that the decreases of slope on the numerical load-indentation depth curve is an indication of the occurrence of a macrocrack (accumulation of aligned microcracks).

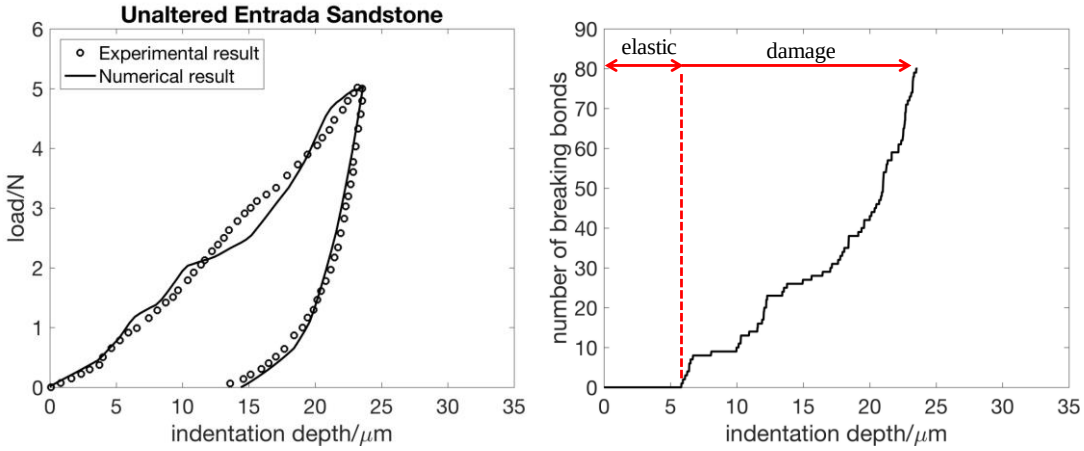

Figure 3.4: Validation results for unaltered Entrada sandstone. (a) Experimental and numerical (λ = 0.5) load-indentation depth curves. (b) Evolution of the number of broken bonds, i.e., microcracks.

The comparison between our model and the experimental result example for CO_2-altered Entrada sandstone is shown in Fig. 3.5a. We change only the coefficient λ (the degree of cementation is reduced); all other parameters are identical to those for the unaltered sandstone as given in Table 3.2. The corresponding evolution of microcrack count is shown in Fig. 3.5b.

More microcracks are shown under the same pre-set maximum load due to the weaker cementation. The curve of microcrack count evolution is also smoother for λ = 0.29 than for λ = 0.5 since the whole sample is weaker. In summary, the change of bond size alone can describe the mechanical rock degradation due to CO_2-related alteration. The following sections explore the impact of other bond microscopic parameters. Invariable parameters in the sensitivity analysis are the same as given in Table 3.2.

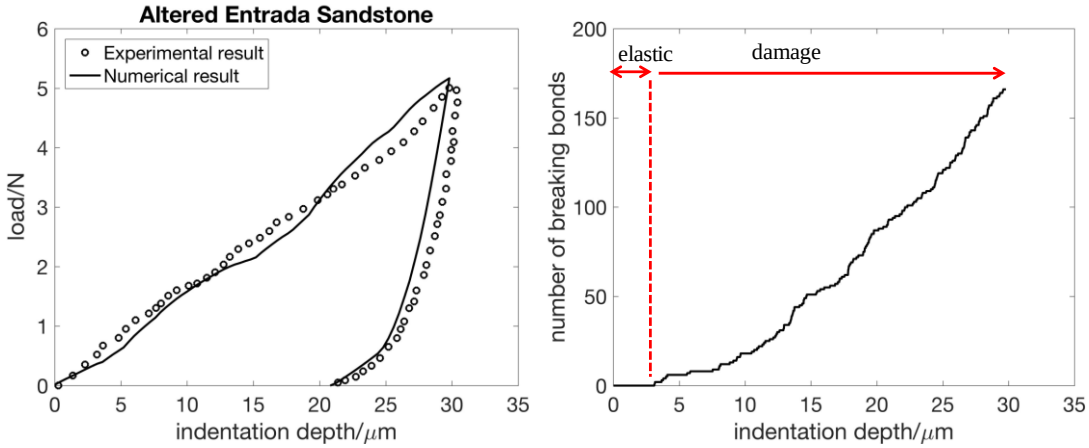

Figure 3.5: Validation results for CO_2-altered sandstone. (a) Experimental and simulational load-indentation depth curve of CO_2-altered sandstone with λ = 0.29. (b) Evolution of the cumulative microcrack count. The pure elastic region is smaller than that of the unaltered sandstone.

3.3.2 Effect of bond size

Fig. 3.6 shows the effect of bond size by changing λ from 0.01 to 0.9.

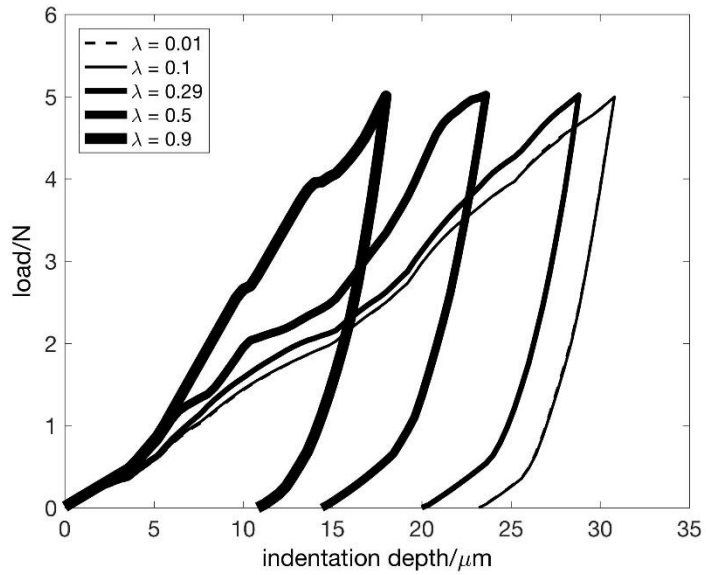

Figure 3.6: Effect of bond size. A larger λ corresponds to a stiffer sample that is harder to break.

The larger bond size makes the sample stiffer and harder to break. For small λ, unloading occurs less steep than large λ due to the lower sample stiffness and the loading curve has fewer sudden slope drops (if the sample contains no cementation, no slope drop would occur). Fig. 3.6 shows the general trend of mechanical degradation associated with the reduction of λ. In the cases of $\lambda = 0.1$ and $\lambda = 0.01$, the plots almost overlap each other, which indicates that when the degree of cementation is very low, the cement size has little impact on the global mechanical behavior.

3.3.3 Effect of bond elastic modulus

Chemical alteration may also result in a change of the bond elastic modulus. At the microscale, increases of bond elastic modulus cause stiffer but easier to break bonds (for a fixed bond strength). Fig. 3.7a shows that the overall mechanical response is almost insensitive to bond elastic modulus.

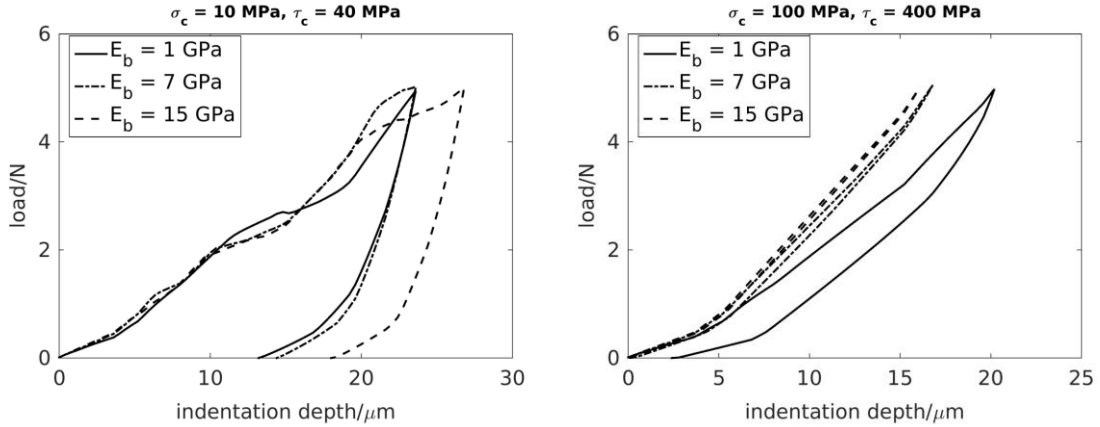

(a) (b)

Figure 3.7: (a) Effect of bond elastic modulus when σ_c = 10 MPa and τ_c = 40 MPa. Various bond elastic moduli have little impact on the global mechanical behavior. (b) Load-indentation depth curves for different bond elastic moduli when σ_c = 100 MPa and τ_c = 400 MPa, which guarantees no bond breakage during indentation tests. After excluding the impact of bond strength, the effect of bond elastic modulus is apparent.

The load-indentation depth curve is conditioned by the competition between bond breakage and elastic modulus. Larger bond elastic modulus tends to increase the stiffness while the associated bond breakage also becomes easier. The consequence of this competition is that the large number of broken bonds induced by larger bond elastic modulus offsets the additional sample stiffness, i.e., the mechanical response behaves similarly for different bond elastic moduli.

We performed a numerical simulation in which both the normal and tangential bond strength were large enough (σ_c = 100 MPa and τ_c = 400 MPa) to ensure no bond breakage occurs during the indentation tests. Thus, only the bond elastic modulus affects the load-indentation depth curves. As shown in Fig. 3.7b, the curves are different, unlike Fig. 3.7a in which they were nearly identical; larger bond elastic modulus correlates with stiffer mechanical behavior. Moreover, in the loading and unloading processes hysteresis is much smaller (than as shown in Fig. 3.7a) as a result of the plastic deformation initiated by the bond breakage. The hysteresis is less evident as the bond elastic modulus is increased, which indicates that in the case of the small bond elastic modulus in our model, additional hysteresis can occur due to the inelasticity. For the validation cases in Section 3.3.1 where E_b is 7 GPa the hysteresis of which is due to pure elasticity is almost negligible.

To summarize, rock mechanical properties are not as sensitive to bond elastic modulus as the bond size. The reason is that the bond breakage becomes harder for larger bond radius whereas easier for larger elastic modulus; the bond breakage plays two opposite roles for two microscopic parameters. Thus, even if the CO_2-related alteration tends to alter the cement elastic modulus, cement size is the parameter which determines the ultimate mechanical behavior.

3.3.4 Effect of bond strength

The bond strength in both normal and tangential directions can also affect the mechanical response. The effect of bond strength is shown in Fig. 3.8.

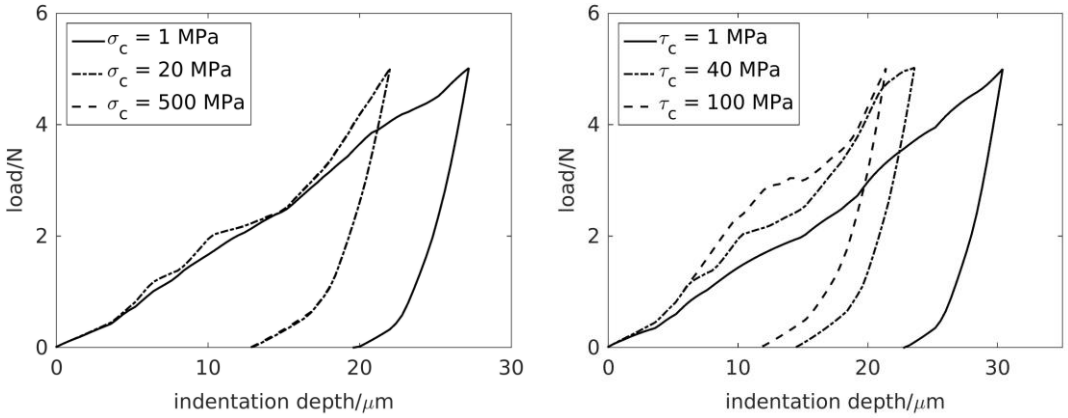

Figure 3.8: Effect of bond strength, specifically (a) normal strength and (b) tangential strength. The normal strength has little impact on the sample stiffness. When the strength is increased from 20 MPa to 500 MPa, no difference occurs on the load-indentation depth curves due to the bond breakage is determined by the bond tangential strength. Larger bond tangential strength can lead to a stiffer sample due to the bonds harder to break. The tangential strength functions within a larger range compared with the normal strength.

The sample stiffness is mostly unaffected by the bond normal strength which can only have an indirect impact through the bond breakage. However, the sample becomes harder to break when the normal strength is increased. Similar to Fig. 3.6, when the normal strength is extremely small, the curve tends to be smooth. In Fig. 3.8a, when the normal strength increases from 1 MPa to 20 MPa, the sample becomes slightly stiffer since bonds are harder to break. However, when the normal strength increases from 20 MPa to 500 MPa, the resulting load-indentation depth curves almost overlap because the bond breakage is controlled by the bond tangential strength if the normal strength is too large.

Although normal and tangential strengths have some similarities, a study of tangential strength is necessary to determine the dominant direction of bond breakage. As in the case for normal strength, the tangential strength indirectly affects the sample stiffness through microcracks. Comparing Fig. 3.8a and Fig. 3.8b, the tangential strength results in more variability of load-indentation depths than the normal strength, indicative that more bonds tend to crack in the shear direction rather than the normal direction. However, the microcracks in shear and normal directions should not be confused with shear and tensile cracks, which are classified by shear-tensile ratio $|\tau/\sigma|$ regardless of broken bond types (Shimizu et al., 2011). Moreover, the smaller bond strength leads to the smoother load-indentation depth curve, which indeed can be observed for almost all bond microscopic parameters. The existence of strong bonds leads to the fluctuation of curves.

The effects of bond microscopic parameters have been investigated to reveal the possible grain scale mechanism of the CO_2-related alteration. Compared with bond elastic modulus and normal bond strength, the tangential bond strength is more likely to contribute to the mechanical alteration. Variation of tangential strength (1 MPa to 40 MPa) has a comparable effect on indentation curves to that of bond size. However, it is unrealistic for CO_2-acidified water to reach the contact-particle interface (and degrade its strength) before reacting with the outer cement, unless it is a permeable cement. Thus, DEM simulations suggest that the cement size is the primary variable that affects CO_2-related natural alteration of hematite-coated Entrada sandstone.

Although the effects of bond parameters are studied and discussed separately, they have a synergistic effect on mechanical response. The microscale parameters should not be treated as a group of adjustable numerical parameters to recover the macroscale properties; rather they should be properly calibrated within a reasonable range. The relationship between microscale and macroscale parameters is always a challenge in the DEM

especially for 3D simulation. In our model, the simulation of indentation test provides a tool to construct the corresponding relationship.

3.3.5 Effect of rock heterogeneity

Rock heterogeneity also affects the results of indentation tests. In the experiments performed by Sun et al. (2016), five sets of indentation tests were performed on the unaltered and altered sandstones, respectively, in order to demonstrate the CO_2-related alteration. Several indentations were performed because the resulting load-indentation depth curves are different even for the same sandstone due to the rock heterogeneity. It is rather complicated to study the effect of heterogeneity with all factors taken into account. In this section, we only study the heterogeneity related to cement size and indent position.

The heterogeneity due to cement size is investigated for fixed indenter position and microstructure of grains. Fig. 3.9 shows the relationship between λ and the indentation depth corresponding to the pre-set maximum load of 5 N, which is an indicator of the rock mechanical strength.

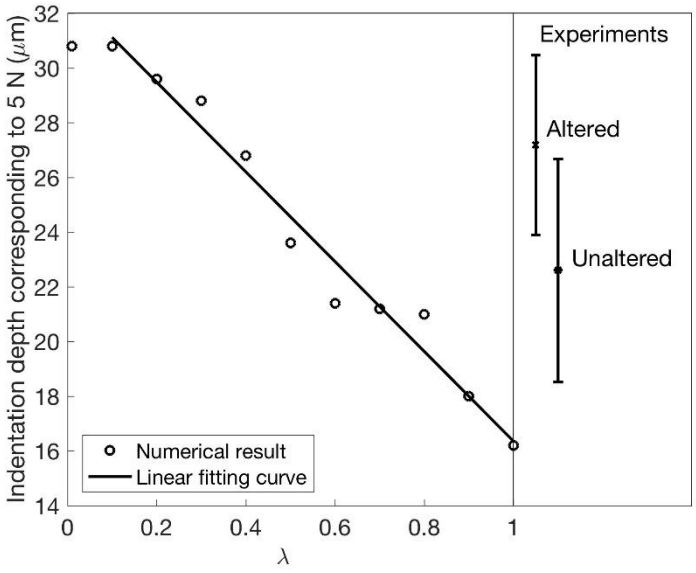

Figure 3.9: Relationship between λ and the indentation depth corresponding to the pre-set maximum load of 5 N during indentation. The experimental results of the unaltered sandstone and altered sandstone are compared with the numerical result to obtain their different ranges of λ. The experimental error bars result from the heterogeneity of sandstones.

When λ is too small (< 0.1), the degree of cementation has almost no effect. An approximately linear relationship is obtained for λ between 0.1 and 1. Experimental results for altered and unaltered sandstones have error bars due to sample heterogeneity, which can be attributed to the spatial heterogeneity of cement size. Based on Fig. 3.9, for the unaltered sandstone, λ ranges from 0.37 to 0.88; while for the altered sandstone, λ ranges from 0.14 to 0.54. Note that for the same microstructure and indenter position numerical simulations always yield higher indentation depth for lower values of λ (Fig. 3.6). The CO_2-related alteration can be described by the change of λ parameter range.

Scatter of results may also occur as a result of the indent position. In other words, the indenter encounters different grain microstructures at different landing positions. Moreover, the surface is polished in experiments, but rough in the DEM study; thus,

additional scatter of results is created numerically due to the roughness. To investigate the effect of indenter position, five positions were tested numerically: #1 the base case (0 m,0 m), #2 (0.0001 m, 0.0001 m), #3 (0.0001 m, -0.0001 m), #4 (-0.0001 m, 0.0001 m), and #5 (-0.0001 m, -0.0001 m). To be consistent with Section 3.3.1, λ is assumed to be 0.5 and 0.29 for unaltered and altered sandstones, respectively, i.e. the cement size is assumed constant in the sample. Fig. 3.10 shows the load-indentation depth curves corresponding to different indent positions.

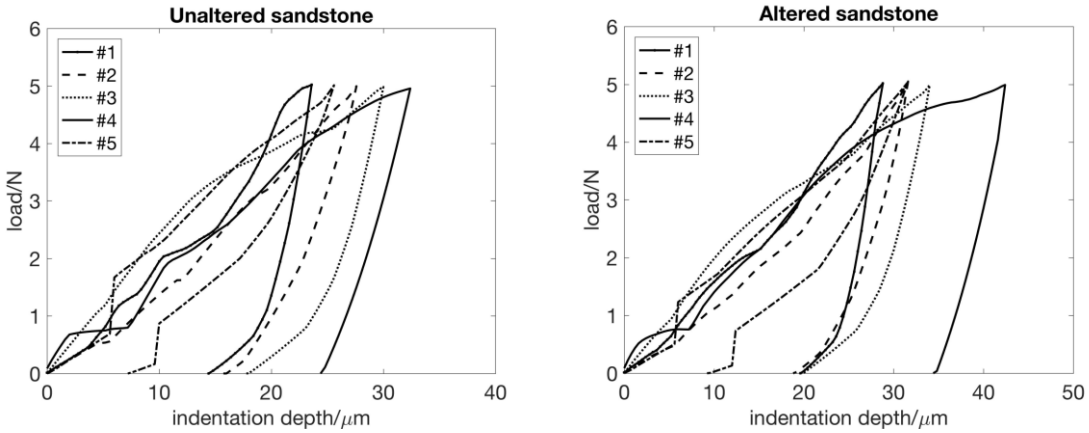

Figure 3.10: Effect of indent positions on (a) unaltered sandstone and (b) altered sandstone. Load-indentation depth curves show variability because the indentation depth is smaller than the characteristic size of heterogeneity of the microstructure. The curves are from five different indent positions.

Due to the observed variability of load-indentation depth curves of both experimental and numerical indentations, a single curve is not sufficient for quantifying the effect of CO_2-alteration. Indentation hardness and Young's modulus are calculated (using equations in Sun et al. (2016)) from the numerical simulations; mean and standard deviations are presented in Fig. 3.11.

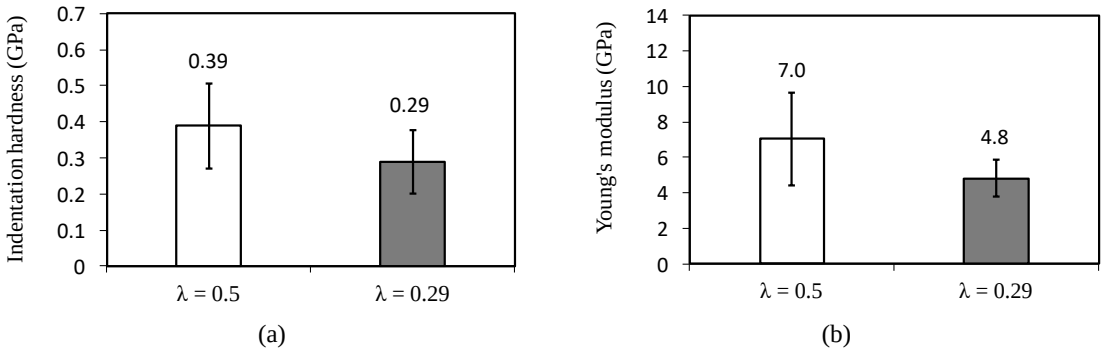

Figure 3.11: Statistical analysis of results from Fig. 3.10: (a) indentation hardness and (b) Young's modulus. $\lambda = 0.5$ (unaltered), $\lambda = 0.29$ (altered).

The indentation hardness and Young's modulus of the altered sandstone are lower on average than the unaltered sandstone as a result of smaller λ ascribed potentially to CO_2-alteration, but with large and overlapping error bars. However, the altered sandstone always has a lower hardness and Young's modulus with the same indenter position. The error bars in Fig. 3.11 are calculated from results of indentation tests on different indent positions and show the impact of local microstructure, e.g. the indentation curves will be affected by whether the numerical indent is performed on top of a grain or in-between grains.

In order to study other possible sources of scatters in the results, different random seeds were also used to study the effect of initial packing randomness while the grain size distribution and volume fraction of grains are kept the same. Fig. 3.12 shows the effect of randomness on load-indentation depth curves.

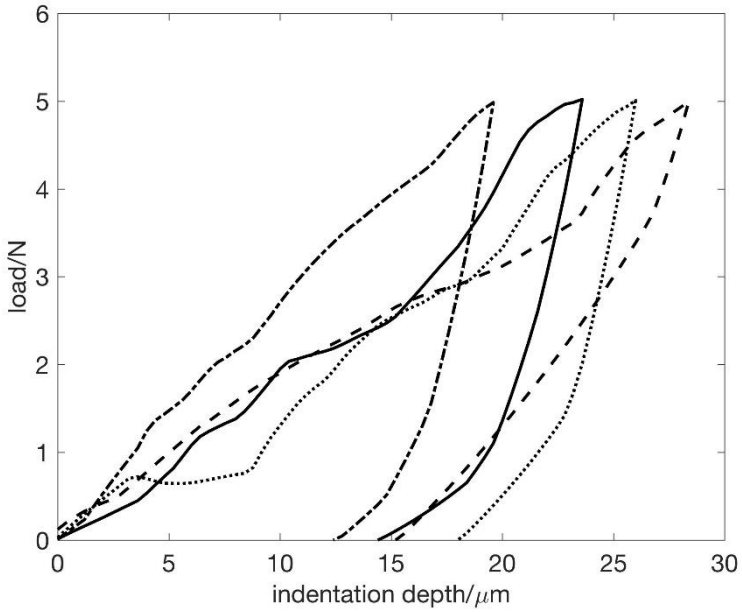

Figure 3.12: Effect of the randomness. Other factors including the grain size distribution, volume fraction of grains and cement size are invariant.

Fig. 3.12 (similarly to Fig. 3.10) demonstrates sensitivity of the indentation curve to initial conditions (different microstructures the indenter encounters at the grain scale). Despite the scatter of results, both Fig. 3.10 and Fig. 3.12 show statistically meaningful trends.

3.4 CONCLUSIONS

In this chapter, a model coupling the Discrete Element Method (DEM) and the Bonded-Particle Model (BPM) is developed to investigate mechanisms of CO_2-related chemo-mechanical alteration of rocks. The BPM adopted here is proven to be numerically robust even with large deformations and timesteps. The high performance computing capability of LIGGGHTS enables our model to be implemented with up to 10^8 particles. The main parameters for the BPM are size, stiffness, and strength of the bonds. The indentation test is used to validate our model and obtain a set of model parameters. To

minimize the number of adjustable parameters, most parameters are fixed in reference to either quartz properties or typical values from the literature. The normal and shear strength of bonds are varied to fit the indentation load-indentation depth curves. The model inputs from such a parameterization is able to reproduce the mechanical behavior of Entrada sandstone.

Variation of bond size seems to be the most likely variable affecting the mechanical alteration of Entrada sandstone by CO_2. Evolution of microcracks reveals the plastic deformation. The capability of the evolution of microcracks to represent the plastic deformation is further proven by studying the hysteresis of indentation tests with no bond breakage. Sensitivity analysis of bond parameters confirms bond size as the most likely parameter responsible for Entrada sandstone alteration and tangential strength as the second most likely. To conclude, our simulation results demonstrate that:

- The Bonded-Particle Model can model indentation on cemented sandstones.
- For sandstones with interparticle cements more susceptible to CO_2-water mixture alteration than grains, the numerical results support our hypothesis that CO_2-related mechanical rock degradation in Entrada sandstones can be ascribed to the degradation of interparticle cementation.
- The CO_2-related degradation on cementation in Entrada sandstone is likely due to the reduction of cement size, which indicates that the CO_2-alteration occurs on the surface of cements.

Chapter 4: Discrete Element Modeling of Micro-Scratch Tests to Investigate Mechanisms of CO_2 Alteration in Reservoir Rocks[2]

4.1 INTRODUCTION

Micro-scratch tests have been broadly used to investigate the mechanical behavior of different materials (Wredenberg and Larsson, 2009; Akono et al., 2011). In the oil and gas industry, scratch tests have been adopted to measure the hardness, strength, and scratch toughness of sedimentary rocks (Adachi et al., 1996; Richard et al., 1998, 2012; Schei et al., 2000; Suarez-Rivera et al., 2002; Akono and Ulm, 2012). This chapter presents a pore-scale model based on the DEM to simulate micro-scratch tests and analyze the mechanical behavior of cemented sandstone susceptible to grain cement dissolution. We explore the role of cementing bonds dissolution on large-strain mechanical properties of altered rocks through comparison with micro-scratch tests. We discuss the effects of cement dissolution on brittle to ductile transition and simulate the effect of a reactive fluid front inducing fracture propagation.

4.2 CALIBRATION OF MODEL PARAMETERS

We calibrate the DEM-BPM parameters by conducting a numerical triaxial compression test and comparing it with a real experiment. The digital sample with calibrated parameters should be able to capture the mechanical behavior of a real experimental sample, including elastic coefficients, strength and post-peak behavior. We utilized experimental data from a triaxial test performed on unaltered Entrada sandstone with most grains sized between 50 and 100 μm. Tested Entrada sandstones are from Crystal

---

[2] Zhuang Sun, D. Nicolas Espinoza, Matthew T. Balhoff, Thomas A. Dewers (2017). Discrete Element Modeling of Micro-Scratch Tests: Investigation of Mechanisms of CO_2 Alteration in Reservoir Rocks. Rock Mechanics and Rock Engineering 50 (12), 3337-3348.
I performed the research and wrote the manuscript with support from M.T. Balhoff and D.N. Espinoza.

Geyser, Utah. Some outcrops have been altered by natural leakage of CO_2-rich brine. The sandstone porosity is 8.3% (Espinoza et al., 2018). Fig. 4.1 shows radial and axial strains measured upon deviatoric loading of a sample 25 mm diameter by 54 mm height confined at 0.69 MPa.

The numerical triaxial test applies the same loading path to a random sphere packing with a uniform particle diameter distribution from 50 to 100 μm. The height and diameter of the digital sample are 2.54 mm and 1.27 mm. The sample contains 7,928 particles and 23,178 bonds and has a porosity of 24% (39% without counting cement bond volume). Similar to the experimental triaxial test, appropriate boundary conditions apply a constant confining stress (0.69 MPa) in the radial direction.

Fig. 4.1 shows that the digital sample simulated with DEM is capable to reproduce the bulk mechanical properties of Entrada sandstone, including the elastic modulus, Poisson's ratio and strength. Adjustable parameters are E, k_T/k_N, λ, σ_c and τ_c. Parameter λ is fixed as 0.8 to keep the microscopic parameters within reasonable ranges. Thus, the model calibration results in a unique set of adjustable parameters. Table 4.1 summarizes the calibrated microscopic parameters. The numerical simulation matches post peak behavior of radial strain as well. The simulation calculates radial strain from the displacements of grains located along the outside edge of the sample at the midpoint along its length, in order to mimic the measurement adopted in the experiment. We utilize the DEM simulation parameters calibrated on triaxial loading to run scratch test simulations. DEM microscopic parameters are independent of the stress state. We will explore the sensitivity of micromechanical parameters on rock strength.

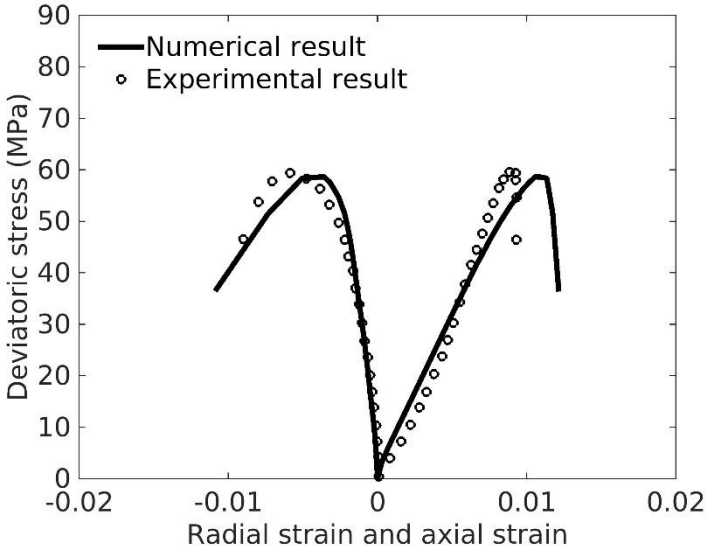

Figure 4.1: Validation of numerical simulation against experimental deviatoric loading triaxial test on unaltered Entrada sandstone with a confining stress of 0.69 MPa.

Table 4.1: Calibrated microscopic DEM-BPM parameters

Particle-particle contacts	Bonds
E = 4 GPa	E_b = 4 GPa
k_T/k_N = 1	$\bar{k}_T/\bar{k}_N$ = 1
μ = 0.5	λ = 0.8
ρ = 2650 kg/m^3	σ_c = 20 MPa
	τ_c = 80 MPa

4.3 RESULTS

4.3.1 Micro-scratch test model

The micro-scratch test numerical model adopts the geometry of experiments performed by Sun et al. (2016a). The digital sample is a 3 mm cube containing 66,950 particles and 183,988 bonds. Similar to the numerical triaxial test illustrated in section 4.2, we utilize a randomly generated sphere packing with a uniform diameter distribution from

50 to 100 μm. A sphero-conical stylus with radius of 200 μm and cone angle 120° scratches the digital sample across the surface at a constant velocity. The scratch length is up to 2 mm and the scratch depth adjusts to maintain constant vertical load on the stylus. The bottom of the sample is fixed and all other boundaries are free. Fig. 4.2 shows the schematic of the micro-scratch test model.

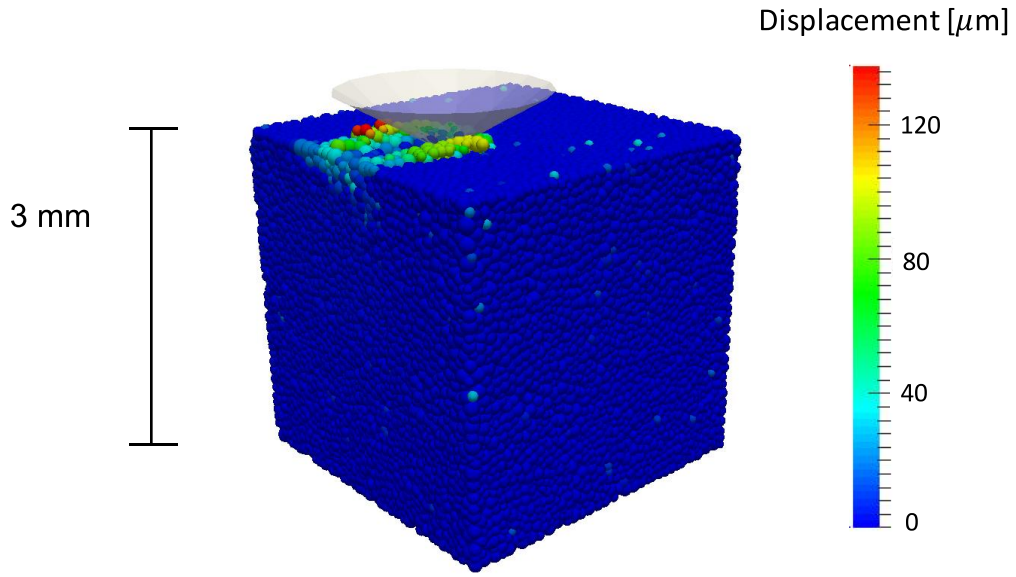

Figure 4.2: Schematic of micro-scratch test model. Sphero-conical stylus moving left to right scratches the surface of the digital sample. Color represents the absolute vertical displacement of particles.

The simulation outputs include (1) forces on the stylus (including horizontal and normal forces), (2) scratch depth and (3) cumulative number of broken bonds. The following equation calculates the scratch toughness K_c [MPa·m$^{1/2}$] (Akono et al., 2011; Akono and Ulm, 2012):

$$K_c = \frac{F_T}{\sqrt{f(d)}} \tag{4.1}$$

where F_T is the horizontal force, and function $f(d)$ is proportional to d^3 in the conical case and d^2 in the spherical case (Akono et al., 2012). Function f for the sphero-conical shape is proportional to $d^{5/2}$ when d is larger than the depth of sphere cap as shown in Eq. 4.2, where d has a unit of μm and f has a unit of m^3.

$$f[m^3] = 3.0 \times 10^{-16} (d[\mu m])^{2.5} \tag{4.2}$$

4.3.2 Validation against experimental micro-scratch test

Sun et al. (2016a) performed three experimental micro-scratch tests on the same unaltered Entrada sandstone, yielding similar results with average K_c = 2.6 MPa·$m^{1/2}$ (Fig. 4.3a). Tests on CO_2-altered Entrada sandstone resulted in average K_c = 2.2 MPa·$m^{1/2}$, indicating a decrease of 15% by exposure to CO_2-brine mixtures over geological time. Experimental micro-scratch tests serve as a benchmark. We performed a DEM "blind" scratch simulation with the calibrated parameters from triaxial tests given in Table 4.1. Normal force is maintained constant at 20 N, which is the same as used in Sun et al. (2016a). The numerical results (Fig. 4.3b) show larger variation of horizontal force than the experimental results, which may result from the surface roughness of sphere packing used in the DEM model (experiments performed on polished sandstone surfaces). Both numerical and experimental tests result in similar values for the scratch toughness (K_c = 3.0 MPa·$m^{1/2}$ and 2.6 MPa·$m^{1/2}$ - Eq. 4.1). Numerical and experimental tests yield similar averaged scratch depth (d = 80 μm). The numerical model results in a slightly higher scratch toughness compared with the experiment, which is likely due to the fact that the numerical simulation ignores the potential interlayer of cement between particles. Section 4.4 discusses the various failure modes induced by different preset normal forces.

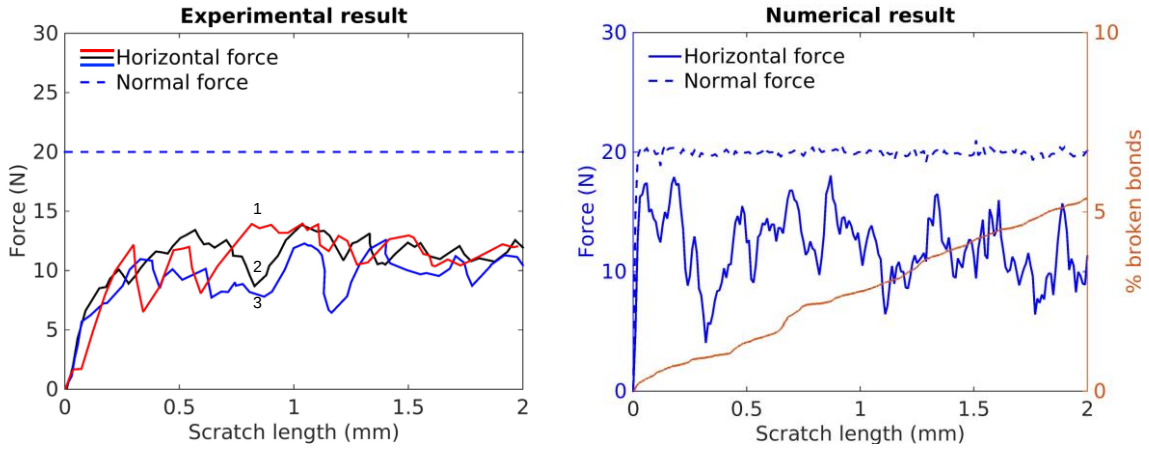

Figure 4.3: (a) Experimental micro-scratch test results including measurements from three scratches on the same Entrada sandstone sample. (b) Example of numerical micro-scratch test result. Rapid variations on the curve of cumulative percentage of broken bonds indicate the occurrence of a fracture.

Fig. 4.3b also shows the evolution of bond breakage when the stylus scratches the digital sample surface. A rapid increase of the percentage of broken bonds indicates brittle fracture propagation, which may result in a rapid decrease of horizontal force. Both surface roughness and brittle fractures contribute to the variation of horizontal force.

Fig. 4.4 shows the evolution of broken bonds (points). The wireframe block represents the shape of the digital sample. Most of the broken bonds appear on the sample surface whereas some may occur further into the sample. The numerical results agree with experimental observations of scratches in which failure localizes around the tested region. A few random bond breakages occur throughout the sample, which was also observed in a DEM axial compression test prior to the peak stress (Hazzard and Young, 2004).

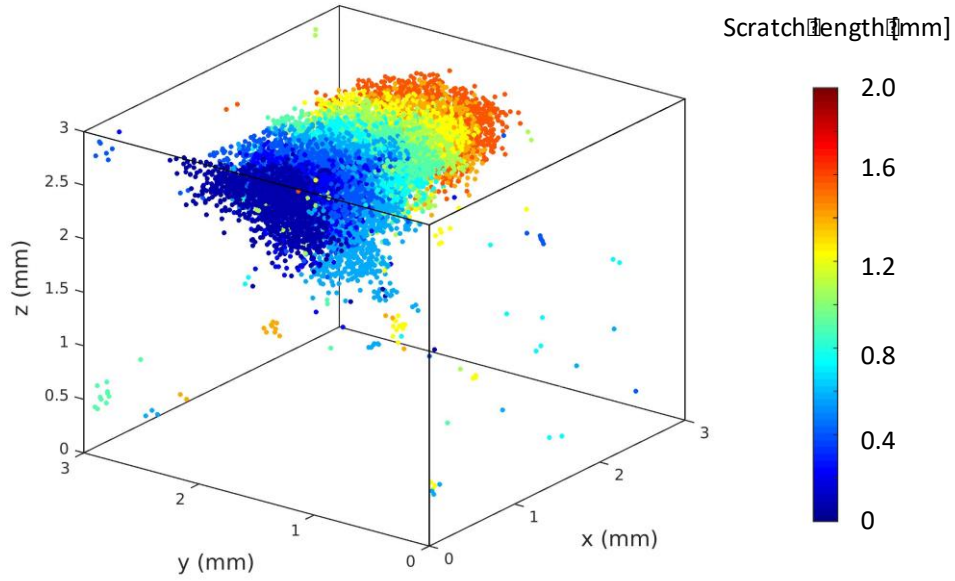

Figure 4.4: Evolution of microcracks during the numerical micro-scratch test. Points represent the bond breakages events. Bond number in total: 183,988; number of broken bonds: 9,888. Percentage of broken bonds: ~5.4%.

4.3.3 Effect of bond microscopic parameters

We performed sensitivity analyses for all bond microscopic properties. We firstly investigate the effect of cement bond size by varying the parameter λ while keeping all other parameters identical as given in Table 4.1. Normal force is constant and equal to 20 N. Since λ = 0.8 corresponds to the unaltered Entrada sample, a physically meaningful parameter λ should range from 0.8 to 0 with decreasing degree of cementation. However, λ is kept larger than 0.4 to make the digital sample strong enough to withstand the scratching. Fig. 4.5a shows the cross-sectional views of residuals of scratch test modeling and Fig. 4.5b shows the calculated scratch toughness along the scratch length for various cement bond sizes. Larger cement bond size results in a stronger sample, which has smaller average scratch depth.

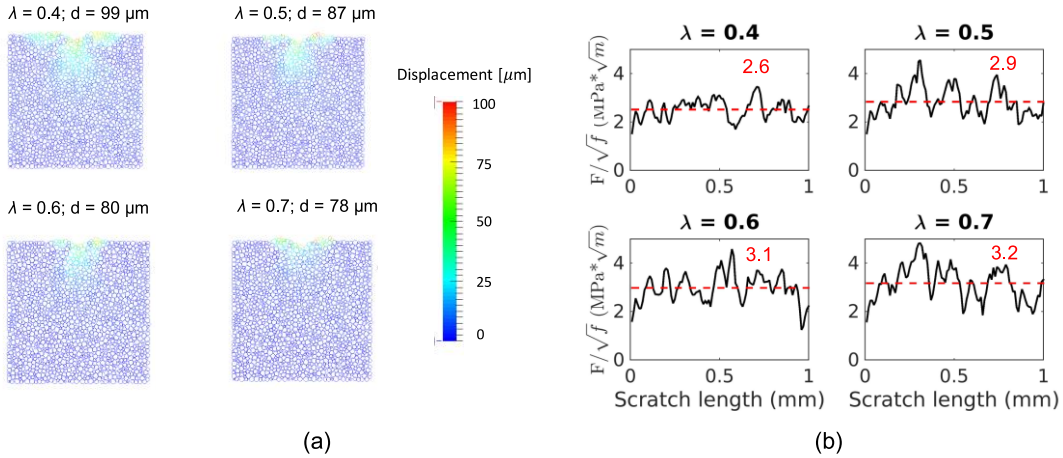

Figure 4.5: Effect of cement bond size. (a) Cross-sectional views of the final states of scratch test modeling. As cement bond size increases, the scratch depth decreases. Color represents the vertical displacement of particles. (b) Dash lines denote the average scratch toughness. As cement bond size increases, the scratch toughness of digital sample increases.

Larger cement bond size λ also leads to a more significant variation of the calculated scratch toughness, which indicates a more brittle sample (see section 4.4). Based on these simulations, we calculate the scratch toughness for various λ based on Eq. 4.1 and Fig. 4.6a shows the results.

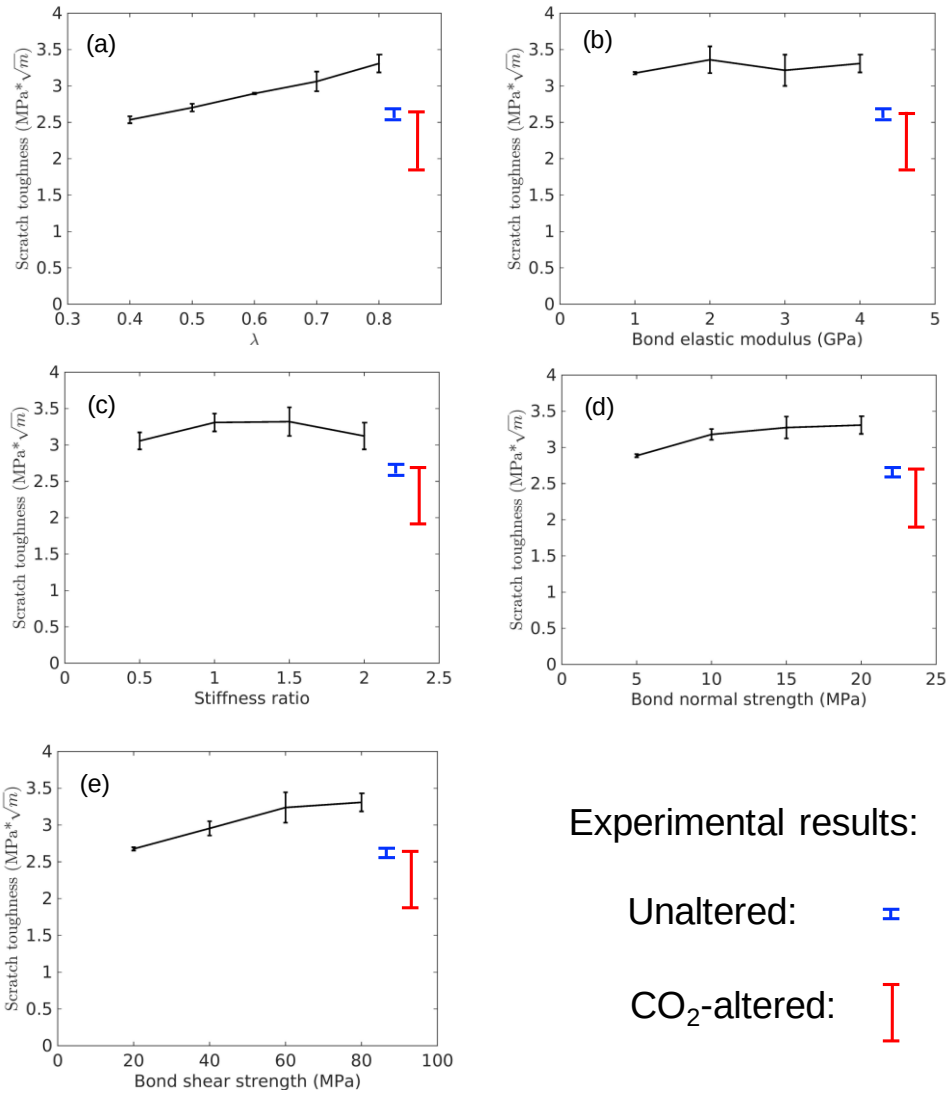

Figure 4.6: Sensitivity analyses results for (a) cement bond size, (b) bond elastic modulus, (c) stiffness ratio, (d) bond normal strength, (e) bond shear strength. Error bars are from 3 various scratch locations. Experimental results for unaltered and altered Entrada sandstones are given with error bars on the top.

As the cement bond size decreases, the digital sample becomes weaker with a smaller scratch toughness. When λ = 0.4, scratch toughness decreases by 17%, which is close to the 15% decrease in scratch toughness of CO_2-altered Entrada sandstone (Sun et

al., 2016a). Numerical test when λ = 0.4 also yields an averaged scratch depth of 97 μm comparable with the scratch depth of 103 μm measured on CO_2-altered sandstone. The scratch toughness shows an approximate linear reduction with parameter λ.

We further performed sensitivity analyses for other bond microscopic parameters including bond elastic modulus, stiffness ratio, normal, and shear strength. The investigated parameter is varied and all other parameters are identical as given in Table 4.1. Particle microscopic parameters are kept constant based on the hypothesis that cements are more susceptible to the CO_2-water mixture attack than the siliceous rigid grains.

Fig. 4.6b shows that the scratch toughness is not strongly affected by bond elastic modulus, which is likely due to competition between elastic modulus and bond breakage. Larger bond elastic modulus leads to stiffer but easier-to-break bonds, which counteracts the additional sample stiffness and results in the similar mechanical behavior for various elastic moduli. Fig. 4.6c shows that the stiffness ratio, similar to the bond elastic modulus, has little impact on the resulting scratch toughness. Fig. 4.6d-e show that the bond strength has a significant impact on the scratch toughness. Shear bond strength appears to be more influential than normal bond strength. Based on the assumption that cement surfaces are more susceptible to the CO_2 alteration than the cement-particle interface, CO_2-related mechanical alteration is most likely to hinge on variation of the cement size rather than on variations of cement bond strength. The sensitivity analyses show consistency with results from chapter 3.

Based on Fig. 4.6a, we plot the reduction of scratch toughness from λ = 0.8 to a given value of λ = 0.7 to 0.4 (Fig. 4.7). A reduction in the parameter λ implies a cement dissolution amount ΔV_c, where V_c is a fraction of the volume of cement over the total solid volume:

$$V_c = \frac{3\lambda^2 - 3\lambda^2\sqrt{1-\lambda^2} - (1-\sqrt{1-\lambda^2})^3}{6\times(\frac{4}{3}+\frac{1}{6}\times\frac{N_{contact}}{N_{particle}})} \times \frac{N_{contact}}{N_{particle}} \quad (4.3)$$

λ is the cement bond size parameter, $N_{contact}$ and $N_{particle}$ are the number of contacts and particles respectively. Eq. (4.3) assumes that each particle connects with $N_{contact}/N_{particle}$ bonds. To derive Eq. (4.3), a bond is separated into two parts with each part assigned a size proportional to the connected particle size (coefficient is λ). Fig. 4.7 shows that a relatively small amount of dissolution in the entire rock leads to a large change in scratch toughness.

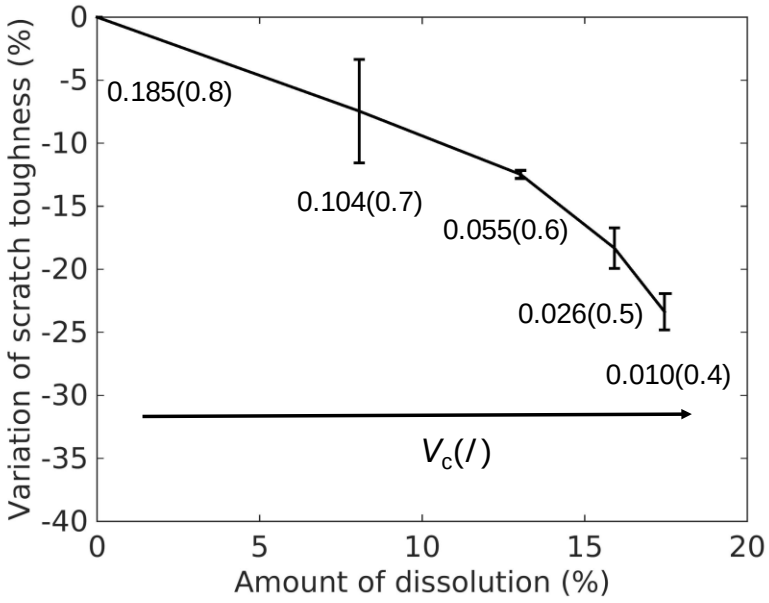

Figure 4.7: Variation of scratch toughness in percentage due to cement dissolution. Dissolution of 17% of the mineral volume at cements can lead to ~25% change in scratch toughness. Error bars come from scratch tests at different locations.

4.4 DISCUSSION

4.4.1 Brittle to ductile transition due to cement size reduction

The failure mode induced by scratching could be ductile and/or brittle depending on material properties and level of stresses around the stylus tip. The ductile mode is

associated with damaged zone development, whereas the brittle mode involves fracture propagation (Huang et al., 2013). To quantitatively study this behavior, we propose two definitions of brittleness based on scratch test modeling.

The first definition is based on bond/cement breakage. In DEM simulations, the occurrence of a fracture is associated with the nucleation and coalescence of broken bonds. For a brittle material, broken bonds tend to align in localized planes and release strain energy quickly. For a ductile material, bonds tend to break gradually and create a diffuse damaged zone. Thus, we propose to use the coefficient of variation of bond breakage rate to quantify brittleness. Eq. 4.4 calculates the brittleness BI_b from bond breakage rate, r_{bb}. The amounts $\mu(r_{bb})$ and $\sigma(r_{bb})$ are respectively the mean and the standard deviation of r_{bb}.

$$BI_b = \frac{\sigma(r_{bb})}{\mu(r_{bb})} \tag{4.4}$$

The second definition is based on energy conservation. A brittle sample tends to store strain energy via elastic deformation and release it quickly with failure. On the contrary, a ductile sample tends to dissipate the energy gradually through the plastic deformation. The brittleness index BI_w is defined based on the ratio between work spent in brittle events W_B and the total energy needed for scratching W_T. Both W_B and W_T can be calculated based on the resulting horizontal force-displacement curves of a scratch test (Hernandez-Uribe et al., 2017).

$$BI_w = \frac{W_B}{W_T} \tag{4.5}$$

Fig. 4.8 shows brittleness calculated based on these two approaches. Both calculations demonstrate the brittle to ductile transition as the cement bond size λ decreases, which is consistent with the observation in Fig. 4.5. In the limit, as λ tends to zero, poorly cemented sandstone exhibits ductile failure. Scratch tests may not be appropriate to test such materials due to the lack of confinement and shear strength.

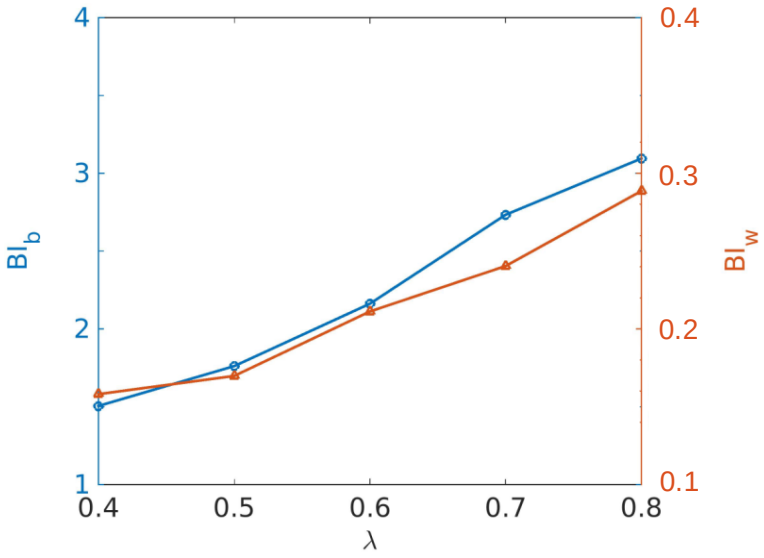

Figure 4.8: Brittleness calculated based on the coefficient of variation of bond breakage rate (BI_b) and the ratio of brittle energy and total energy (BI_w). Two definitions yield similar trend as cement bond size λ decreases, indicating brittle to ductile transition.

Long-term contact with CO_2-acidified brine reduces the size of grain-to-grain cementation in Entrada sandstones. Such alteration reduces rock strength but also reduces brittleness, and thus inhibits brittle fracture propagation and potential leaks through such fractures. However, a weaker reservoir rock can lead to local changes of stresses that affect the structural integrity of the reservoir rock and caprock.

4.4.2 Effect of normal force/scratch depth on scratch toughness calculation

Localized plastic strain may occur during the scratch test when the penetration depth is small compared with the characteristic length of the material (Huang et al., 2013). Therefore, a critical scratch depth is necessary to reach the asymptotic value, which represents the true scratch toughness of the material (Akono et al., 2012; Richard et al., 2012). Normal force on the stylus is constant at 20 N for simulations in the previous

sections. In this section, we attempt to demonstrate that the normal force adopted is sufficient to reach the asymptotic scratch toughness.

The average scratch depth increases as the normal force increases. Our numerical results exhibit opposite behavior to that of experimental scratches in polished media, which show a decreasing trend in scratch toughness with scratch depth toward an asymptotic trend (Akono and Ulm, 2012). Roughness affects the measurement of scratch depth d and, therefore, the scratch toughness calculated with DEM numerical simulations. Thus, a scratch depth smaller than the typical roughness of a random spherical packing ($d < \sim R_{max}$ = 50 μm) leads to erroneous interpretations of scratch toughness as calculated with Eq. (4.1). That is because the surface roughness of the particle packing becomes dominant when the scratch depth is smaller than the particle size.

The normal force (20 N) used throughout this study is reasonable to measure scratch toughness, yet it is close to the region where artifacts may develop because of surface roughness. We assume the characteristic threshold for normal force/depth is constant after contact with CO_2-rich brine. In summary, a critical normal force/scratch depth must be reached to obtain the true scratch toughness. Fig. 4.9 shows that the calculated brittleness decreases as the normal force increases, which indicates that the brittleness is a function of stress state as well.

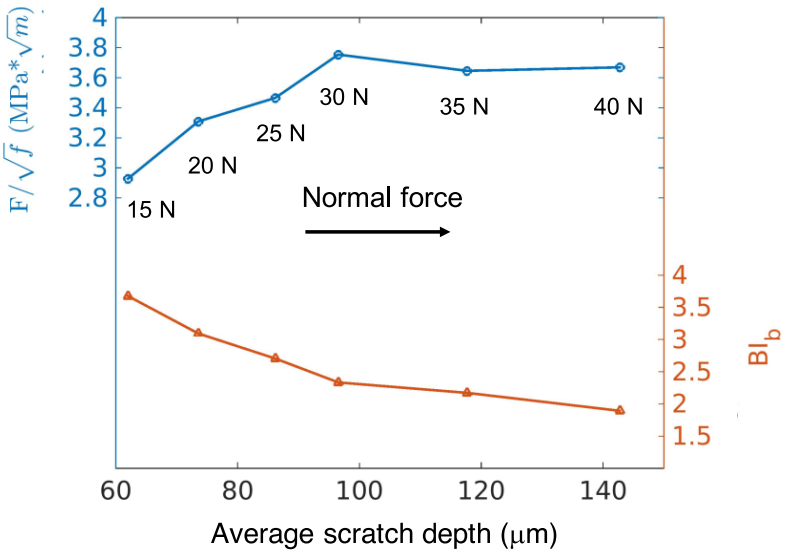

Figure 4.9: The effect of normal force on scratch toughness and brittleness calculation (λ = 0.8). Average scratch depths are plotted instead of the corresponding normal forces. Aymptotic trends of scratch toughness develops when the normal force is sufficient to reach the fracture-driven regime. Brittleness BI_b calculation is based on Eq. 4.4.

Another alternative to investigate the true toughness of a medium with scratch testing is to prescribe the scratch depth linearly increasing with the scratch length (Akono and Ulm, 2012). Fig. 4.10 shows the results of the numerical scratch test adopting an increasing scratch depth. Horizontal force increases but with oscillations due to local heterogeneity (Fig. 4.10a). The calculated scratch toughness is almost the same as the scratch toughness obtained from the previous scratch test performed with a constant normal force, which again shows that the calculated $F_T/(f)^{1/2}$ can represent the scratch toughness when the scratch reaches the fracture-driven regime. We discard data from shallow scratch depth ($d/R < 0.4$) to avoid possible misinterpretations due to inadequate scratch.

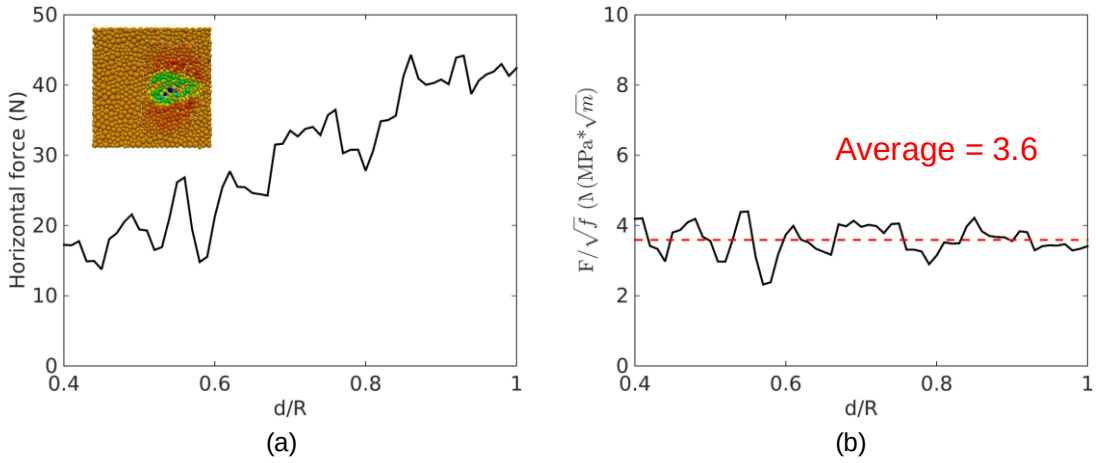

Figure 4.10: Scratch with linearly increasing depth. (a) Horizontal force statistically increases with the scratch depth (radius of stylus R = 200 μm). Oscillations come from the local heterogeneity. (b) Calculated scratch toughness = 3.6 MPa·m$^{1/2}$, similar to the result obtained from scratch test with constant normal force (3.3 MPa·m$^{1/2}$).

4.4.3 Effect of cement size reduction on fracture propagation

The potential reduction of cement size induced by the CO_2 alteration has a significant impact on rock mechanical properties. Numerical experiments with digital DEM samples show reductions of fracture toughness and brittleness. In this section we set up a DEM-BPM model of a cemented granular medium subjected to tension with evolving cement size. This simulation investigates the effect of decreasing cement size resulting from injection of a reactive fluid.

Fig. 4.11a shows a notched digital sample (1.5 mm × 1.5 mm × 0.5 mm cuboid containing 2,400 particles and 5,584 bonds). The length and height of the notch are 0.75 mm and 0.1 mm. Particles have a uniform size distribution from 50 to 100 μm. Microscopic parameters are the same as Table 4.1. We apply loads on the top and bottom of the sample, inducing tensile stresses at the notch. Initially, the sample has cement size parameter λ = 0.8 and a few bonds break but the fracture does not propagate. Resulting mode-I stress

intensity is K_I = 1.7 MPa·m$^{1/2}$ (Bower, 2009), which is smaller than the toughness obtained from scratch tests (K_c = 3.0 MPa·m$^{1/2}$ - differences partially due to a combination of mode-I and mode-II failure in scratches). Then, we reduce the parameter λ of the entire specimen with time, in order to mimic the cement dissolution due to exposure to CO_2-acidified water. The fracture propagates through the entire digital sample when λ decreases to 0.5. The fracture emerges as the coalescence of broken bonds in the DEM-BPM simulation (Fig. 4.11c).

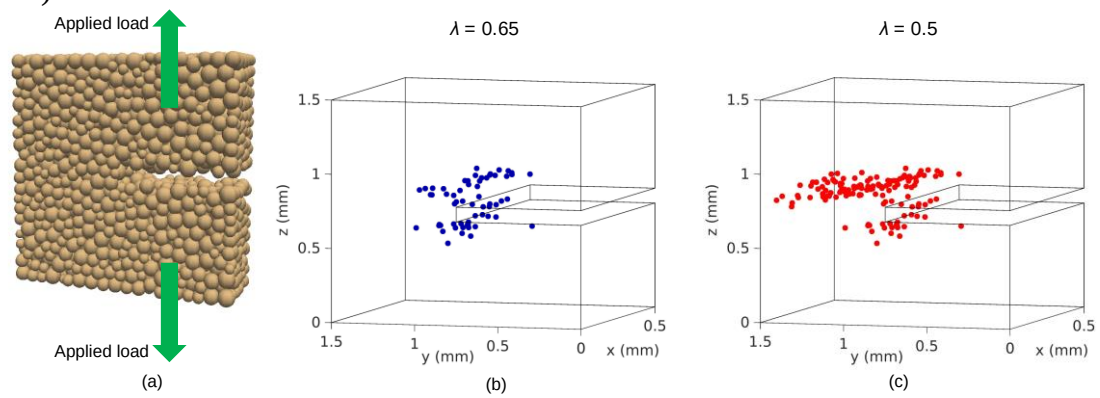

Figure 4.11: Simulation of propagation of a mode-I fracture. (a) A notched digital sample with λ = 0.8. (b) Cement size reduces to λ = 0.65 and fracture initiates from the notch. (c) Fracture propagates and finally fails the entire sample at λ = 0.5. Fracture is represented by coalescence of broken bonds or "microcracks", which are represented by points in (b) and (c).

The result demonstrates the effect of cement size reduction on triggering fracture propagation. If the sample is unaltered and contains load-bearing cements, it could be strong enough to withstand stresses in situ. However, if the CO_2-water mixture attacks the cement over a long term, alteration will reduce fracture toughness and promote fracture propagation.

4.5 CONCLUSIONS

We present a numerical model coupling the Discrete Element Method (DEM) and Bonded-Particle Model (BPM) to study the mechanical behavior of cemented geomaterials. The random bonded-particle packings are capable of numerically reproducing the mechanical properties of Entrada sandstone. Numerical simulation of micro-scratch tests provides an effective tool to investigate the impact of CO_2-related alteration at the particle scale. We successfully calibrated the simulation parameters through numerical triaxial test modeling. The rock mechanical alteration is addressed on the alterable cements rather than the siliceous rigid grains. The sensitivity analyses show that cement size is the most appropriate parameter representing the CO_2 alteration compared with other cement bond properties including elastic modulus, normal and shear strength. Scratch toughness decreases as the cement size is reduced.

We observed a resulting brittle to ductile transition when decreasing the cement size and quantified the transition by the brittleness based on bond breakage rate and released brittle energy. DEM simulations provide a unique way to quantify the sample brittleness via the rate of bond breakage, which yields a similar trend compared with the brittleness based on brittle energy. The brittleness based on DEM simulations is presented here for the first time. The defined brittleness index can distinguish the ductile/brittle fracture modes based on their physical behaviors at the particle scale. The fracture propagation associated with the cement size reduction over time is visualized through numerical modeling of a fracture toughness test. In conclusions, our simulation results show that:

- The bonded-particle model can model scratch tests with a constant vertical load on cemented sandstones.

- Scratch toughness decreases as the cement size is reduced, which is associated with the brittle to ductile transition.
- A small amount of cement dissolution (e.g. 10% in volume) can lead to a large change in scratch toughness.
- A simple approach to quantify the brittleness is proposed based on the coefficient of variation of bond breakage rate in DEM simulations.
- True scratch toughness can only be obtained when the normal force is larger than the threshold, below which the sample exhibits abnormal scratch toughness and brittleness due to the surface roughness.

Chapter 5: Reservoir Rock Chemo-Mechanical Alteration Quantified by Triaxial Tests and Implications to Fracture Reactivation[3]

5.1 INTRODUCTION

Triaxial tests provide a tool to evaluate the rock mechanical properties, such as stiffness parameters and shear strength. Brittleness is another mechanical property that characterizes the rock failure process, induced seismicity, and therefore the structural integrity of host formations. Various types of rock brittleness indices have been reviewed in the literature (Hucka and Das, 1974; Andreev, 1995; Yang et al., 2013; He et al., 2016). Meng et al. (2015) proposed a brittleness index based on post-peak stress-strain curves, which can be readily obtained from triaxial tests. The brittleness index verified by uniaxial and triaxial tests on different types of rock can reflect the influence of confining stress on rock brittleness (Meng et al., 2015). At similar levels of confining stress, a transition of brittle to ductile failure mode may appear with successive acid treatments (Zinsmeister et al., 2013). Numerical modeling on micro-scratch tests presented in chapter 4 shows that the dissolution of interparticle contact cement results in a reduction of brittleness.

This chapter presents a model based on the DEM to investigate the mechanical behavior of cemented sandstones susceptible to interparticle contact cement and particle dissolution (Fig. 5.1). We explore the role of mineral dissolution of cements and particles on mechanical properties of CO_2-altered rocks through comparison of simulated and experimental data from triaxial tests. We discuss how the mineral dissolution affects change of local stresses in the reservoir and in adjacent strata that may lead to fracture reactivation.

---

[3] Zhuang Sun, D. Nicolas Espinoza, Matthew T. Balhoff (2018). Reservoir Rock Chemo-Mechanical Alteration Quantified by Triaxial Tests and Implications to Fracture Reactivation. International Journal of Rock Mechanics and Mining Sciences.106, 250-258.
I performed the research and wrote the manuscript with support from M.T. Balhoff and D.N. Espinoza.

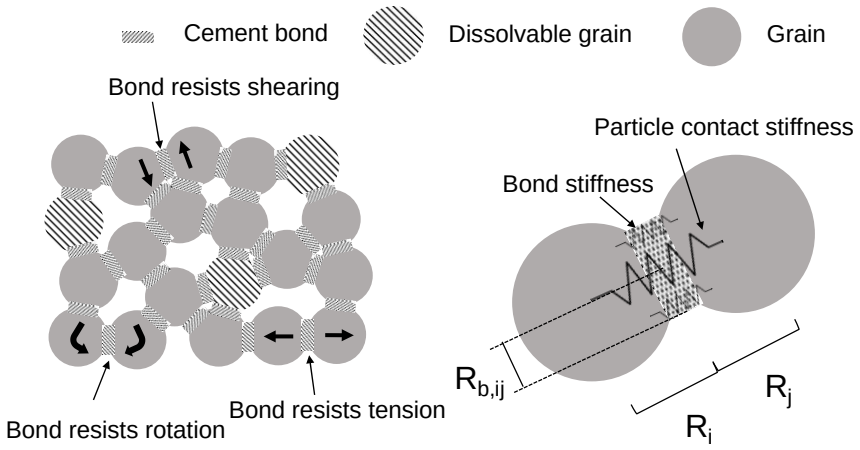

Figure 5.1: Schematic of DEM-BPM model containing two types of dissolvable minerals: bonds and full particles. Bonds resist the particle movements and act in parallel with the particle contacts. Local bond size $R_{b,ij}$ is dependent on the sizes of the bonded particle pair R_i and R_j through parameter λ.

5.2 BRITTLENESS INDEX

Brittleness characterizes rock failure and creation of new failure surfaces. An increase of mean effective stress, temperature and loading duration can result in failure transition from brittle to ductile (Mogi, 1966, 1971; Byerlee, 1968; Gowd and Rummel, 1980). Meng et al. (2015) proposed a brittleness index BI_p based on post-peak triaxial stress-strain curves:

$$BI_p = BI_{p1}BI_{p2} = \frac{\tau_p - \tau_r}{\tau_p}\frac{\log_{10}\left|\frac{k_{ac}}{MPa}\right|}{10} \tag{5.1}$$

where BI_{p1} is the magnitude of the relative post-peak stress drop and BI_{p2} represents the velocity of stress decrease. Parameters τ_p and τ_r are the peak and residual stresses, respectively. Parameter k_{ac} is the slope of the line that joins the peak strength point to the starting point of the residual strength. Both BI_{p1} and BI_{p2} range from 0 to 1. The form of BI_{p2} is to normalize the value of k_{ac} within the range of 0-1. A larger value of BI_{p1} and BI_{p2}

results in a larger BI_p, indicating a higher brittleness. The index BI_p is suitable to evaluate rock brittleness with uniaxial and triaxial tests on various types of rock (Meng et al., 2015).

5.3 RESULTS

5.3.1 Experimental triaxial data

Espinoza et al. (2018) performed triaxial tests on Entrada Sandstone air-dry samples at confining stress $\sigma_3 = 0.69$ MPa (100 psi), 6.9 MPa (1000 psi) and 20.7 MPa (3000 psi). Samples are 25 mm in diameter and 54 mm in height. CO_2-altered and unaltered Entrada Sandstones were taken from outcrops in the Crystal Geyser field that has been used as a CO_2 sequestration analog. CO_2-altered samples are subject to hematite dissolution, which leads to the bleaching of otherwise red unaltered samples. Thin section and micro-tomography analyses showed higher porosity and less cementation in altered sandstone than unaltered sandstone. Entrada Sandstone has a grain size distribution mostly in the range of 50 to 100 μm.

5.3.2 Baseline unaltered Entrada Sandstone model and calibration

The DEM numerical sample is initialized as a random particle packing with a uniform diameter distribution from 50 to 100 μm. The cylindrical DEM numerical sample has a height of 2.54 mm and a diameter of 1.27 mm, containing 7,928 particles and 23,178 bonds. The numerical sample is shown to be large enough to reduce the sample inhomogeneity and boundary effect. More details on the DEM sample size effect can be found in relevant literatures (Potyondy and Cundall, 2004; Kuhn and Bagi, 2009; Huang et al., 2014). The porosity is 39%, not including cement bond volume. Similar to the experimental conditions, we apply different constant confining stresses, $\sigma_3 = 0.69$ MPa,

6.9 MPa and 20.7 MPa in the radial direction. We apply the constant confining stress through 10×12 segmented servo walls in the radial direction.

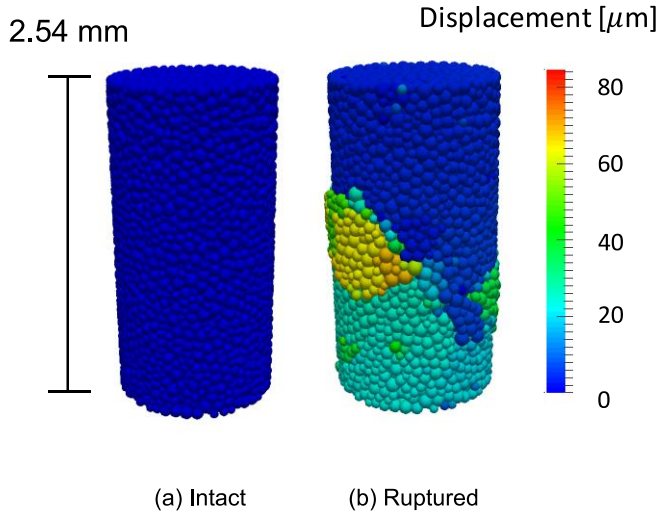

Figure 5.2: Snapshots of triaxial test modeling. The initially intact DEM numerical sample ruptures with a shear band due to the deviatoric loading $\sigma_1-\sigma_3$. Confining stress σ_3 is 0.69 MPa. Color represents vertical displacement of particles.

The calibration is performed against experimental triaxial tests on unaltered Entrada Sandstone under a confining pressure of 0.69 MPa. Parameter λ is fixed as 0.8 to keep the microscopic parameters in a range of practical values. Thus, the model calibration (Fig. 5.3a) results in a set of parameters E, k_T/k_N, σ_c and τ_c (Table 5.1). We perform sensitivity analyses of these microscopic parameters in section 5.3.3. Fig. 5.3b and 5.3c show the blind predictions of stress-strain for the numerical triaxial test results at confining stress of 6.9 MPa and 20.7 MPa using the previously calibrated microscopic parameters, in comparison with experimental results for unaltered Entrada.

Table 5.1: Microscopic parameters for numerical triaxial test

Particle-particle contacts	Bonds
E = 4 GPa	E_b = 4 GPa
k_T/k_N = 1	$\bar{k}_T/\bar{k}_N$ = 1
μ = 0.5	λ = 0.8
ρ = 2650 kg/m^3	σ_c = 20 MPa
	τ_c = 80 MPa

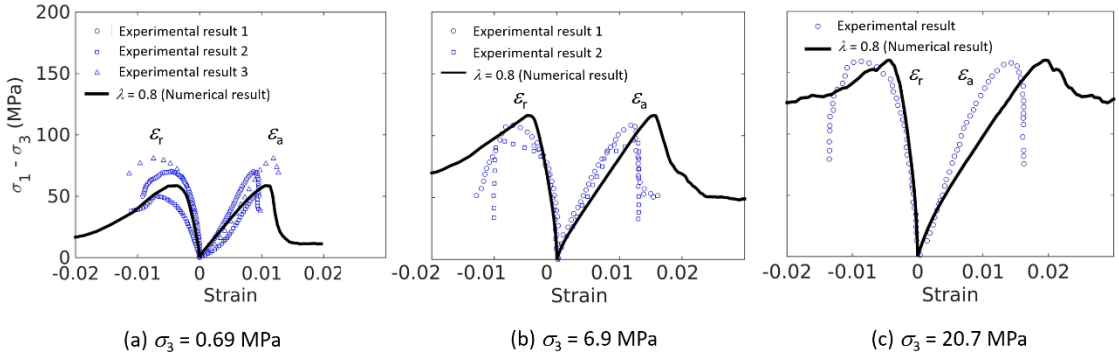

Figure 5.3: Axial/radial strain, $\varepsilon_a/\varepsilon_r$, as a function of deviatoric stress $\sigma_1-\sigma_3$ from numerical and experimental triaxial tests under various confining stresses σ_3.

Fig. 5.3 shows that the numerical triaxial tests yield similar results as the experimental triaxial tests performed on unaltered Entrada Sandstone with respect to elastic modulus, strength and Poisson's ratio. We further summarize the experimental and numerical tangent values of these mechanical properties measured at 40% of peak stress in Table 5.2. As expected, increases in confining stress result in stronger samples. The peak strength is followed by a rapid strain softening in all experimental results, which indicates that the unaltered Entrada Sandstone remains brittle with an increasing confining stress up to 20.7 MPa. This is likely because the maximum confining stress is relatively low

compared to the rock strength (maximum σ_3 = 20.7 MPa compared to rock unconfined compression strength ~ 66 MPa) and the stress needed for significant grain crushing. On the contrary, the DEM numerical sample becomes more ductile when the confining stress increases. The discrepancy may result from having spherical grains and high initial porosity. Another source of discrepancy between the model results and the experimental data is grain crushing, which our DEM-BPM model does not capture. However, bulk strain measurements indicate dilation at failure in all cases and microscopic observations provide evidence for negligible grain crushing in the shear band (experiments stopped shortly after peak stress).

The following sections explore the role of dissolution of cementing bonds and dissolvable particles on mechanical properties of Entrada Sandstone and compare them with experimental results on geologically altered rock samples.

Table 5.2: Comparison of mechanical properties obtained from experiments and numerical simulations

Confining stress (MPa)	0.69		6.9		20.7	
	Exp.	Num.	Exp.	Num.	Exp.	Num.
Young's modulus (GPa)	5.5	6.5	12.4	8.9	14.4	11.0
Peak strength (MPa)	60	59	115	123	179	181
Poisson's ratio	0.16	0.20	0.19	0.17	0.20	0.12

5.3.3 Effect of dissolution of cementing bonds

Experimental triaxial tests were also performed on CO_2-altered Entrada Sandstone. CO_2-altered sandstone samples are statistically weaker than the unaltered samples. The macroscopic rock mechanical behavior is significantly affected by the cement bond micromechanical properties, which include cement bond size, elastic modulus, normal strength and shear strength. Fig. 5.4 shows the sensitivity analyses for these bond

microscopic properties. The investigated parameter is varied while all other parameters are the same as in Table 5.1. The confining stress is 0.69 MPa.

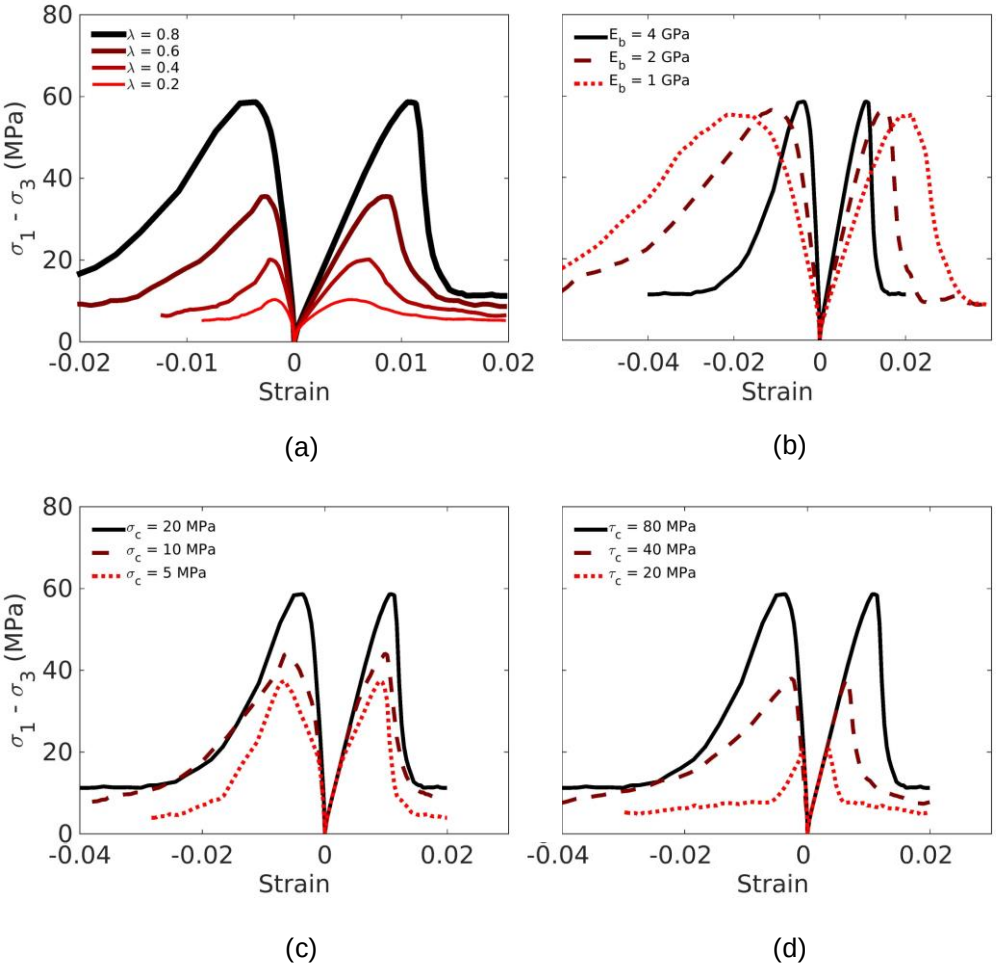

Figure 5.4: Sensitivity analyses for cement bond (a) size, (b) elastic modulus, (c) normal strength and (d) shear strength. σ_3 = 0.69 MPa.

Fig. 5.4a shows that cement bond size, λ, has a significant impact on the mechanical behavior with a clear strength reduction and brittle to ductile transition as λ decreases. Fig. 5.4b shows that the bond elastic modulus has little impact on shear strength. Larger bond elastic modulus results in stiffer but easier-to-break bonds, which in combination yields the similar peak strength for various elastic moduli. As expected, the macroscopic elastic

modulus of the sample decreases as the microscopic bond elastic modulus decreases. Fig. 5.4c and 5.4d show that the normal and shear bond strengths have a significant impact on the sample strength but little impact on the macroscopic elastic modulus before bond breakage. The sample strength appears to be more sensitive to the bond shear strength than to the normal strength, which indicates that the bond breakage predominantly occurs in the shear mode.

Table 5.3 summarizes the brittleness indices of DEM numerical samples with various microscopic properties (Eq. 5.1). The results show that the bond elastic modulus, the normal and shear bond strength have a limited impact on the sample brittleness. However, the cement bond size strongly affects the sample brittleness. Smaller cement bond size and parameter λ results in a more ductile sample at various confining stresses. Smaller bond shear strength, that only affects the bond breakage onset, has slight influence on brittleness.

Table 5.3: Brittleness for DEM numerical samples with various bond microscopic parameters

λ	BI_p	E_b (GPa)	BI_p	σ_c (MPa)	BI_p	τ_c (MPa)	BI_p
0.2	0.12	1	0.29	5	0.29	20	0.24
0.4	0.21	2	0.31	10	0.32	40	0.27
0.8	0.32	4	0.32	20	0.32	80	0.32

Let us use the cement bond size parameter λ (all other DEM-BPM model parameters are identical as shown in Table 5.1 for unaltered Entrada) to mimic the mechanical degradation measured experimentally in Entrada Sandstone. Fig. 5.5 compares the experimental results of altered Entrada Sandstone with DEM numerical predictions with best-fitting parameter λ reproducing the reduced rock strength in all altered samples.

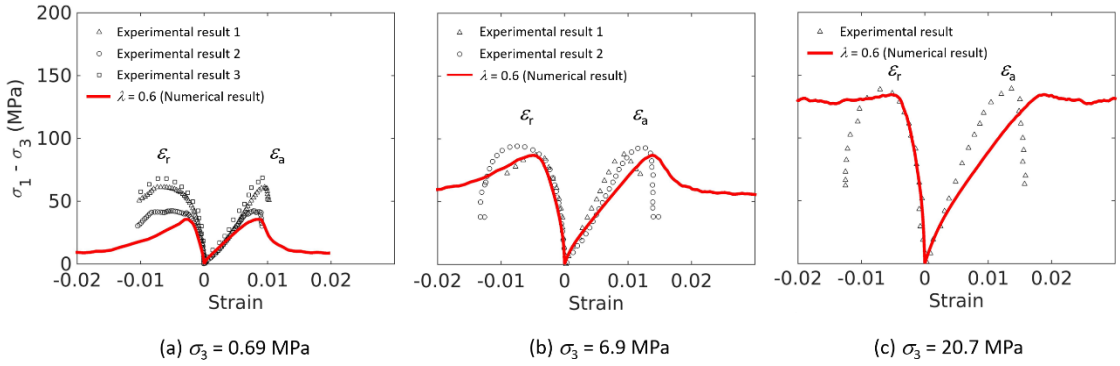

Figure 5.5: Experimental and numerical results (varying bond size parameter λ) of CO_2 geologically altered Entrada Sandstone. DEM-BPM suggests a reduction of λ from 0.8 to 0.6 to match rock alteration.

The discrepancy between numerical and experimental results at σ_3 = 6.9 and 20.7 MPa indicates an alternative mechanism other than cement dissolution, such as bond strength reduction or full particle dissolution. This is discussed in detail in section 5.3.4. In summary, the cement bond size, λ, is the most sensitive bond microscopic property that significantly affects the shear strength in a similar way that is observed in the experiments.

5.3.4 Effect of full grains dissolution

In addition to intergranular cements, grains and pore-filling solids composed of easily dissolvable minerals (such as carbonates) may also be removed by dissolution into CO_2-water mixtures. The dissolution of grains and pore-filling solids can alter the mechanical properties in a similar manner as the dissolution of intergranular cements, both of which result in changes in rock skeleton and fabric. The dissolvable grains and pore-filling minerals are idealized as removable particles in this section. Cement bond properties remain identical as given in Table 5.1. We randomly remove particles to mimic the dissolution of grains and pore-filling minerals. To investigate quantitatively the effect of full grain dissolution on the sample brittleness, we randomly remove 5%, 10% and 15%

particles. Fig. 5.6 shows the numerical triaxial test results for various particle removal percentages, V_{diss}.

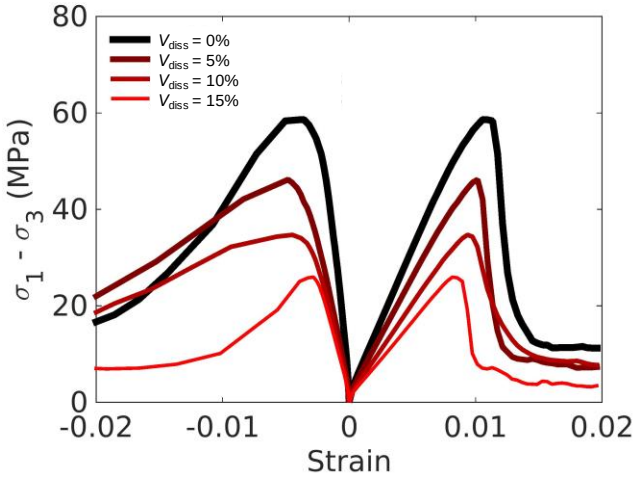

Figure 5.6: Numerical triaxial test results for random particle removal. The confining stress is 0.69 MPa.

Fig. 5.6 shows that the dissolution of grains and pore-filling minerals leads to similar mechanical degradation as the dissolution of intergranular cements. Hence the dissolution of full reactive grains may also explain experimentally measured CO_2-induced mechanical alteration in Entrada Sandstone.

We further investigate the effect of grain dissolution on DEM numerical sample brittleness. Table 5.4 summarizes the quantitative brittleness results under various confining stresses 0.69 MPa, 6.9 MPa and 20.7 MPa.

Table 5.4: Brittleness for DEM numerical samples after the random particle removal

0.69 MPa		6.9 MPa		20.7 MPa	
% of removal	BI_p	% of removal	BI_p	% of removal	BI_p
0	0.32	0	0.22	0	0.08
5	0.31	5	0.17	5	0.03
10	0.27	10	0.18	10	0.02
15	0.30	15	0.17	15	0.03

Table 5.4 shows that the random particle removal only has small impact on the calculated BI_p, especially compared with the effect of cement bond size. Fig. 5.7 includes the comparison between experimental triaxial test results and numerical results using V_{diss} as a fitting variable. Particles are randomly removed to mimic the effect of full grain dissolution. DEM-BPM model suggest a dissolution of 5% of particles to match experimental results of altered respect to unaltered Entrada Sandstone. Cement bond microscopic properties are the same as in Table 5.1. The digital sample cannot capture the post-peak behavior likely due to the assumptions in spherical particles.

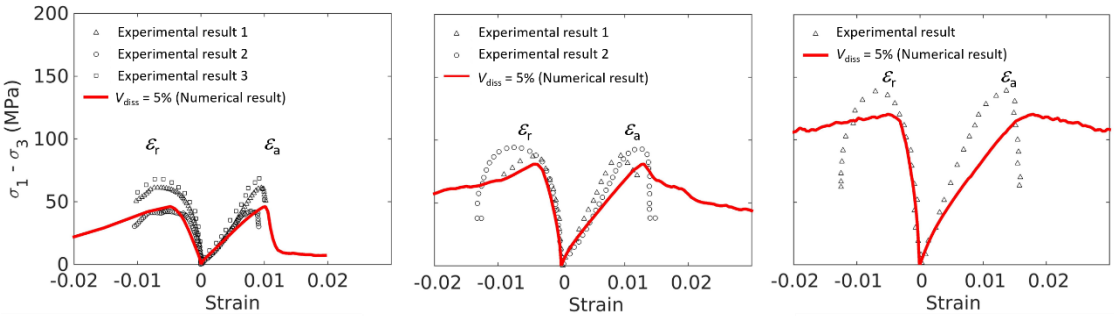

Figure 5.7: Comparison of experimental and numerical results for CO_2-altered Entrada Sandstones.

5.4 DISCUSSION

5.4.1 The effect of mineral dissolution in reservoir rock under subsurface storage conditions

Previous work suggests that the dissolution of hematite and calcite minerals are main factors contributing to the weakening of Entrada Sandstone altered in the near-surface (Major et al., 2014; Aman et al., 2017a; Espinoza et al., 2018). Experimental triaxial test results show evidence of degradation of rock stiffness and strength. However, such alterations are dependent on the stress state and stress path. For instance, cavities observed

in shallow karst terrain due to carbonate dissolution become less possible as the overburden stress increases with burial depth (White et al., 1995). Similarly, the CO_2 alteration path under high levels of mean effective stress and deviatoric stress is not necessarily the same as the one at near-surface conditions. Dissolution of cement and mineral grains may result in grain crushing, pore collapse, grain rearrangement and loss of porosity under high *in situ* stress, which at the larger scale manifests as reservoir compaction and stress redistribution (Segall and Fitzgerald, 1998; Goulty, 2003; Shin et al., 2008; Kim and Santamarina, 2014).

Reservoir rocks in CO_2 storage formations experience higher overburden stress than outcrops. We propose a DEM-BPM model to investigate the chemo-mechanical alteration path, which mimics the mineral dissolution under a stressed condition. Fig. 5.8 shows the schematic of the numerical model. The DEM numerical sample is a 1.5 mm × 1.5 mm × 1.5 mm cube with 8,332 particles and 24,410 bonds. The random particle packing has a uniform diameter distribution from 50 to 100 μm. DEM-BPM model parameters are the same as Table 5.1. We apply a constant vertical effective stress σ_{zz} = 30 MPa, 50 MPa and 70 MPa. There is no pore pressure in DEM simulations. Fixed lateral walls constrain the horizontal displacement. The initial stress state is set isotropic, i.e. $\sigma_{xx} = \sigma_{yy} = \sigma_{zz}$. We decrease the cement bond size or increase the dissolvable grain percentage V_{diss} to mimic the mineral dissolution at bonds and particles due to the exposure to CO_2-rich brine.

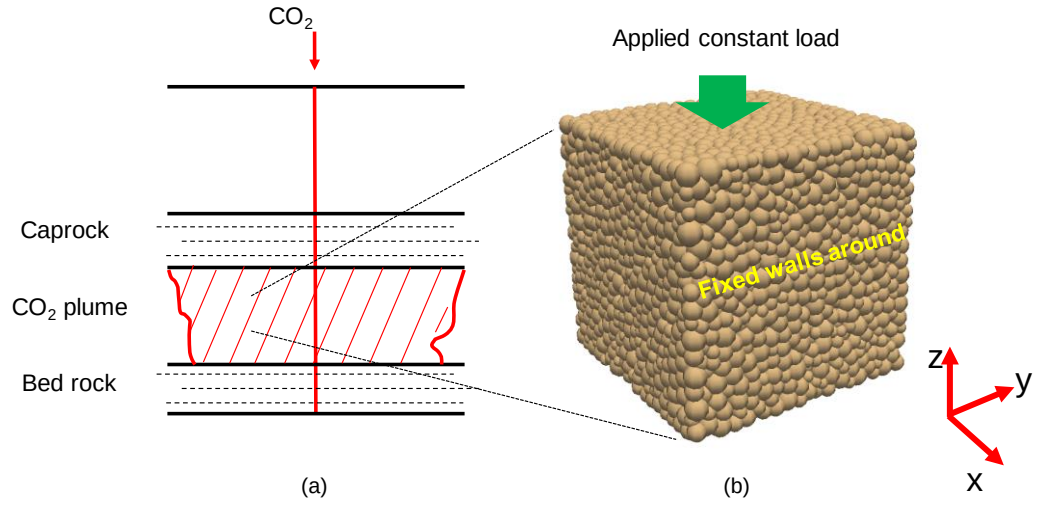

Figure 5.8: (a) Schematic of CO_2 storage. The DEM numerical sample taken from the host formation is in contact with the CO_2 plume. (b) DEM-BPM model schematic.

Fig. 5.9 shows the simulation results. The mineral grain dissolution results in a more significant rock compaction (increase in vertical strain ε_{zz}) compared with the cement dissolution, which is likely due to the alteration in rock skeleton and fabric. Mineral dissolution also results in horizontal stress relaxation (decrease in horizontal stress σ_{xx}). The compaction and stress relaxation become more significant as the effective stress increases. Previous work investigating the dissolution of full particles in uncemented granular media results in similar conclusions (Shin et al., 2008; Cha and Santamarina, 2014). Our simulation results indicate that CO_2 alteration caused by mineral dissolution may have different impacts on subsurface reservoir rocks and outcrops due to the change in local stress conditions. CO_2 injection field projects have shown unexpected microseismic events in the Mt. Simon reservoir sandstone, indicating subsurface stress change (Bauer et al., 2016). Significant strains induced by chemo-mechanical processes related to CO_2 injection have not been observed in the field yet.

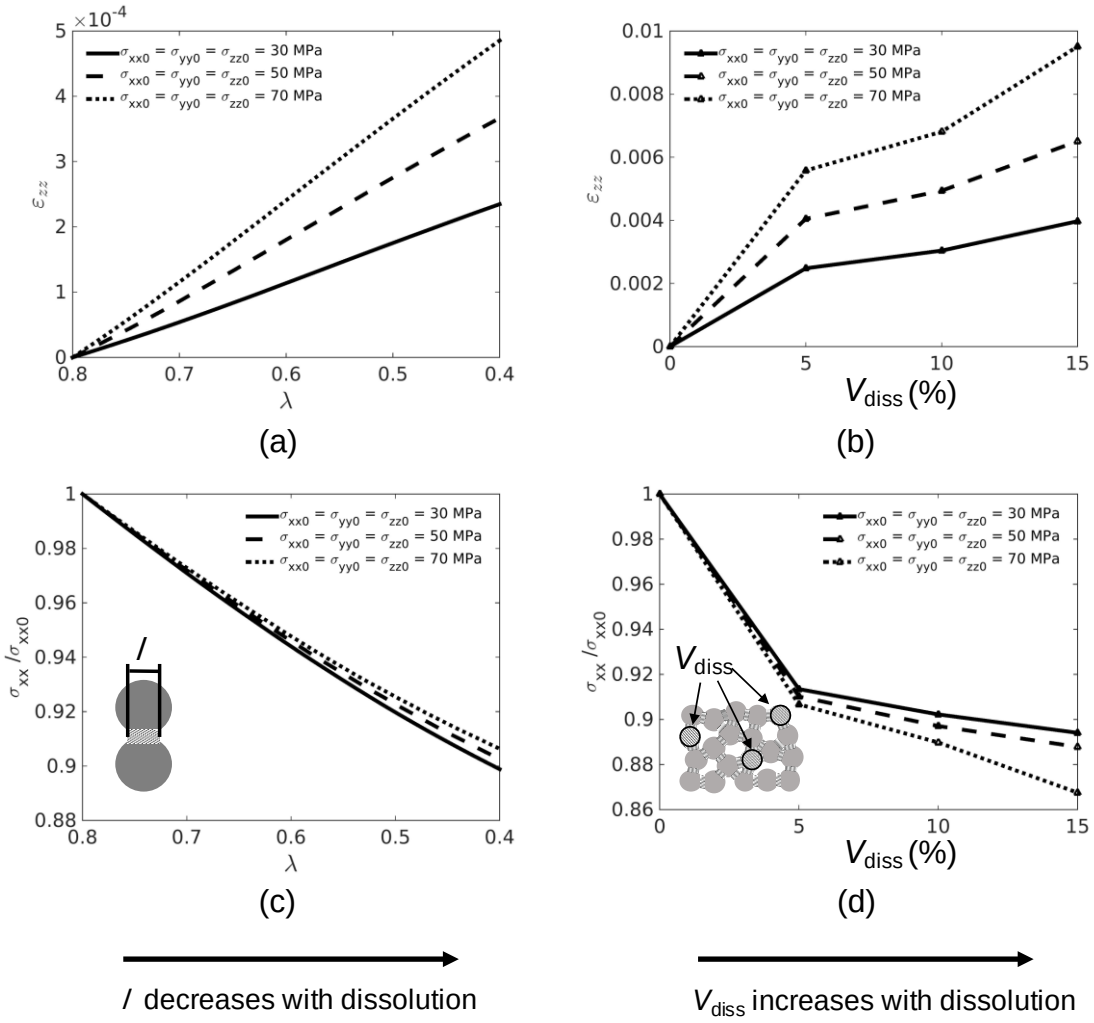

Figure 5.9: Change in vertical strain ε_{zz} (compaction) and horizontal stress σ_{xx} (relaxation) due to the dissolution at cement bonds λ and mineral particles V_{diss}. σ_{xx0} is the initial horizontal stress in direction x.

5.4.2 Dissolution-induced stress transfer from reservoir to bounding layers: impact on fracture reactivation

The DEM-BPM model has been used to simulate seismic events in brittle rock (Hazzard and Young, 2004). We investigate the CO_2-induced microseismicity, which assumes that fracture reactivation corresponds to a cluster of broken bonds. Fig. 10a-b shows the model schematic. The DEM numerical sample is a 9 mm × 9 mm × 0.3 mm

cuboid with two predominate directions. The sample contains 56,159 particles and 141,772 bonds. The particles have a uniform diameter distribution from 50 to 100 μm. Microscopic parameters are the same as shown in Table 5.1. The model contains three layers representing the caprock, host formation and bedrock, which correspond to shale, sandstone and crystalline basement with increasing bond elastic moduli. We apply constant far-field effective stresses σ_{Hmax}^{eff} = 60 MPa, σ_{hmin}^{eff} = 30 MPa and σ_{v}^{eff} = 30 MPa based on field data from the Decatur project (Bauer et al., 2016). The red block shown in Fig. 5.10c represents the reservoir volume affected by the CO_2 plume, where the cement bond size is reduced (λ changes from 0.8 to 0.4) indicating the cement dissolution due to contact with CO_2-acidified water. Cements are not altered in the domain outside the red box (λ = 0.8) mimicking the intact surrounding area.

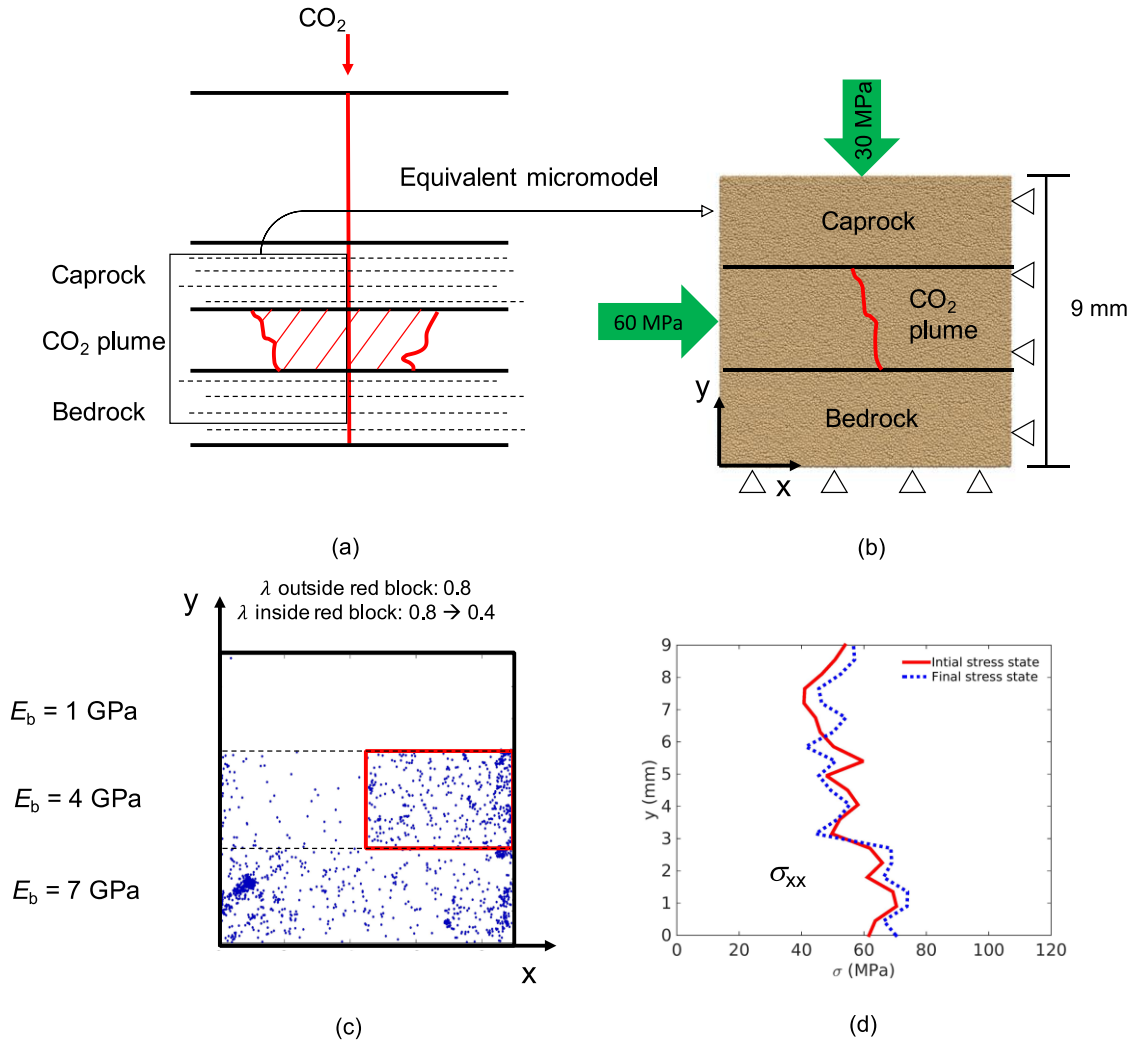

Figure 5.10: (a) Schematic of CO_2 storage. (b) Equivalent micromodel of caprock, reservoir and bedrock area. (c) Distribution of broken bonds when $\lambda = 0.4$. Size of cement in the red block is reduced from 0.8 to 0.4, which mimics the CO_2-induced cement dissolution. (d) Horizontal effective stress σ_{xx} measured on the right side of the model. Horizontal stress transfers to caprock and bedrock.

Fig. 5.10c-d show the simulation result. Points in Fig. 5.10c represent broken bonds, i.e. microcracks. Most of the broken bonds appear in the bottom layer, indicating a preferential zone for bond breakage in the bedrock, i.e. similar to fracture reactivation. The storage site weakened by CO_2 becomes less capable to withstand the constant horizontal

stress as shown in Fig. 5.10d. Therefore, stress tends to redistribute to the intact surrounding area, resulting in bond breakage in the bedrock. Although the mineral dissolution may lead to undesired stress change, the ensuing brittle/ductile transition and mineral precipitation could mitigate the strain localization in reservoir rock. These results highlight the possibility of potential induced seismicity in stiff basement rock where the reservoir rock is weakened.

5.5 CONCLUSIONS

We quantitatively investigate the CO_2-induced alteration through the DEM-BPM modeling of triaxial tests. Reactive minerals exist as intergranular bonds and dissolvable particles in the DEM-BPM model. Sensitivity analyses for the bond microscopic properties indicate that cement bond size impacts the CO_2-induced mechanical alteration and controls brittleness of DEM numerical sample. The dissolution of full grains can also describe the rock mechanical degradation whereas it has limited influence on the brittleness. The change of brittleness index indicates a transition from brittle to ductile due to a decrease of cement bond size.

A CO_2 storage site under subsurface boundary conditions exhibits a different alteration path from that of the outcrops based on a DEM-BPM simulation. The alteration-induced stress change could also result in stress transfer outside the CO_2 storage formation, which may further trigger the fracture reactivation and induced seismicity. The DEM-BPM model provides a unique tool to investigate the CO_2 alteration and subsequent changes in strain and stress. To conclude, this study shows that:

- Cement bond size reduction and full particle dissolution are two likely mechanisms of CO_2-induced alteration on Entrada Sandstone.

- Cement size is the most likely bond microscopic parameter controlling the DEM numerical sample brittleness. On the contrary, full grain dissolution has small impact on the brittleness.
- CO_2-induced cement dissolution in deep storage sites can result in rock compaction and horizontal stress relaxation.
- CO_2 alteration can induce microseismic events outside the injection zone, which may explain the occurrence of fracture reactivation observed in the field.

Chapter 6: Pore-Scale Modeling of Grain Crushing[4]

6.1 INTRODUCTION

In this chapter, we present numerical simulations that complement laboratory experiments and provide a means to quantify the impact of sand grain micromechanical properties. We introduce a grain crushing model based on the Discrete Element Method (DEM) and the Bonded-Particle Model (BPM). In another study, we represented a crushable grain with a large sphere surrounded by identical small spheres, which is shown to be computationally efficient (Appendix A). However, the regular mono-sized spheres geometry used in this study can capture the change in particle size distribution and fines production, and therefore result in a better estimation of change in permeability with crushing (Sun et al., 2018d). We perform single-grain-crushing tests and calibrate the model parameters by comparing the crushing strength with experimental results. Then, we perform numerical uniaxial strain tests on a packing of crushable grains and calculate the induced changes of porosity and permeability with an increasing effective stress. We focus on the investigation of two factors: the grain size and the presence of soft inclusions (e.g. shale fragments). We compare the numerical result of permeability to field data from a literature.

6.2 GRAIN CRUSHING MODEL

We represent crushable grains in the DEM-BPM by particle agglomerates that allow grain breakage. The agglomerates consist of bonded individual mono-sized spheres in a regular hexagonal close packing (HCP) (Thornton et al., 1996; McDowell and

[4] Zhuang Sun, Hewei Tang, D. Nicolas Espinoza, Matthew T. Balhoff, John E. Killough. Pore- to Reservoir-Scale Simulations of Depletion-induced Compaction and Implications on Production Rate. SPE Annual Technical Conference and Exhibition. Dallas, TX, 24-26, September, 2018.
I performed the research and wrote the manuscript with support from M.T. Balhoff, D.N. Espinoza, H. Tang and J.E. Killough.

Harireche, 2002; Cheng et al., 2003; Jurgens, 2007; Alonso et al., 2012; Cil and Alshibli, 2014). The HCP structure avoids the overlapping among spheres and yields the densest packing in the spherical agglomerate (Kwok and Bolton, 2013). The elementary sphere size is equal to one fourth of the agglomerate size. The bonds fill out the void space of agglomerates. Therefore, the packing porosity will refer to the inter-agglomerate porosity in the following sections. Fig. 6.1 shows how the DEM model idealizes sands containing structural soft shale as crushable particles in this study (Thomas and Stieber, 1975). We assume spherical grain shape, mono-sized bonded spheres and structural shale grains. The DEM model in this study provides a grain-scale simulation approach whereas can never capture all features of complicated real rocks.

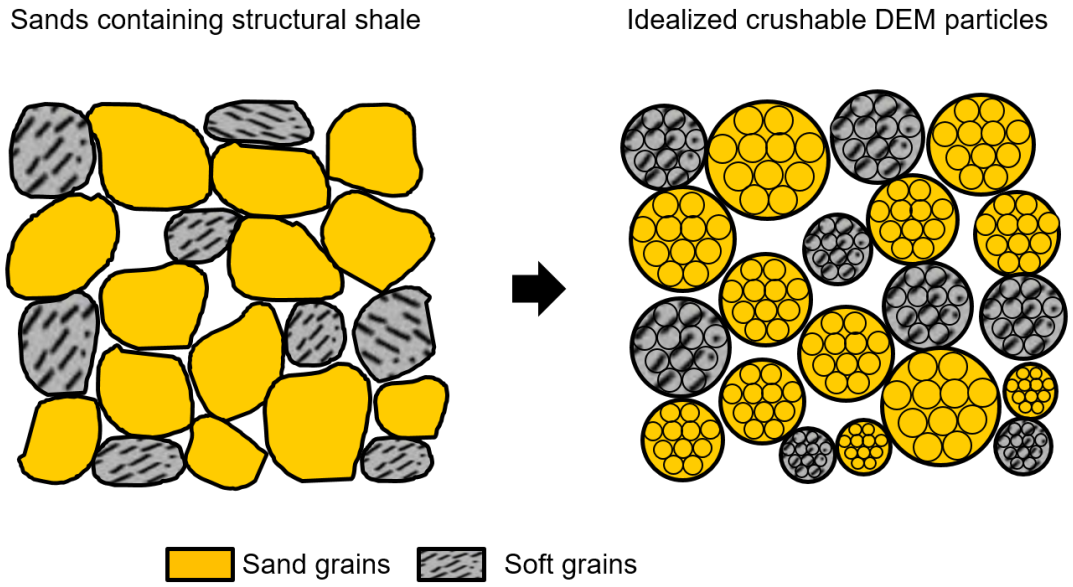

Figure 6.1: Idealization of sands containing structural shale as crushable DEM particles

We perform single-grain-crushing tests to calibrate the model parameters (Mirabolghasemi, 2017). Fig. 6.2a shows that two stiff walls constrain an agglomerate with free side boundaries. This is the same as the experimental single-grain-crushing test. The agglomerate consists of 46 spheres and 173 bonds. The top wall moves toward the

agglomerate with a constant velocity of 0.05 m/s with the bottom wall fixed. The velocity is low enough for the agglomerate to undergo a quasi-static deformation. We measure the force and displacement of the top wall during the tests. Fig. 6.2b shows the force-displacement curves for agglomerates of different diameters D_p. Table 6.1 summarizes the model parameters. Elastic modulus E = 4 GPa and stiffness ratio k_T/k_N = 1 are typical values for sand particles. Parameter λ is fixed as 0.5 to keep the microscopic particle and bond properties within reasonable ranges. Bond normal strength σ_c and shear strength τ_c are calibrated against experimental single-grain-crushing tests on sand grains (Nakata et al., 1999).

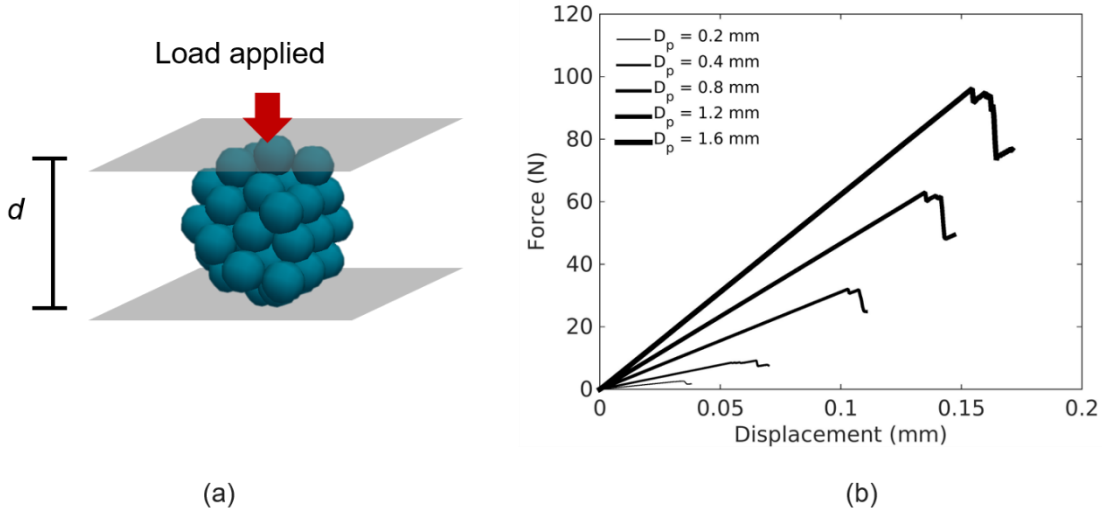

Figure 6.2: (a) Schematic of single grain crushing test. We use the top and bottom stiff walls to crush the agglomerate. (b) Force and displacement are measured for agglomerates of various diameters.

Table 6.1: Microscopic DEM-BPM parameters for agglomerates of various diameters

Parameters	Values
E	4 GPa
k_T/k_N	1
λ	0.5
σ_c	100 MPa
τ_c	120-190 MPa

Fig. 6.2b shows that large agglomerates tend to have a high peak force that coincides with agglomerate crushing. The crushing strength σ_g [Pa] is defined as (Jaeger, 1967):

$$\sigma_g = \frac{F}{d^2} \tag{6.1}$$

where F represents the peak force and d is the agglomerate diameter between the two walls. Agglomerates of different sizes have identical crushing strength when using the same model parameters. Kwok and Bolton (2013) developed a DEM model using the decay of bond strength to simulate the change of grain strength under sustained loading. In order to mimic the size effect of real sands, we assume that the bond shear strength τ_c is linearly correlated with the agglomerate size D_p. Large grains tend to have a small bond shear strength.

Fig. 6.3 shows the change of crushing strength as a function of particle diameter for numerical agglomerates and experiments for sand grains. The numerical results are calculated from force-displacement curves shown in Fig. 6.2b. The experimental results correspond to single-grain-crushing tests performed on quartz sands of various diameters (Nakata et al., 1999). With the calibrated model parameters in Table 6.1, the numerical agglomerates can reproduce the change of characteristic crushing strength with sand grain

size. Small sand grains tend to have a large crushing strength due to the lower likelihood of being flawed (Nakata et al., 1999). Numerical agglomerates in this study introduce the crushing strength scale effect by changing the bond shear strength instead of directly incorporating these physical flaws. In the next section, these numerical agglomerates are randomly packed to investigate the porosity and permeability of unconsolidated sands as a function of effective stress.

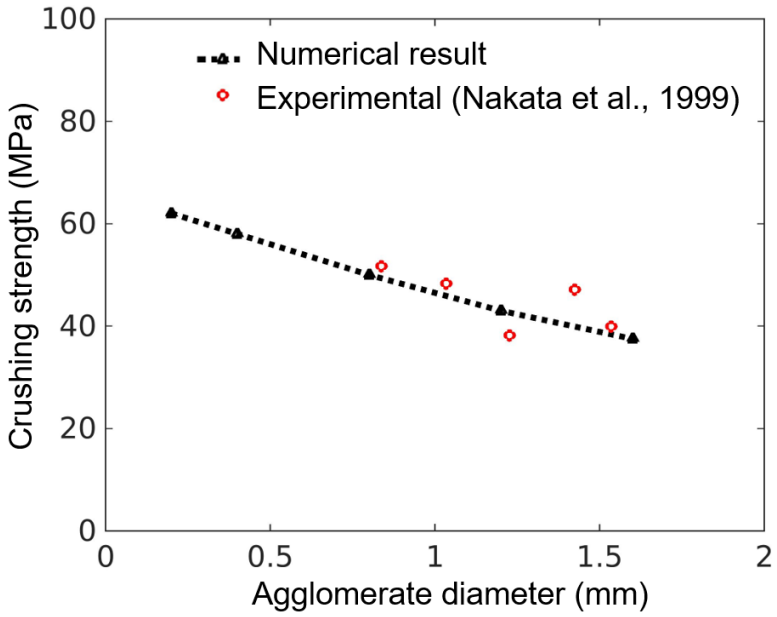

Figure 6.3: Numerical agglomerates can reproduce the change of sand grain crushing strength as a function of particle diameter. Experimental result is from Nakata et al. (1999).

6.3 Numerical Uniaxial Strain Test

6.3.1 Effect of grain (agglomerate) size

Fig. 6.4 shows the schematic of the numerical uniaxial strain test, which applies a constant vertical stress and constrains the horizontal strains with fixed walls. The numerical sample is a 1.5 mm cube containing 484 agglomerates of 200 μm diameter. The number of

agglomerates maintains constant for packing of different sizes. The initial agglomerate packing porosity is 40%.

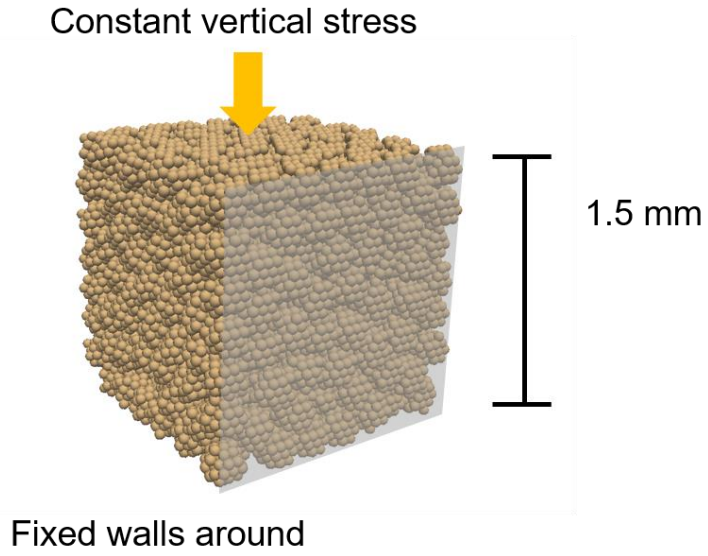

Figure 6.4: Schematic of numerical uniaxial strain test. The boundary conditions are constant stress in the vertical direction and no displacement in the horizontal directions. Agglomerate size D_p = 200 μm.

We perform uniaxial strain tests on packing with an agglomerate size of 100, 200, and 400 μm, respectively. The simulation takes ~15 hours on one Intel i7-3820 3.60GHz processor. We assume that the intra-agglomerate porosity is filled with cement bonds. Therefore, the porosity here refers to the inter-agglomerate porosity and its calculation is based on the change of vertical strain as shown in Eq. 6.2:

$$\phi = \frac{\phi_0 - \varepsilon_{zz}}{1 - \varepsilon_{zz}} \tag{6.2}$$

where ϕ and ϕ_0 are the current and initial porosity and ε_{zz} is the measured vertical strain. Fig. 6.5 shows the change of porosity as a function of the effective vertical stress. DEM simulations have zero pore pressure; therefore, the effective stress is equal to the applied vertical stress.

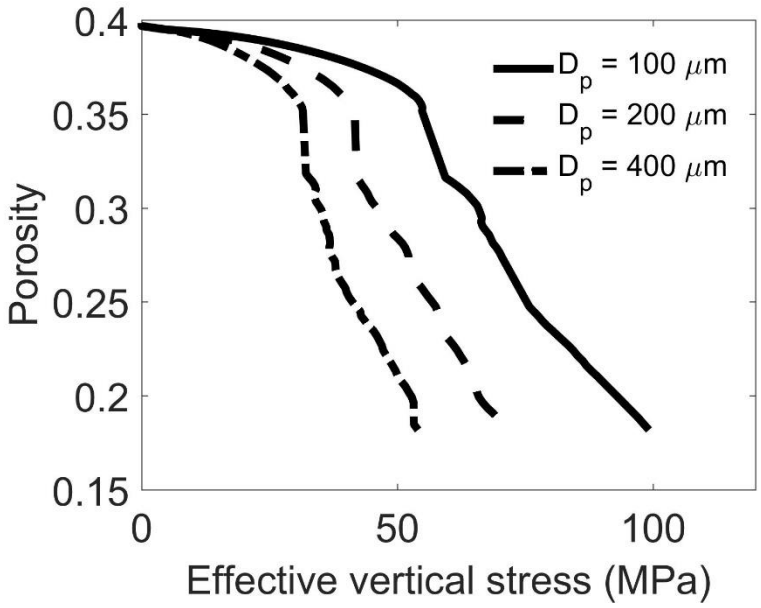

Figure 6.5: Change of porosity as a function of effective vertical stress. Uniaxial strain tests are performed on packings with an agglomerate diameter D_p = 100, 200 and 400 μm.

The porosity shows a pronounced reduction as the effective stress exceeds the corresponding threshold. Grain slippage and rotation contribute to the porosity reduction at low effective stress. Grain crushing becomes significant when the effective stress exceeds the compressive strength and induces plastic deformation. Grain size has a limited impact under a low effective stress when grain slippage and rotation is the dominant mechanism. On the contrary, grain size has a significant impact under a high effective stress when grain crushing manifests. Large grains tend to have a low threshold of effective stress because of the low grain crushing strength as shown in Fig. 6.3.

Grain crushing produces fines and results in reduction of porosity. Grain crushing manifests as the breakage of agglomerates in DEM simulations. Therefore, we capture the change of particle size distribution by counting the number of bonded elementary particles in each agglomerate. Fig. 6.6 shows the size distribution of agglomerates after successive

fragmentation generations caused by increasing the effective stress (D_p = 200 μm). The vertical axis represents the percentage of smaller agglomerates by volume (Bolton et al., 2008). We plot the data in logarithmic axes for a better visualization of the fine production. The agglomerate size is assumed proportional to the 1/3 power of the number of bonded elementary particles. The initial size distribution of agglomerates is nearly uniform. The agglomerates are more distributed in size containing a pronounced amount of fines as the effective stress increases. Note that the smallest size is limited by the size of elementary particle that constitutes the agglomerate.

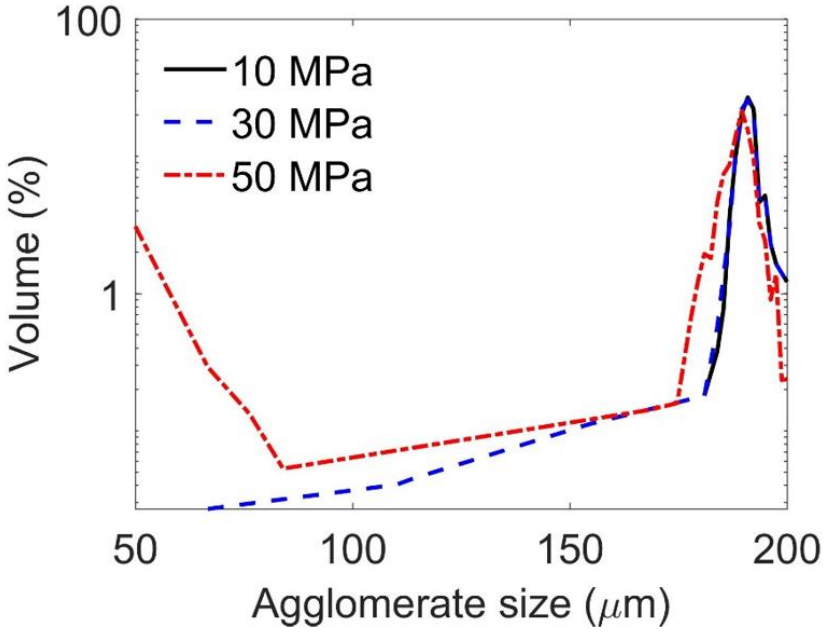

Figure 6.6: Distribution of agglomerate size as a function of effective stress (in the legend).

We capture the change of permeability with porosity using the Kozeny-Carman equation based on the results shown in Fig. 6.5 and Fig. 6.6 (Carrier, 2003):

$$k = \frac{D_a^2}{150}\frac{\phi^3}{(1-\phi)^2} \tag{6.3}$$

where k is the current permeability, ϕ is the porosity, D_a is the harmonic average of grain size as shown in Eq. 6.4. Parameter f_i is the fraction of particles of size D_i.

$$D_a = \frac{100\%}{\sum\left(\frac{f_i}{D_i}\right)} \tag{6.4}$$

The Computational Fluid Dynamics (CFD) provides another approach to compute permeability. However, it still remains challenging to numerically capture the evolution of permeability caused by grain crushing and fines production (Mirabolghasemi, 2017; Yang, 2018). Fig. 6.7 shows the change of normalized permeability k/k_0 as a function of effective stress. Parameter k_0 is the initial permeability. The permeability loss induced by the change of effective stress exhibits a similar trend to the porosity decrease (Fig. 6.5). The permeability exhibits a significant reduction as the effective stress exceeds the threshold that indicates grain crushing. Packs of large grains are more readily affected by grain crushing and tend to have a more significant permeability loss than packs of small grains. Fig. 6.5 and Fig. 6.7 show that the depletion-induced change of effective stress can result in pronounced reductions of porosity and permeability. Grain crushing is the dominant mechanism for porosity-permeability loss under a high effective stress. Large grains tend to undergo more significant grain crushing than small grains. Therefore, grain crushing is an important grain-scale phenomenon that plays a significant role in reservoir compaction.

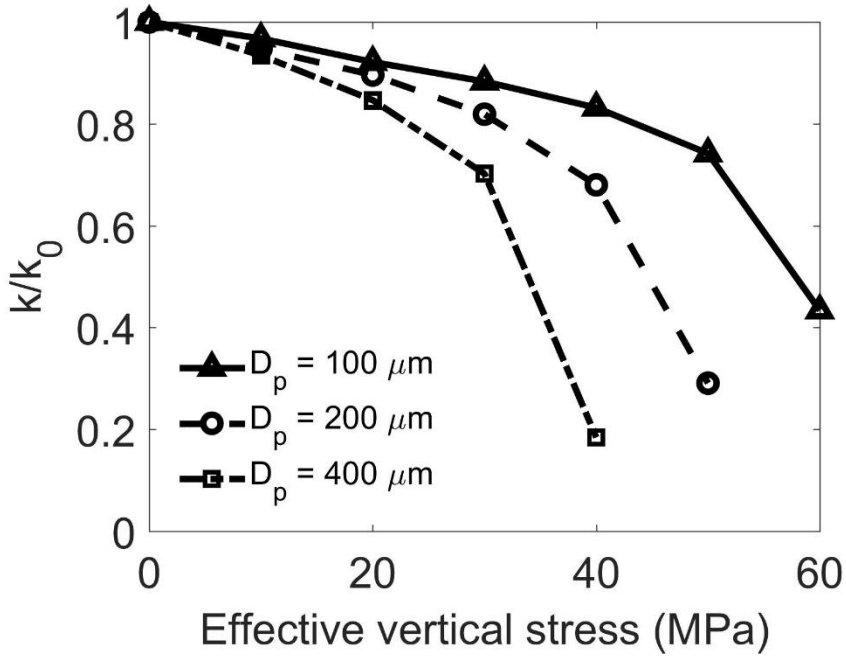

Figure 6.7: Change of normalized permeability as a function of effective stress. D_P is the grain size.

6.3.2 Effect of soft grains

Unconsolidated sands often contain soft grains such as micas, inclusions of shale fragments and weathered grains (Davies and Davies, 2001). These soft grains can deform easily even at low effective stress. Here, we investigate how the presence of soft grains changes the compaction behavior. Fig. 6.8 shows the numerical samples containing soft grains that are randomly distributed. We assume that the soft grains have 50% of the original elastic modulus and bond strength. All other parameters stay invariant as shown in Table 6.1. P_s represents the percentage of soft grains. The sample of P_s = 0% is the same as the numerical sample shown in Fig. 6.4, which is a 1.5 mm cube containing 484 agglomerates of 200 μm diameter.

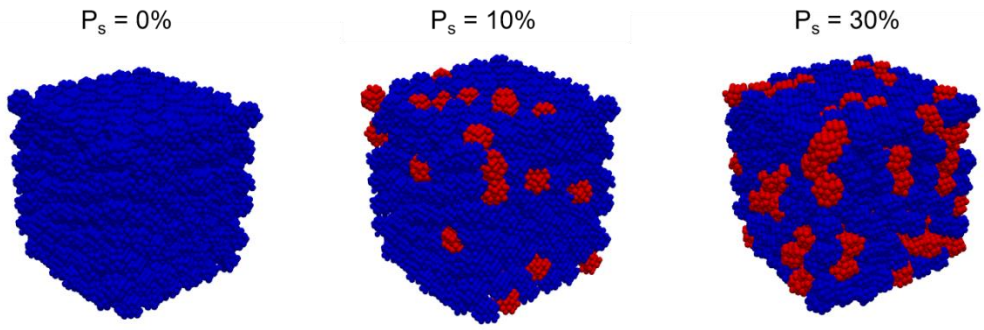

Figure 6.8: Numerical samples containing soft grains (in red). P_s is the percentage of soft grains.

We perform uniaxial strain tests on the numerical samples and obtain the respective changes of porosity and permeability using the same approach as described in the previous section. Fig. 6.9 shows the porosity/permeability-effective stress curves for samples containing different amounts of soft minerals.

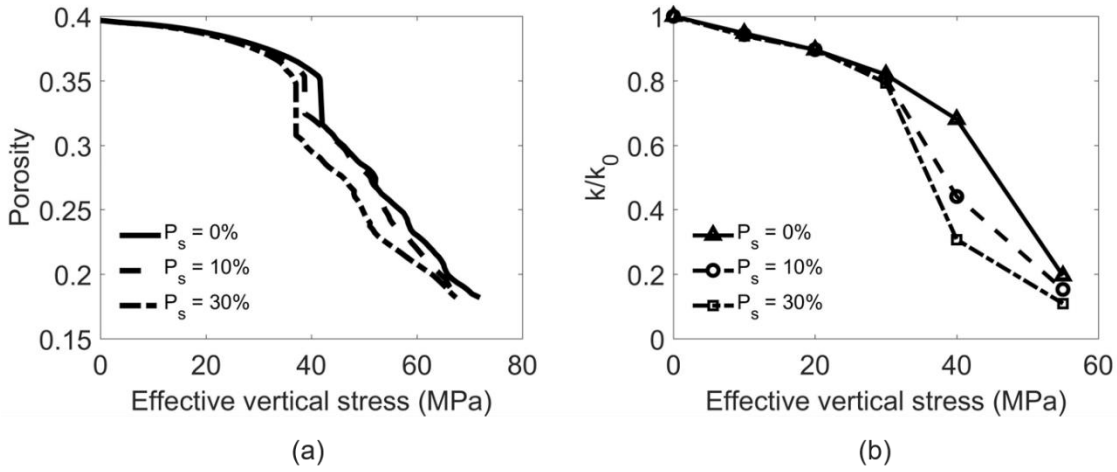

Figure 6.9: Changes of (a) porosity and (b) permeability as a function of effective stress for samples containing different amounts of soft minerals (represented by P_s).

The sample containing no soft grains (P_s = 0%) shows a steep decrease in porosity when the effective stress is around 40 MPa, which indicates the occurrence of grain

crushing behavior. The presence of soft grains decreases the threshold effective stress of grain crushing. The sample containing more soft grains (larger P_s) appears to be more readily compacted. The results indicate that the existence of soft grains facilitates the grain crushing and the associated compaction behavior.

6.3.3 Implications to reservoir-scale behavior

The compaction effect was characterized for the Ewing Bank Block 873 field located in south of New Orleans in the Gulf of Mexico (Petro et al., 1997). The field contained poorly consolidated hydrocarbon-bearing sands that were overpressured. The initial reservoir pressure is 50 MPa at 3262 m subsea depth and the water depth is 236 m. Therefore, the initial effective vertical stress is around 26 MPa. The formation is composed of quartz as the major mineral and minor amount of compliant clays. The change in normalized permeability is measured based on field production behavior from east and west performance area as shown in Fig. 6.10b. We compare the result shown in Fig. 6.9b with field data (Petro et al., 1997).

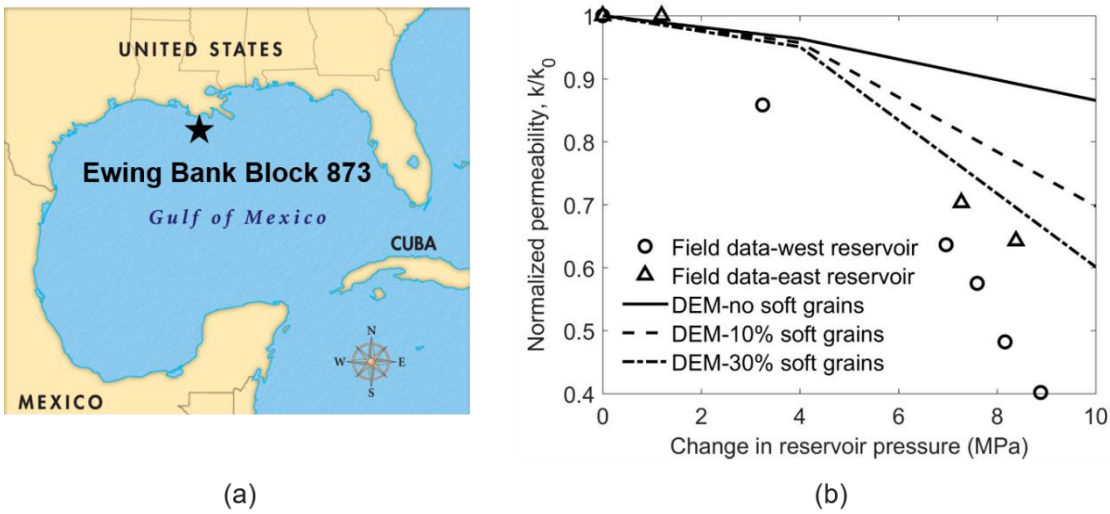

Figure 6.10: (a) Location of Ewing Bank Block 873 field. The map is from British Encyclopedia. (b) Comparison between the DEM results and field data from the Ewing Bank Block 873 field. The formation contains mainly quartz sands with minor amount of soft clays.

Fig. 6.10 shows that the DEM simulations can mimic the actual reservoir behavior of normalized permeability when considering the inclusion of soft grains. The discrepancy in Fig. 6.10b may be attributed to the simplistic assumptions used in the DEM for grain shape, clay mineral mechanical strength and stress state. The DEM simulation nevertheless can capture the grain crushing and the resulting sudden decrease on permeability change and provide an alternative approach other than experiments to study the compaction behavior of formations consisting of unconsolidated sands and clays.

6.4 CONCLUSIONS

We propose a pore-scale grain crushing model to study the compaction effect on porosity and permeability. To conclude, the numerical simulations in this chapter show that:

- Numerical agglomerates consisting of mono-sized bonded elementary spheres can reproduce the crushing strength of sand grains as a function of size.
- Numerical uniaxial strain test that represents the reservoir stress path can be used to obtain the changes of porosity and permeability as a function of effective stress.
- Grain crushing appears to be the dominant mechanism for large changes in porosity and permeability in sands under high effective stress.
- Numerical samples containing large and soft grains tends to be more readily compacted.

Chapter 7: CFD-DEM Modeling of Fluid-Driven Fracture Opening

7.1 INTRODUCTION

Fluid-driven fracture processes are ubiquitous under subsurface conditions and have important scientific and practical impacts. For instance, CO_2 injection into the storage formation can induce fractures and present risks to undesired migration of subsurface fluids. This work investigates the mechanisms of opening-mode fracture initiation based on grain-scale fluid-rock interactions. The resolved CFD-DEM approach models the solid phase using the fictitious domain method and can capture the particle-particle/fluid interactions even at high particle concentrations. The study presents a benchmark problem (seepage flow in a single column of spheres) in which the numerical resolved CFD-DEM approach is verified against the analytical solution. We also validate the resolved CFD-DEM model against experiments of fluid-driven deformation of a soft granular material (MacMinn et al., 2015). Additional results show fracture initiation mechanisms in a random granular packing subjected to constant boundary stresses and a fluid injection with localized source. This work, for the first time, uses the resolved CFD-DEM approach to study how particle-scale processes contribute to fluid-driven fracture initiation at the grain scale.

7.2 PARTICLE-LEVEL FORCES

At the particle level, the most important forces involved in the fluid-driven particle displacements include the weight of particles $W = \pi d_p^3 \rho g/6$, where d_p is the particle size and ρ is the mass density, the skeletal force $F_{sk} = \sigma d_p^2$, where σ is the local stress [N/m^2] acting on the particles, the capillary force $F_c = \pi d_p T_s$ due to an injection of immiscible fluid with interfacial tension T_s [N/m], and the seepage force $F_s = 3\pi\mu v d_p$ due to an injection of miscible fluid of viscosity μ traversing the pore space with a velocity v.

Fig. 7.1 shows the capillary forces and seepage forces caused by an injection of immiscible and miscible fluids into a medium made of grains. The capillary and seepage forces tend to result in grain separation at the fracture tip (i), grain convergence at the shoulder of the fracture (ii) and compaction in the far field (iii). When capillary and/or seepage forces are larger than the local skeletal force and the particle weight, a fracture opening or particle separation will occur. The particle size has a greater effect on the skeletal force (d_p^2) and particle weight (d_p^3) than capillary and seepage forces (d_p). Therefore, fine grains are more prone to fluid-driven fracture opening with capillary and seepage forces exceeding skeletal force. The van der Waals force describing the interaction between molecules remains negligible for the range of d_p in this study.

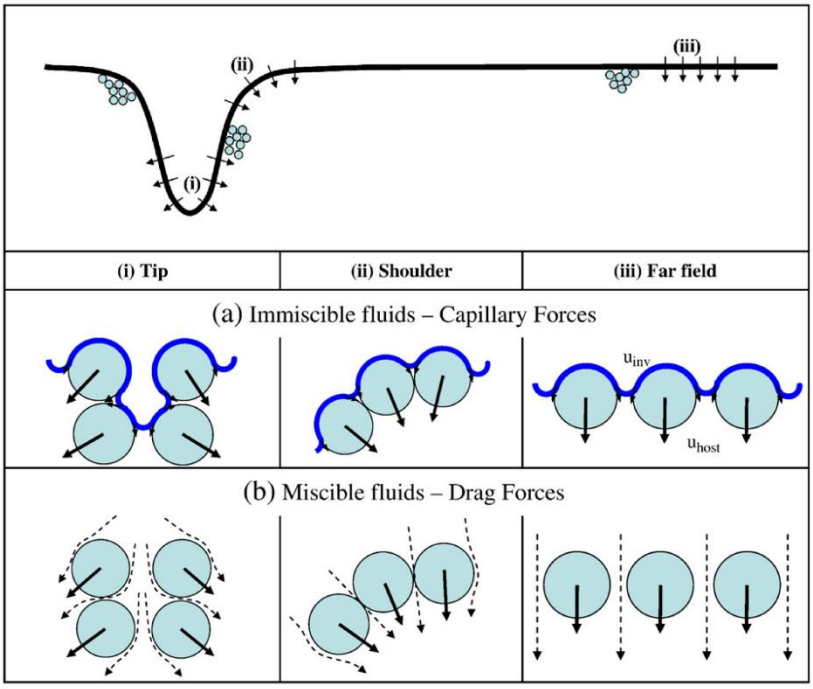

Figure 7.1: Capillary and seepage forces near a fracture during the invasion of (a) immiscible and (b) miscible fluids (Shin and Santamarina, 2010).

Fig. 7.2 shows various regimes of fracture opening due to an immiscible and/or miscible fluid invasion. A medium of coarse grains (large d_p) is usually presented by zone (a) with no particle separation. Capillary forces caused by the immiscible invasion can promote fracture opening in fine-grained media, as shown by zone (b). Fracture initiation driven by miscible fluids requires enough drag force to support the opened fracture walls (zone (c)). In other words, fracture opening benefits from fine-grained media, high fluid flow velocity, high fluid viscosity, and low effective confining stress (Khodaverdian and McElfresh, 2000). Capillary and seepage forces may also induce fracture opening under a mixed mode (zone (d)). In this chapter, we focus on the invasion of miscible fluids, which mostly results from the competition between seepage and skeletal forces.

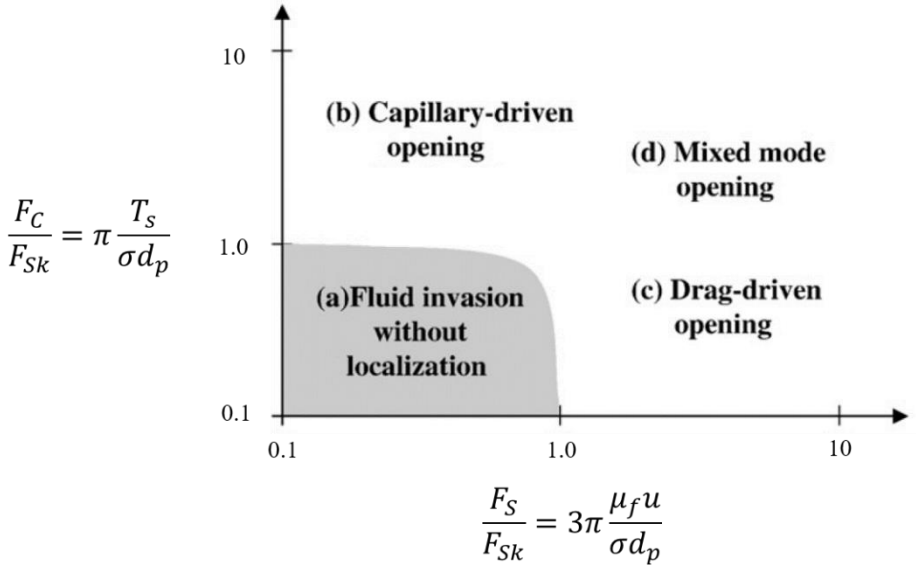

Figure 7.2: Regimes of fracture opening dependent on fluid and soil type and a force balance between capillary (F_c), seepage (F_s) and skeletal forces (F_{sk}). Modified from Shin and Santamarina (2010).

7.3 MODEL VERIFICATION

In this section, we verify the resolved CFD-DEM approach against a classic problem with an analytical solution: upward seepage flow in a single column of spheres.

We also validate the resolved CFD-DEM model against an experimental fluid-driven deformation of a soft granular material (MacMinn et al., 2015). Appendix B presents another two benchmark cases of (1) a settling single spherical particle in a fluid and (2) steady state fluid flow and pressure drop through a random particle packing (Sun et al., 2018a).

7.3.1 Seepage flow in a single column of spheres

The upward seepage flow in a single column of spheres is a classic problem with three stages. Fig. 7.3 shows a sketch of *N* spherical particles stacked in a monolayer column inside a square cross-sectional tube. All the particle-particle and particle-wall contacts are frictionless. In the first stage, the particles settle to equilibrium under the effect of gravity. The deformation at the contact of particle *i* and *i*-1 is:

$$\delta(i) = \frac{f_C(i)}{K_C^n} \tag{7.1}$$

where K_C^n is the normal stiffness and $f_C(i)$ is the contact force at contact *i*:

$$f_C(i) = \frac{4\pi R_p^3 \rho_p g}{3}(N - i + 1) \tag{7.2}$$

The deformation at ground surface S_g under gravity loading is the summation of deformation at all contacts:

$$S_g = \frac{4\pi R_p^3 \rho_p g}{3K_C^n} N(N+1) \tag{7.3}$$

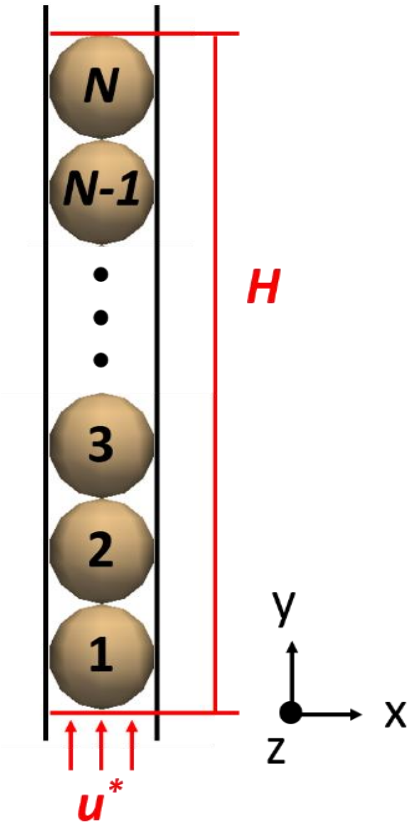

Figure 7.3: Schematic of the upward seepage flow in a single column of *N* spheres.

In the second stage, the tube is filled with a fluid of density ρ_f. The deformation at ground surface S_f caused by buoyancy can be calculated by replacing the particle density ρ_p in Eq. 7.3 with ρ_f:

$$S_f = \frac{4\pi R_p^3 \rho_f g}{3K_C^n} N(N+1) \tag{7.4}$$

In the third stage, fluid is injected with a constant velocity u^* from the bottom of the tube. The deformation at ground surface S_t due to the seepage force is predicted by the consolidation theory (Kiichi et al., 2007):

$$S_t = \frac{u^*}{C_v}\frac{H^2}{2}\left[1 - \frac{32}{\pi^3}\sum_{n=0}^{N}\frac{(-1)^n}{(2\pi+1)^3}e^{-T_v(2n+1)^2\pi^2/4}\right] \tag{7.5}$$

where C_v is the coefficient of consolidation and T_v is the time factor, defined as:

$$C_v = \frac{k}{m_v \rho_f g} \tag{7.6}$$

$$T_v = \frac{C_v t}{H_2} \tag{7.7}$$

where m_v is the coefficient of volume compressibility:

$$m_v = \frac{\Delta \varepsilon_v}{\Delta \sigma_v'} \tag{7.8}$$

where $\Delta\varepsilon_v$ is the volumetric strain and $\Delta\sigma_v'$ is the change in effective stress. With the porosity ϕ, the permeability coefficient k can be calculated based on the Ergun equation:

$$k = \frac{u^* \rho_f g}{\frac{150\mu}{d_p^2}\frac{(1-\phi)^2}{\phi^3}u^* + \frac{1.75\rho_f}{d_p}\frac{(1-\phi)}{\phi^3}\left(u^*\right)^2} \tag{7.9}$$

Han and Cundall (2013) simulated the upward seepage process in a single column of spheres based on a coupled LBM-DEM approach. Their simulation used periodic boundary conditions in the horizontal directions, constant pressure boundary at the top, and firstly no flow than constant velocity boundary at the bottom representing the second and third stage, respectively. Table 7.1 summarizes their model parameters:

Table 7.1: Model parameters of the LBM-DEM

Number of spheres, N	5
Particle diameter, d_p	1×10^{-3} m
Particle density, ρ_p	2560 kg/m^3
Normal contact stiffness, K_C^n	50 N/m
Gravity, g	9.81 m/s^2
Fluid density, ρ_f	1000 kg/m^3
Fluid viscosity, μ_f	0.01 Pa · s
Seepage flow velocity, u^*	5×10^{-4} m/s

The LBM simulation has 41 nodes in x- and z-directions and 281 nodes in the y-direction. The coefficient of volume compressibility m_v is calculated as 2×10^{-5} Pa^{-1} and the coefficient of permeability k is calculated as 2.576×10^{-3} m/s. We use identical parameters (Table 7.1) and boundary conditions for the resolved CFD-DEM approach. The CFD has structural meshes of 4 cells/d_p (Mondal et al., 2016b). Therefore, the CFD simulation has 4 cells in x- and z-directions and 28 cells in the y-direction. Note that the bottom and top of the fluid field are one diameter away from the ends of the sphere column to always maintain the spheres within the fluid after swelling and minimize the boundary effects (Han and Cundall, 2013).

Table 7.2 summarizes the results from the analytical, the LBM-DEM and the resolved CFD-DEM models, respectively. The three models predict very close deformations of the sphere column for all three stages.

Table 7.2: Comparison of analytical, LBM-DEM and resolved CFD-DEM models

	S_g (m)	S_f (m)	S_t (m)
Analytical	4.084×10^{-6}	1.541×10^{-6}	4.760×10^{-7}
LBM-DEM	4.084×10^{-6}	1.557×10^{-6}	4.651×10^{-7}
Resolved CFD-DEM	4.084×10^{-6}	1.560×10^{-6}	4.766×10^{-7}

7.3.2 Validation against experiments

MacMinn et al. (2015) injected a mixture of water and glycerol (61% glycerol in mass) into the center of radial disk filled with a monolayer of soft spherical polyacrylamide hydrogel particles and studied the poromechanical deformation of this system. Fluid injection can only result in a storage of elastic energy when the fluid pressure is comparable to the stiffness of the granular medium. Otherwise, the fluid-driven deformation is mostly irreversible because most of the input energy is dissipated through friction and particle

rearrangements that are not elastic. Therefore, extremely soft particles are used to construct a poroelastic system even at a low working pressure. They imaged the deformation field with a digital still camera and tracked the particle positions.

Their system contained ~25,000 spherical particles between two glass discs and was saturated with a mixture of water and glycerol. All packings have an initial porosity of ~0.51. A permeable spacer separating the two discs confined the outward movement of particles which allowed fluid to flow through. The particles were elastic, non-cohesive, incompressible (Poisson's ratio is zero), very slippery (coefficient of friction is zero) and follow the Hertzian contact mechanics. Table 7.3 shows the properties of the particles.

Table 7.3: Properties of soft spherical particles

Young's modulus, E	20 KPa
Poisson's ratio, ν	0.5
Coefficient of friction, μ	0
Mean diameter, d_p	1.2 mm
Standard deviation of diameter	0.12 mm

Fig. 7.4 shows a schematic of the experimental setup and the image of the deformation field at different times. The disc had a radius b of 105 mm. The injection port had a radius of 1.25 mm. The working fluid of a viscosity of 0.012 Pa·s was injected into two discs at a constant volumetric rate Q. The fluid flowed radially in the cell and exited through the spacer. This drives the particles moving outward and resulted in a cavity at the center. After the deformation reached an equilibrium state, they stopped the fluid injection and allowed the particles to relax under the elastic stress field. In other words, the cavity first opened then closed during the experiment.

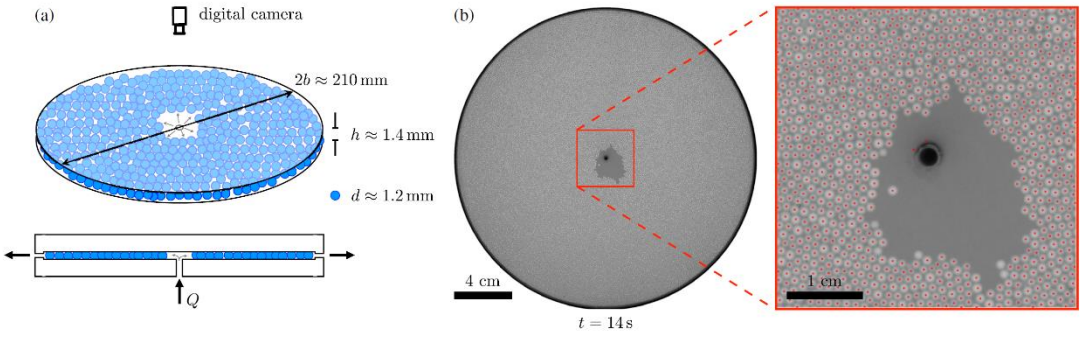

Figure 7.4: (a) Fluid is injected into a monolayer of soft spherical particles. The geometric parameters are given in the figure. (b) The high-resolution imaging and particle-tracking can give changes in the deformation field. (MacMinn et al., 2015).

We simulate this fluid-driven deformation behavior of soft particles using the resolved CFD-DEM model. Limited by the computational time, the domain of the simulation ($2b$ = 80 mm) is smaller that of the experiment ($2b$ = 210 mm). The particles have a uniform size of 1.2 mm. The packing has an initial porosity of ~0.46. Other model parameters are set equal to those in the experiment. Boundary conditions of the fluid flow include a constant injection rate into the injection port and an atmospheric pressure at the spacer. Fig. 7.5a shows the steady-state cavity shapes in the experiments and Fig. 7.5b shows the evolution of cavity in the numerical simulation. The color represents the particle displacements in the horizontal direction. Parameter t_D is the dimensionless time. Similar to the experiment, the fluid injection opens the cavity; then, the injection stops and the cavity closes indicating a macroscopic elastic deformation.

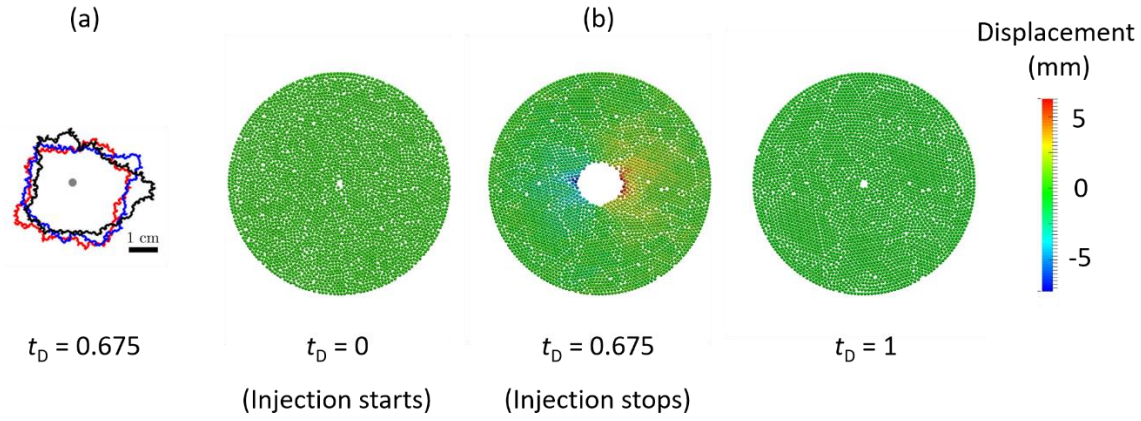

Figure 7.5: (a) The steady-state cavity shape in the experiments (MacMinn et al., 2015). Three curves result from three experiments, respectively. Note that the experimental packing is larger than the numerical packing. (b) Horizontal displacements of particles in the resolved CFD-DEM simulation. The cavity first opens then closes showing an elastic behavior. Parameter t_D is the dimensionless time.

The cavity shape in the experiments is not repeatable indicating the irreversible micromechanics, which is also implied by the states of $t_D = 0$ and 1 in the simulations. The simulated cavity tends to more symmetric about the injection port and smooth compared to the experimental cavity, which is due to the uniform particle size used in the numerical simulation. We normalize the time t and radial position r by domain radius b and characteristic time scale T_{pe} (Coussy, 2004; MacMinn et al., 2015):

$$r_D = \frac{r}{b} \tag{7.10}$$

$$t_D = \frac{t}{T_{pe}} \tag{7.11}$$

$$T_{pe} = \frac{\mu b^2}{Kk} \tag{7.12}$$

where μ is the fluid viscosity, K is the effective (drained) bulk modulus and k is the permeability. The dimensionless cavity area A_D is the ratio of the cavity area A and domain area πb^2:

$$A_D = \frac{A}{\pi b^2} \tag{7.13}$$

We compare the evolution of dimensionless cavity area A_D over the dimensionless time t_D from three experiments and our numerical simulation (Fig. 7.6). The injection rate Q is constant at 16 mL/min.

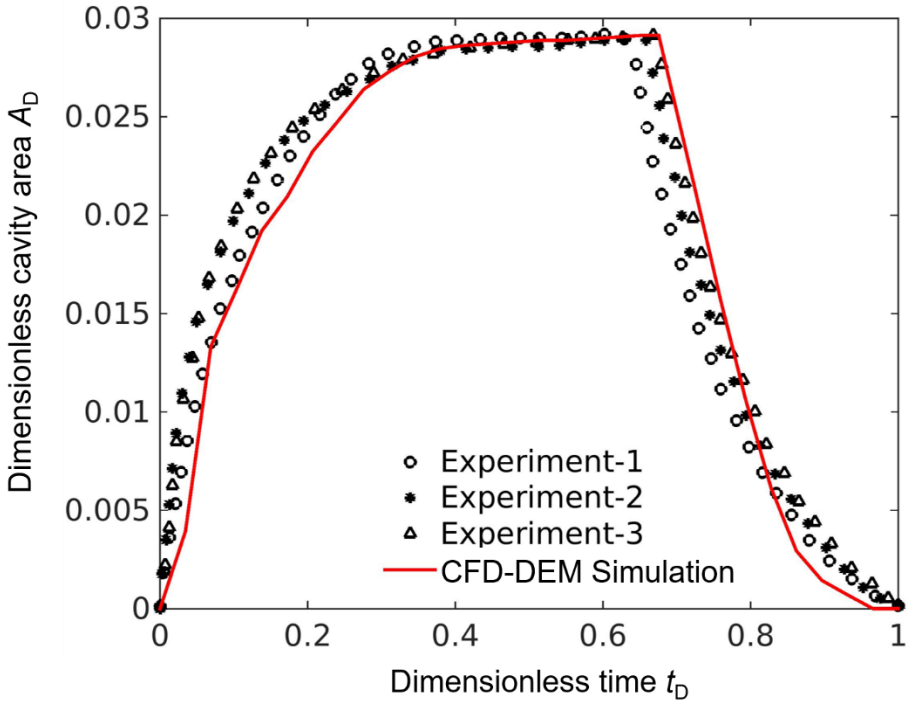

Figure 7.6: Comparison between three experiments (MacMinn et al., 2015) and our CFD-DEM numerical simulation.

Fig. 7.6 shows that the resolved CFD-DEM model predicts the fluid-driven deformation behavior measured in the experiments. The three experiments are a result of the injection-relaxation cycles repeated on the same group of particles. The variability between them under an identical operational condition indicates that the particle spatial distribution can affect the macroscopic mechanics. The change in cavity area essentially results from a force balance between the drag force and the elastic contact force caused by

a fluid-driven compaction. The resolved CFD-DEM approach can capture well the fluid-particle and particle-particle interactions and therefore give a similar macroscopic deformation behavior. The experiments have limitations of soft granular material and a fixed confinement. However, the numerical CFD-DEM model allows flexibility in granular micromechanical properties, fluid characteristics, and boundary conditions. In the following section, we will investigate the fracture opening induced by fluid injection into a granular medium based on the resolved CFD-DEM model.

7.4 Results and Discussion

7.4.1 Fluid-driven fracture opening model

We create a numerical packing of 5061 spherical particles with a diameter of 2 μm as one layer within the 100 μm × 200 μm rectangular domain. We apply constant stress boundaries on the top and two lateral sides and use a stress ratio (the vertical stress σ_v over the horizontal stress σ_h) of 4, which is the maximum stress ratio that can be imposed without inducing a shear failure. The bottom boundary has no displacement. Appendix C shows the shear failures caused by a large stress ratio. After the packing reaches a steady stress state, the fluid is injected from the inlet port placed at the bottom-center. The fluid flows through the particle packing and exits from the top and two sides with a constant outlet pressure. The CFD meshing is uniform with 4 cells per particle diameter.

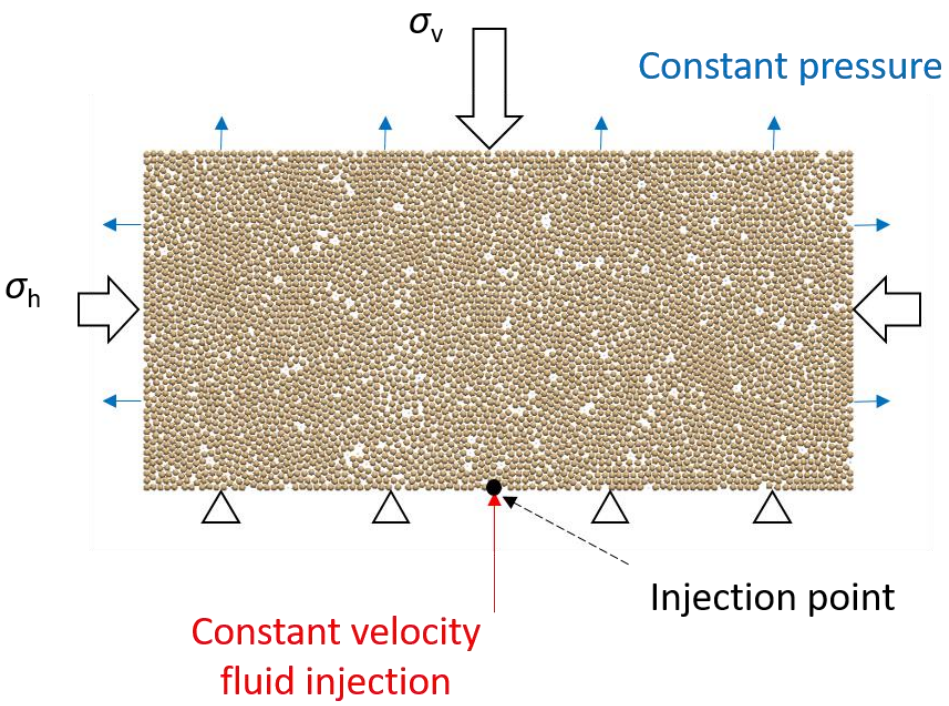

Figure 7.7: Schematic of CFD and DEM boundary conditions of the random particle packing. σ_v and σ_h are vertical and horizontal stresses, respectively. $\sigma_v = 4\times\sigma_h$.

Fig. 7.7 illustrates the domain and boundary conditions used in the CFD and DEM simulations. Table 7.4 summarizes the model parameters for the base case. Fluid injection tends to permeate rather than create a localized fracturing channel in a medium of coarse grains. Therefore, fine grains are used to facilitate the fracture opening. The Reynold's number Re is calculated as 10^{-5} indicating a laminar flow regime.

$$\mathrm{Re} = \frac{\rho u d_p}{\mu} \tag{7.14}$$

Table 7.4: Model parameters of CFD-DEM simulation

Particle Young's modulus, E	1 MPa
Poisson's ratio, v	0.3
Coefficient of friction, μ	0.5
Particle diameter, d_p	2 μm
Particle density, ρ_p	2650 kg/m^3
Vertical stress, σ_v	20 KPa
Fluid injection Darcy velocity, u	5 mm/s
Fluid viscosity, μ_f	1 Pa·s
Fluid density, ρ_f	1000 kg/m^3

The base case simulation is performed with the parameters given in Table 7.4 and models the fracturing opening process within a time period of 0.04 s. The simulation is paralleled and takes ~ 40 hours on two Intel i7-3820 3.60GHz processors. Unlike consolidated samples, the unconsolidated particle packing has little or no tensile strength. Experiments have shown that the fracture initiation in a packing of unconsolidated particles is determined by fluid invasion and shear failure ahead of the fracture tip (Khodaverdian and McElfresh, 2000; Zhai and Sharma, 2005). Therefore, it is important to characterize the shear strain localization in the particle packing. Rotation is the integration of angular velocity over time and can represent the local shear behavior of particles. Fig. 7.8a shows the rotation field of particles at the end of the simulation.

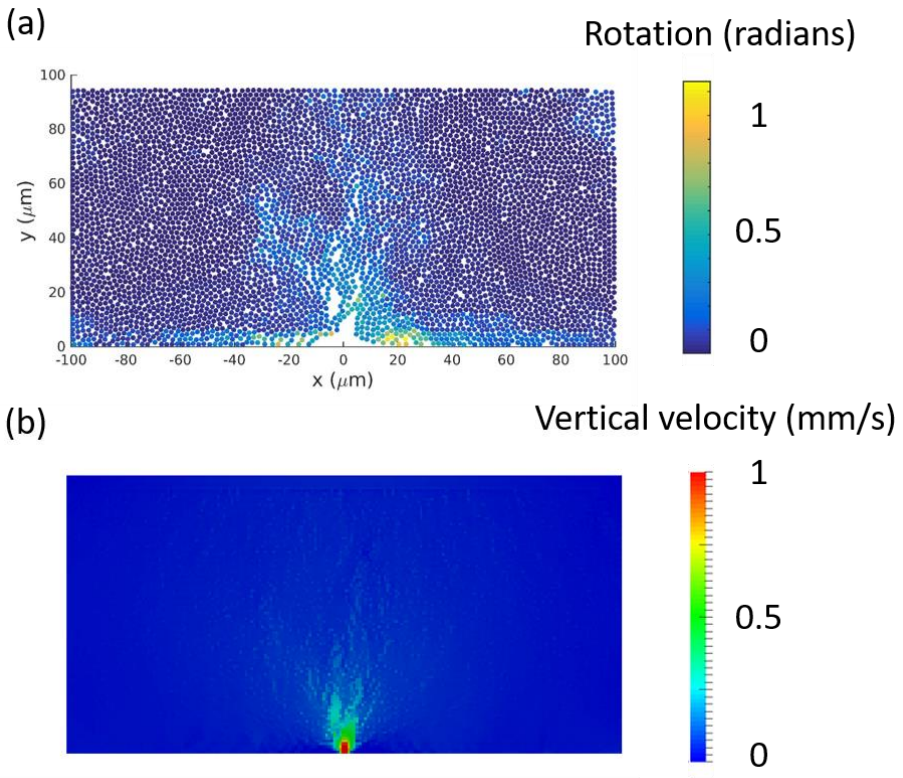

Figure 7.8: (a) Rotation field of particles after a fracture opening in the base case. (b) Field of fluid velocity in the y-direction. The injection velocity is 5 mm/s. The upper limit shown in the figure is selected as 1 mm/s to better visualize the velocity field far from the inlet port.

Fracture initiation manifests through opening-mode particle displacement. Fig. 7.8a shows that fracture initiates from the fluid injection point and propagates perpendicularly to the minimum principal stress. Similar to the experiments (Khodaverdian and McElfresh, 2000; Huang et al., 2012b), our simulation shows complex and sub-parallel fractures induced by the fluid drag force. The fluid flow is localized in the opened fracture channels and supports the fracture walls against the applied boundary stresses. There exists a sheared zone near the fracture face which indicates that the fracture opening in unconsolidated particles is dominated by shear failure. This behavior is shown to be independent of the domain size because a larger simulation domain will yield a similar result.

7.4.2 Sensitivity Analysis

The fluid-driven fracture opening in granular media features large deformations and small-scale microstructures that result in a strong nonlinear coupling between the fluid flow and geomechanics. The classical theory of poroelasticity assumes a linear coupling between Darcy's law and elasticity and therefore is not applicable for this problem. The resolved CFD-DEM model presented in this chapter enables us to investigate the fracture initiation as a collective behavior of pore-scale processes. Sensitivity analyses can help to explain the impact of injection parameters and physical properties. As illustrated in Section 7.2, the dimensionless variable F_s/F_{sk} defining the ratio of seepage force and skeletal force can be a criterion separating regimes of fluid invasion and drag-driven fracture opening.

$$\frac{F_s}{F_{sk}} = 3\pi \frac{\mu_f u}{\sigma d_p} \tag{7.15}$$

where μ_f is the fluid viscosity, u is the injection velocity, σ is the applied stress, d_p is the particle size. In this section, we will perform sensitivity analysis of the dimensionless variable F_s/F_{sk} and other important parameters but not included in Eq. 7.15.

7.4.2.1 Effect of dimensionless variable F_s/F_{sk}

The dimensinolesss variable F_s/F_{sk} is changed from 0.047 to 47 by increasing the fluid viscosity from 0.01 Pa·s to 10 Pa·s. All other parameters stay invariant as shown in Table 7.4. Fig. 7.9 shows the displacement patterns for tests with a different F_s/F_{sk}. The rotation represents the local shear behavior of particles induced by the fluid flow. When the F_s/F_{sk} is relatively small as 0.047, the particles exhibit nearly negligible displacements. The fluid flow tends to shear the particles that are loosely contacted to the neighbors, which results in the randomly high local rotation. When the F_s/F_{sk} increases to 0.47, the particle displacements remain negligible whereas the sheared zone becomes localized at the fluid

injection inlet. For the cases (a) and (b) in Fig. 7.9, the flow regime is dominated by the infiltration rather than the fracture opening.

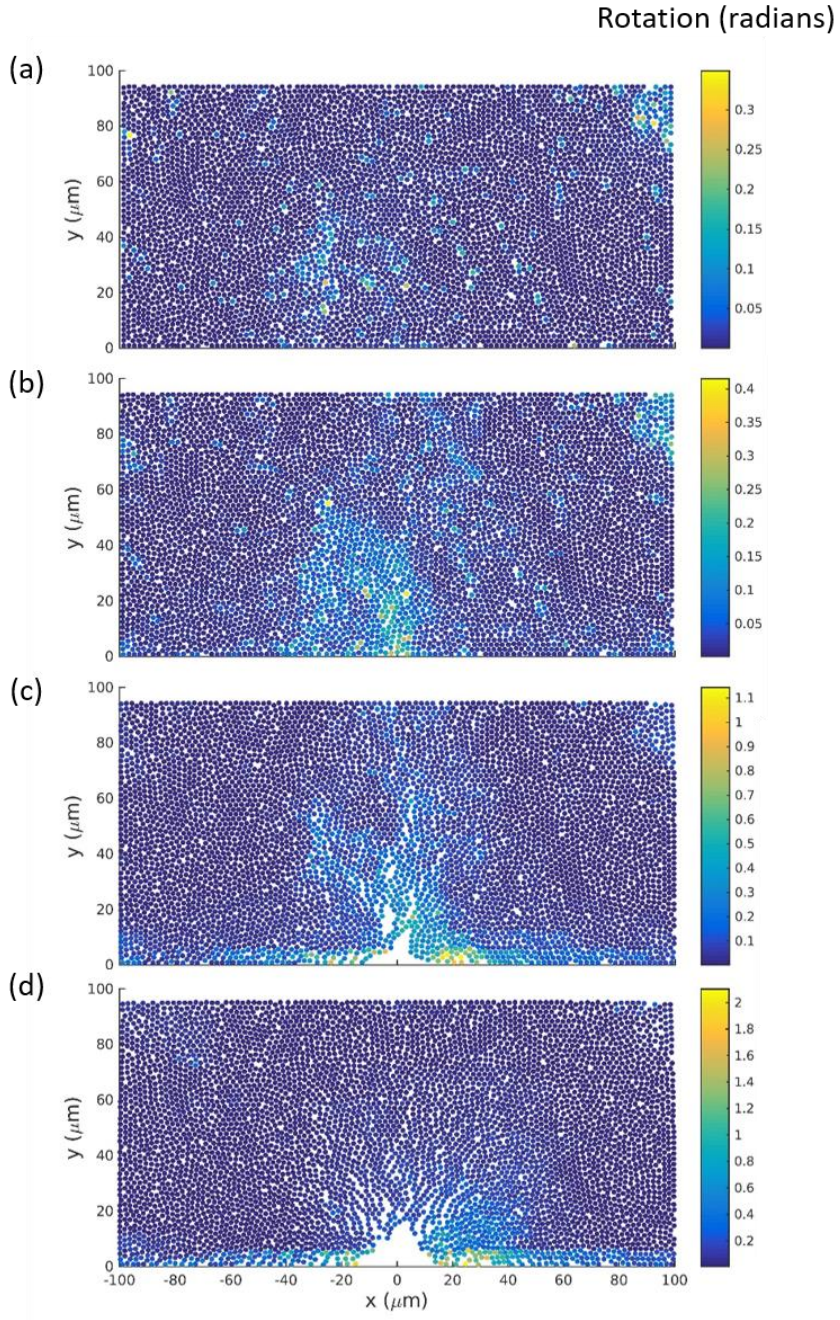

Figure 7.9: Effect of the dimensionless variable F_s/F_{sk} on the fracture opening. From (a) to (d), F_s/F_{sk} changes from 0.047, 0.47, 4.7 and 47.

As the F_s/F_{sk} increases to 4.7, a fracture opening occurs, which indicates a transition from the infiltration-dominated regime to the grain-displacement dominated regime. The created fluid channel profile is relatively complicated with a main channel and several branches. The fracture initiates from the fluid injection point and propagates perpendicularly to the minimum stress direction under the anisotropic principal stresses. The field of particle rotations shows that the fluid also permeates into the granular medium and induces a shearing on the particles. The sheared zone exhibits a similar shape to the created fractures. As the F_s/F_{sk} further increases to 47, the fluid flow induces a short and wide cavity rather than a long and thin fracture as shown for a lower fluid viscosity. The high fluid viscosity inhibits the infiltration therefore results in a grain-displacement dominated regime. The particle displacements induced by seepage drag forces lead to changes in effective stress and strains at the macro-scale. For instance, the particles in the far field shown in Fig 7.9c-d experience a compaction and store the strain energy at all the particle contacts.

7.4.2.2 Effect of the particle micromechanical properties

In this section, we investigate effects of the particle micromechanical properties including Young's modulus, Poisson's ratio and coefficient of friction on the fracture opening. The base case uses the parameters given in Table 7.4 (Fig. 7.10a). Fig. 7.10b shows the simulation result by increasing the particle Young's modulus from 1 MPa to 10 MPa. The granular medium becomes stiffer and shows an increase in the height of y-direction when the particle Young's modulus is increased. The created fracture tends to be thin for a granular medium consisting of stiff particles. However, the sheared zone remains similar in the shape. Therefore, an increase in particle Young's modulus appears to inhibit the fracture opening but barely affects the fluid infiltration.

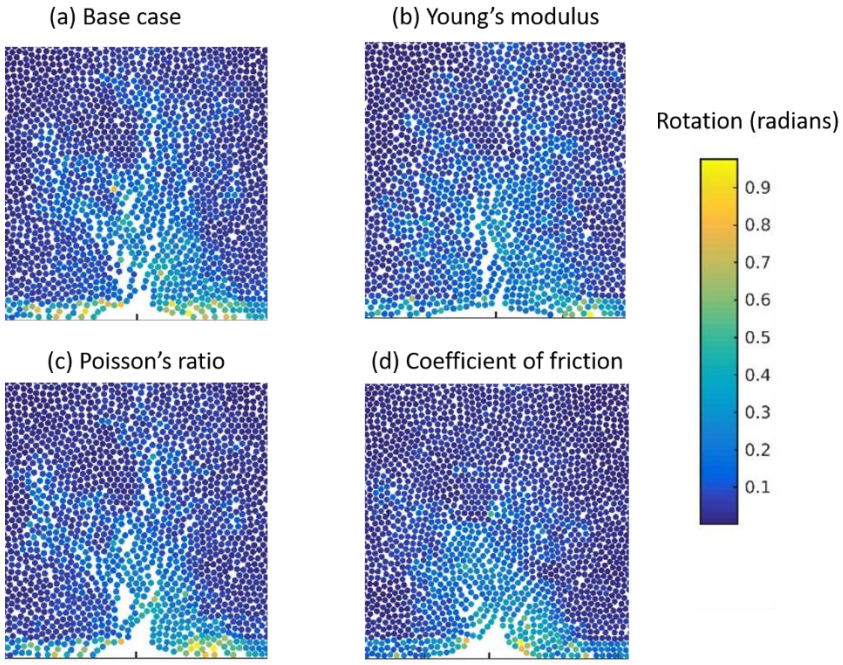

Figure 7.10: Effect of particle micromechanical properties, Young's modulus, Poisson's ratio and coefficient of friction, on the fracture opening. The zoomed-in domain is of 80 × 80 μm. The base case (a) uses the parameters given in Table 7.4.

Fig. 7.10c shows the simulation result by decreasing the particle Poisson's ratio from 0.3 to 0.1. The shear modulus is defined through the Young's modulus and the Poisson's ratio. The particle Poisson's ratio only has a slight impact on the fracture opening, which indicates an insignificant effect of the particle shear modulus. Fig. 7.10d shows the simulation result by decreasing the coefficient of friction from 0.5 to 0.1. The coefficient of friction μ indicates the roughness of particle surface. For instance, the particles with a parameter μ of 0 are slippery. As the coefficient of friction decreases, the created fracture becomes short and wide, which is due to the fact that the particle surfaces are no longer rough enough to support a complicated flow channel. A decrease in the coefficient of friction will result in a similar cavity as the increase in the fluid viscosity whereas not significantly affect the sheared zone and fluid infiltration.

7.4.2.3 Effect of the stress anisotropy

The fracture opening is also conditioned by the stress anisotropy. It is generally recognized that the fracture tends to propagate in a direction normal to the minimum stress direction (Hoek and Bieniawski, 1965; Zhou et al., 2008; Khodaverdian et al., 2010). In this section, we apply a vertical-to-horizontal stress ratio σ_v/σ_h of 1, 2 and 4 and investigate the resulting fracturing behavior. The horizontal stress σ_h is constant as 5 KPa. Fig. 3.11 shows the simulation results of different stress ratios. As the stress anisotropy decreases, i.e. from case (a) to case (c), the fracture length decreases and the fracture width increases. For an isotropic stress state (case (c)), the fracture no longer propagates along the vertical direction whereas a relatively uniform cavity expansion occurs, even though the fluid is injected from the vertical direction. Higher stress anisotropy is expected to increase the likelihood of shear failure and facilitate the fracture propagation (Olson et al., 2011).

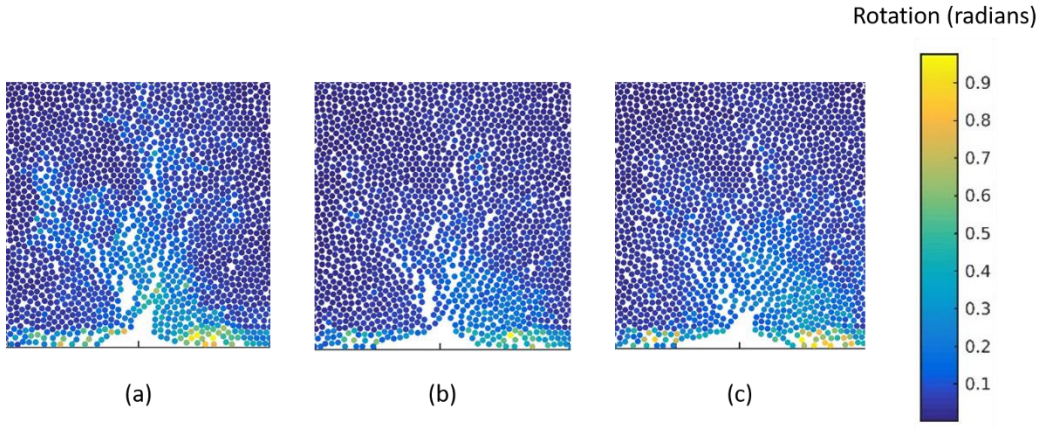

Figure 7.11: Effect of stress anisotropy on the fracture opening. The zoomed-in domain is of 80 × 80 μm. The stress anisotropy is changed from (a) σ_v/σ_h = 4, (b) σ_v/σ_h = 2 and (c) σ_v/σ_h = 1. The horizontal stress σ_h is constant as 5 KPa. All other parameters stay invariant as Table 7.4.

7.4.3 Regimes of fracture opening

Huang et al. (2012a) injected aqueous glycerin solutions into dense dry Ottawa F110 sand and found that the flow regime is dependent on the interplay between fluid infiltration and grain displacement. In their experiments, when the injection velocity and the fluid viscosity are relatively small, the flow regime is dominated by the infiltration with negligible flow channels. As the injection velocity and the fluid viscosity increase, the transition from the infiltration-dominated regime to the grain-displacement dominated regime occurs, which is consistent with our simulation results. Classification of these displacement regimes in unconsolidated granular media shows similarities with that of fracture propagation regimes in competent rocks (Detournay, 2004; Adachi and Detournay, 2008).

The dimensionless time τ_1, which is the ratio of the injection time t_i and the diffusion time from hydromechanical coupling t_d, can be used to classify the two displacement regimes (Huang et al., 2012a).

$$\tau_1 = \frac{t_d}{t_i} = \frac{\mu_f u l}{Ek} \tag{7.16}$$

$$t_d = \frac{\eta l^2}{Ek} \tag{7.17}$$

$$t_i = \frac{l}{u} \tag{7.18}$$

where μ_f is the fluid viscosity, u is the injection velocity, l is the characteristic length, E is the small strain Young's modulus and k is the permeability. We take the fluid injection inlet width as the characteristic length. The Young's modulus of the medium is shown to be proportional to the particle Young's modulus while the particle Poisson's ratio is maintained constant (Zhang et al., 2013). We approximate the particle Young's modulus as the effective medium modulus considering the difficulty in measuring the mechanical

properties of the 2D packing. The permeability of the particle packing is a function of the porosity and the particle size.

In the experiments only the fluid viscosity and the injection velocity were varied, but in our simulations we investigate effects of all relative parameters such as the fluid viscosity, injection velocity, particle micromechanical properties, particle size and applied stress. For each case scenario, we calculate the dimensionless parameters τ_1 and F_s/F_{sk} and summarize all results in Fig. 7.12.

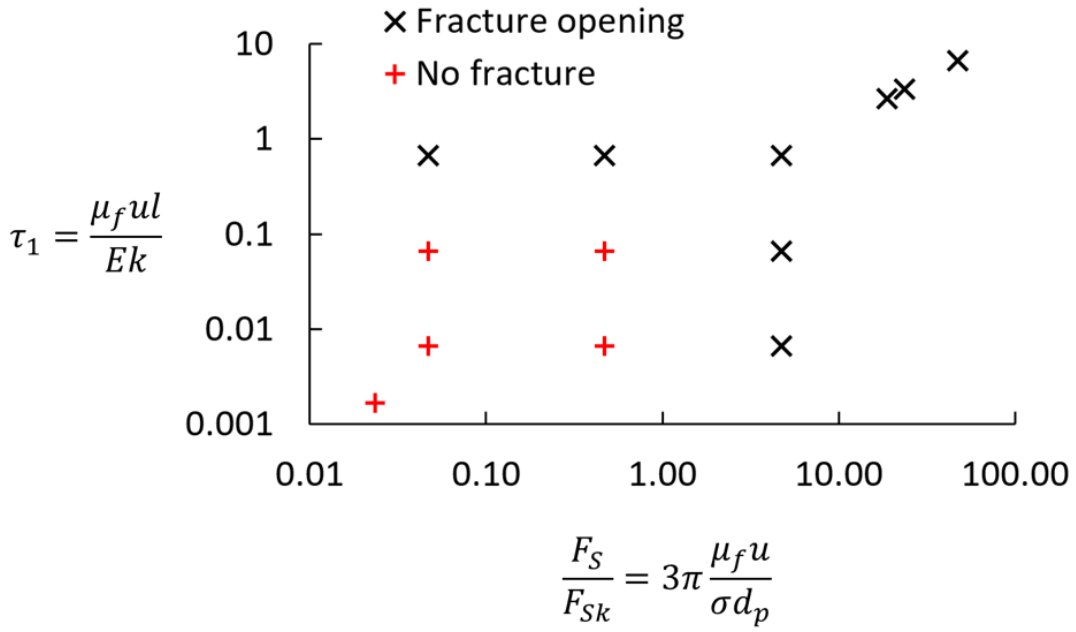

Figure 7.12: Determination of the fracture regime based on the dimensionless parameters τ_1 and F_s/F_{sk}. Each point is the result of a simulation using various parameters including the fluid viscosity μ_f, injection velosity u, Young's modulus E, particle size d_p/permeability k and applied stress σ.

Fig. 7.12 shows that the dimensionless parameter τ_1 or F_s/F_{sk} alone is not sufficient to describe the displacement regimes of miscible fluid injection into a packing of particles. For instance, it is possible to initiate a fracture opening in a relatively soft granular medium even when F_s/F_{sk} is smaller than 1. The results show that these two dimensionless

parameters in combination result in a good indicator of fracture opening. In other words, when either τ_1 or F_s/F_{sk} is greater than the threshold value, a fracture opening will occur. In the literature, the threshold value τ_d is numerically and experimentally obtained as 0.44 and 0.1, respectively (Huang et al., 2012b; Zhang et al., 2013), which is consistent with the results shown in Fig. 7.12. The threshold value of F_s/F_{sk} appears to be 1, which indicates that the seepage force should be greater than the skeletal force. Fig. 7.12 essentially adds another dimension to the regimes of fracture opening in Fig. 7.2 (Shin and Santamarina, 2010).

7.5 CONCLUSIONS

In this chapter, we present a numerical model based on the resolved Computational Fluid Dynamics (CFD) and Discrete Element Method (DEM). The numerical approach is validated against a benchmark problem with analytical solutions and an experiment of fluid-driven deformation of soft granular medium. We investigate the fracture initiation mechanisms in a random granular packing subjected to constant boundary stresses and to fluid injection with a localized source. Fracture initiates from the fluid injection point and propagates normal to the minimum principal stress. Sensitivity analyses help to explain the impact of physical properties and injection parameters including fluid viscosity/injection velocity, grain micromechanical properties, grain size and principal stresses. Simulation results show that the fracture initiation and propagation is facilitated by a large fluid viscosity, a compliant granular material and a large stress anisotropy. Poisson's ratio is shown to have minor impact on the fracture opening. The coefficient of friction, i.e. the particle surface roughness, can result in a change of the fracture geometry. We find that the dimensionless parameters τ_1 and F_s/F_{sk} in combination can classify the regimes of fracture opening. When either τ_1 or F_s/F_{sk} is greater than the threshold value, a fracture opening will

occur. This work, for the first time, uses the resolved CFD-DEM approach to study how particle-scale processes contribute to fluid-driven fracture initiation at the grain scale.

Chapter 8: Conclusions and Recommendations for Future Directions

8.1 CONCLUSIONS

In this study, we investigate several coupled chemo-hydro-mechanical processes based on numerical approaches. The numerical model couples the Discrete Element Method (DEM) and the Bonded-Particle Model (BPM) to perform simulations on synthetic rocks that mimic tested rock samples. The fluid flow through a granular medium is modeled by coupling the Computational Fluid Dynamics (CFD) with the Discrete Element Method (DEM).

We quantitatively investigated the effect of CO_2-related mineral dissolution through numerical modeling and validation of indentation, scratch and triaxial tests performed on geologically altered Entrada Sandstone. For sandstones with interparticle cements more susceptible to CO_2-water mixture alteration than grains, the numerical results support our hypothesis that CO_2-related mechanical rock degradation in Entrada sandstones can be ascribed to the degradation of interparticle cementation. The CO_2-related degradation on cementation in Entrada sandstone is due to the reduction of cement size, which indicates that the CO_2-alteration occurs on the surface of cements.

Scratch toughness decreases as the cement size is reduced, which is associated with the brittle to ductile transition. A small amount of cement dissolution can lead to a large change in scratch toughness. We propose a simple approach to quantify the brittleness based on the coefficient of variation of bond breakage rate in DEM simulations. True scratch toughness can only be obtained when the normal force is larger than the threshold, below which the sample exhibits abnormal scratch toughness and brittleness due to the surface roughness. Cement bond size reduction and full particle dissolution are two likely mechanisms of CO_2-induced alteration on Entrada Sandstone. Cement size is the most

likely bond microscopic parameter controlling the DEM numerical sample brittleness. On the contrary, full grain dissolution has small impact on the brittleness. Numerical results in agreement with experimental evidence show that cement dissolution contribute greatly to rock weakening in sandstones with carbonate/hematite cements. An alteration path that mimics the mineral dissolution under stressed condition leads to (1) vertical compaction and horizontal stress relaxation in the reservoir rock and (2) transfer of stresses to adjacent strata that results in microseismic events and potentially natural fracture reactivation at a larger scale.

We investigated the changes in porosity and permeability induced by compaction. The DEM-based grain crushing model with two-sized subgrains can mimic the crushing strength of rounded sand and the uniaxial strain behavior of a sand pack. Grain crushing can induce a large change in porosity, which becomes more evident for larger grains. Numerical agglomerates consisting of mono-sized bonded elementary spheres can reproduce the crushing strength of sand grains as a function of size by changing the bond shear strength. Numerical uniaxial strain test that represents the reservoir stress path can be used to obtain the changes of porosity and permeability as a function of effective stress. Grain crushing appears to be the dominant mechanism for large changes in porosity and permeability in sands under high effective stress. Numerical samples containing large and soft grains tends to be more readily compacted.

Last but not the least, we attempt to better understand the fluid-driven fracture initiation and address two problems: (1) the grain-scale mechanism of fracture initiation induced by fluid flow; and (2) the effects of fluid characteristics, grain micromechanical properties and stress state on the fracture opening. The resolved CFD-DEM approach can accurately model the fracture initiation at the grain scale. Large fluid viscosity/injection velocity, small particle modulus and small stress anisotropy are shown to facilitate the grain

displacement and fracture opening. The Poisson's ratio of particles appears to only have a slight impact whereas the coefficient of friction (particle surface roughness) can induce a change in the fracture geometry. We propose to combine two dimensionless parameters τ_1 and F_s/F_{sk} to classify the fluid-grain displacement regimes and determine if that is an infiltration-governed or displacement-governed regime.

8.2 Recommendations for Future Directions

The numerical simulations in this study are mostly based on a randomly generated particle packing. Although random particle assemblage can also represent the rock sample in general, it is necessary to develop to a bonded-particle pack extraction technique that can be applied to any 3D image of interest. This is particularly true for rock samples with rather complex microstructures, for instance, carbonate rocks. Micro-x-ray computerized tomography (micro-CT) can image microstructures of a wide range of rocks. The 3D image from micro-CT can be readily transformed into a network of pores and throats with parametric geometries (Dong and Blunt, 2009). Similar to the pore-network extraction from micro-CT image, a bonded-particle pack can also be extracted from the image for grain/cement and used in the DEM-BPM modeling. Boned-particle pack can be constructed through a variety of methods including Delaunay tessellation, medial axis method, maximum ball algorithm and watershed transform. Compared with other methods, watershed transform is widely used for grain partitioning (Sheppard et al., 2006; Thompson et al., 2008). In watershed transform, grains/cements are obtained by growing local maxima until all connected voxels are found. Software such as ImageJ/Fiji can be used as the tool to extract bonded-particle pack from original 3D micro-CT image. Compared with randomly generated sphere packs used in the preliminary results, cements can be initialized for bonded particles with overlap/separation based on the local morphology. Overlap

between particles could be a potential challenge for subsequent DEM modeling. Slight overlap is allowed in the DEM simulation. For too much overlap, we have to merge the grains which appear to be part of the same body. The grain partitioning based on watershed transformation has been applied to sphere packs, unconsolidated cores, sandstones and carbonates (Sheppard et al., 2006). Geometric parameters measured from the construction include grain radius, ratio between grain radius and the radius of each neighboring grain contact, and ratio between grain radius and the radius of a sphere with the same volume as the grain. It could be challenging to extract a distribution of bond radii and other rock properties from the micro-CT image.

Another important phenomenon during CO_2 geologic storage is the rock creep (time-dependent behavior), which may jeopardize the structural integrity of reservoir rock, wellbore, caprock, and faults in the long term. However, it still remains challenging to characterize these processes due to a lack of knowledge regarding the underlying mechanisms. It is generally accepted that the time-dependent damage, deformation and fracture behavior of rocks arise from subcritical crack growth that is due to stress corrosion at crack tips (Atkinson and Meredith, 1987). It describes the thermally activated fluid-rock reactions and occurs at strained defects in the rock comprising open pores, grain boundary voids, open microcracks that act as stress concentrators. Therefore, a pore-scale model may be required to study rock failure behavior caused by the stress corrosion. The Parallel-bonded Stress Corrosion (PSC) model can describe the microscopic stress corrosion process, which is implemented by removing the bonding surface material at a rate of crack velocity that is related to the stress state (Potyondy, 2007). The time-dependent damage and deformation of the numerical sample then arises from the propagation and coalescence of microcracks and can be characterized by a creep curve. Therefore, another recommendation for a future direction is to describe the time-dependent behavior of rocks

by capturing the pore-scale rock structure and microcrack evolution rather than phenomenological degradation in mechanical properties.

The resolved CFD-DEM model couples single-phase fluid flow with the granular medium. However, in order to describe the particle-CO_2-water flow, it is necessary to consider a multi-phase fluid flow. The Volume of Fluid (VOF) method can locate the free surface between CO_2 and water through the calculation of liquid saturation in computational cells. Parameter $\mathbf{u}_r$, which represents the relative velocity between gas and liquid phases, is used to compress the interface to a sharper region. Another transport equation for liquid saturation is added to the CFD-DEM. More details about the implementation of VOF in the CFD-DEM can be found elsewhere (Jing et al., 2016). The fracture opening should be more favored in the water saturated sample rather than the dry sample. It is of great significance to investigate the fracture initiation induced by multi-phase fluid flow in consolidated/unconsolidated formations.

In this study, we focus on experimental or numerical samples that are isotropic. However, many rocks, including sedimentary and metamorphic rocks, have structural anisotropy which leads to anisotropic response to loading or unloading. The micro structure of anisotropic rocks is critical for both deformation and damage processes. The impact of preferred weak layers on the fracture growth in anisotropic rocks is not well understood. Numerical simulations provide an opportunity to systematically study the anisotropic rock mechanical behavior. Park and Min (2015) represented the transversely isotropic rocks by a bonded-particle pack with a set of continuous smooth joints, which model the continuous weak planes often encountered in fractured rocks. However, the anisotropy essentially originates from mineral structure, layers, foliation, or banding, which are not necessary to be continuous at the particle scale. The Smooth-Joint Model (SJM) replaces the bonds with smooth joints that are assigned to all contacts between particles which lie on opposite sides

of the joint. Parameters associated with the SJM are correlated with parameters of bonds and particles (Duan et al., 2016). The SJM could be used to investigate the mechanical behavior of anisotropic rocks, for instance, shale caprock which is of special interest in CO_2 sequestration. The fracture propagation is expected to be under the synergistic impact of the anisotropy and the effective stress in anisotropic rocks. The anisotropy may play a positive role in CO_2 secure storage especially when the favored propagation direction is horizontal rather than vertical. Therefore, I also suggest a quantitative investigation on the effect of direction of pre-existing weak planes.

Appendices

A. Another Pore-Scale Grain Crushing Model[5]

We represent a crushable grain with an agglomerate of bonded subgrains, such that there is a large subgrain surrounded by small subgrains of the same size. Bonds are added to the particle contacts. The size ratio between large and small subgrains is r^* ($r^* \geq 1$). The introduction of a large subgrain reduces the number of contacts and significantly saves computational cost of simulations that involve grain crushing. Fig. A.1 shows a cross-section schematic of the 3-D grain crushing model.

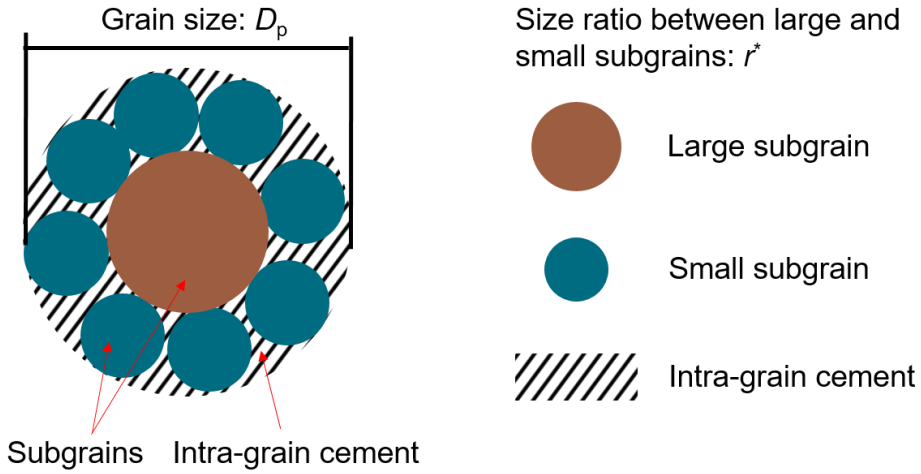

Figure A.1: Cross-section view of a crushable grain which contains bonded subgrains. The volume of intra-grain cement is included when calculating the sample porosity

The intra-grain bonds develop intra-grain cementation, which we assume fills all the void space between subgrains. Therefore, the packing porosity in the following sections refers to the inter-grain porosity. The inputs of this grain crushing model are the

[5] Zhuang Sun, Hewei Tang, D. Nicolas Espinoza, Matthew T. Balhoff, John E. Killough (2018). Discrete Element Modeling of Grain Crushing and Implications on Reservoir Compaction. Journal of Petroleum Science and Engineering. 171, 431-439.
I performed the research and wrote the manuscript with support from M.T. Balhoff, D.N. Espinoza, H. Tang and J.E. Killough.

micromechanical parameters and the geometrical parameters including grain size D_p and subgrain size ratio r^* (Fig. A.1).

Fig. A.2 shows a crushable grain with $r^* = 2$ consisting of one large subgrain, 25 small subgrains and 35 bonds. The applied load leads to the grain crushing which manifests as a reduction of bond number or a decrease of reaction force. Fig. A.3 shows the change of measured force as a function of the displacement of the upper wall.

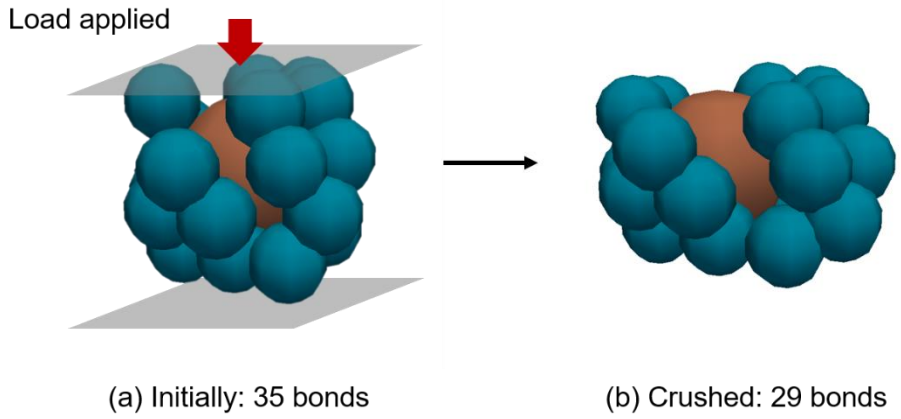

Figure A.2: Schematic of single grain crushing test. Some small subgrains are close but not in contact. Intra-grain bonds are added to the particle contacts. The applied load crushes the particle and breaks some bonds. The top wall moves at a velocity of 0.05 m/s.

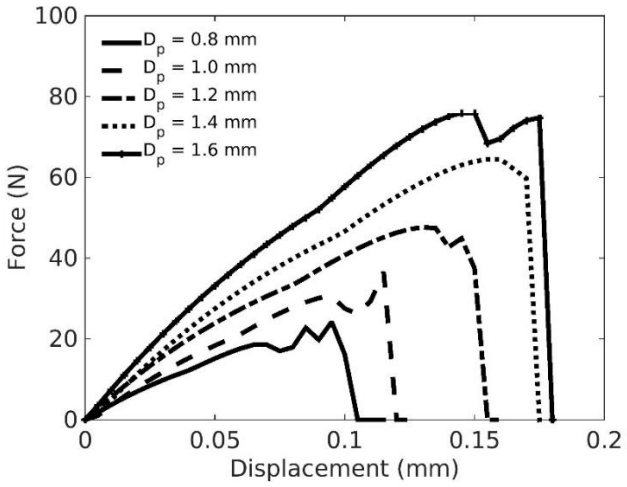

Figure A.3: Single grain crushing test results for grains with different diameters D_p. Subgrain size ratio $r^* = 2$.

We perform single grain crushing tests on grains with various diameters D_p and obtain the force-displacement curves. Table A.1 summarizes the model parameters. Small decreases in force result from particle fracturing (and subgrain debonding) from the sides, which is also observed in experiments without particle splitting in the middle (Nakata et al., 1999). Larger grains tend to have a higher peak force. However, the characteristic grain crushing strength decreases as the particle size increases.

Table A.1: Calibrated model parameters for various subgrain size ratios r^*.

Parameters	$r^* = 1$	$r^* = 2$	$r^* = 4$
E (GPa)	4	4	40
k_T/k_N	1	1	1
λ	0.5	0.5	0.5
σ_c (GPa)	0.1	1	2
τ_c (GPa)	0.3	3	8

Model parameters in Table A.1 result from calibrations against experimental data of single grain crushing tests on quartz sands (Nakata et al., 1999) (Fig. A.4). We perform

numerical single grain crushing tests on three types of grains with r^* = 1, 2 and 4. A larger r^* results in more intra-grain contacts and thus increases the computational cost to run simulations. Table A.2 summarizes the number of subgrains and bonds for various types of grains. Fig. A.4 shows the comparison between numerical and experimental results of single grain crushing tests. Each point results from one force-displacement curve as shown in Fig. A.3.

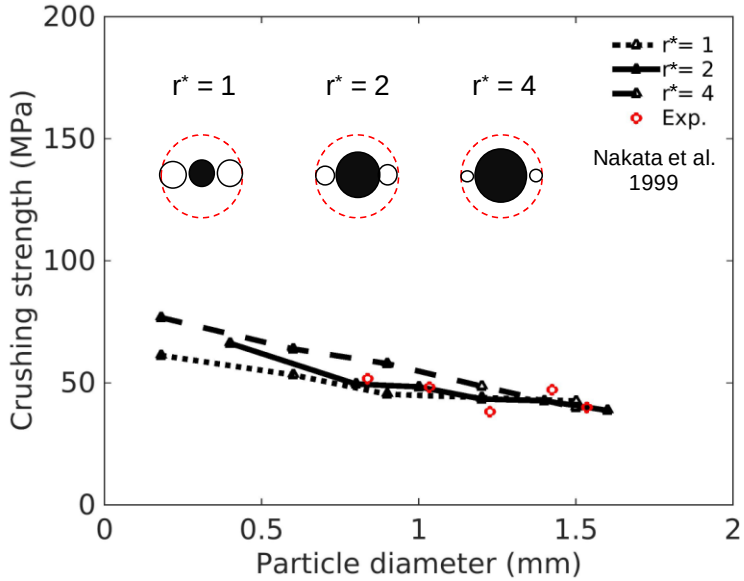

Figure A.4: Results of single grain crushing tests on grains with various subgrain size ratio r^*. Experimental data are from Nakata et al. (1999).

Table A.2: Number of subgrains and bonds of a single grain

Number	$r^* = 1$	$r^* = 2$	$r^* = 4$
Subgrains	18	26	60
Bonds	30	35	81

With the calibrated parameters in Table A.1, all three types of digital grains can reproduce the change of crushing strength with grain size. The sand particles used in experiments are beach sands from Yamaguchi in Japan. Note that the real sands behave

diverse in grain shape, mineral composition and distribution of incipient flaws and these factors may contribute to the discrepancy between the experimental and numerical results (Nakata et al., 1999). Small quartz particles tend to have a larger crushing strength because of a lower likelihood of being flawed (Nakata et al., 1999). Bonded particle agglomerate has a similar trend which is likely due to the scale effect that intra-grain bonds in smaller agglomerate are more closely distributed. Subgrain size ratio r^* is shown to have a significant impact on the calibrated model parameters. Grains with larger r^* are calibrated with higher intra-grain bonding strength. Although the digital grain has reproduced the quartz sand crushing strength as a function of grain size, it is still unknown if these digital grains with various r^* could reproduce the crushing behavior of a grain packing. Therefore, we further perform the uniaxial strain tests on grains with $r^* = 1$, 2 and 4.

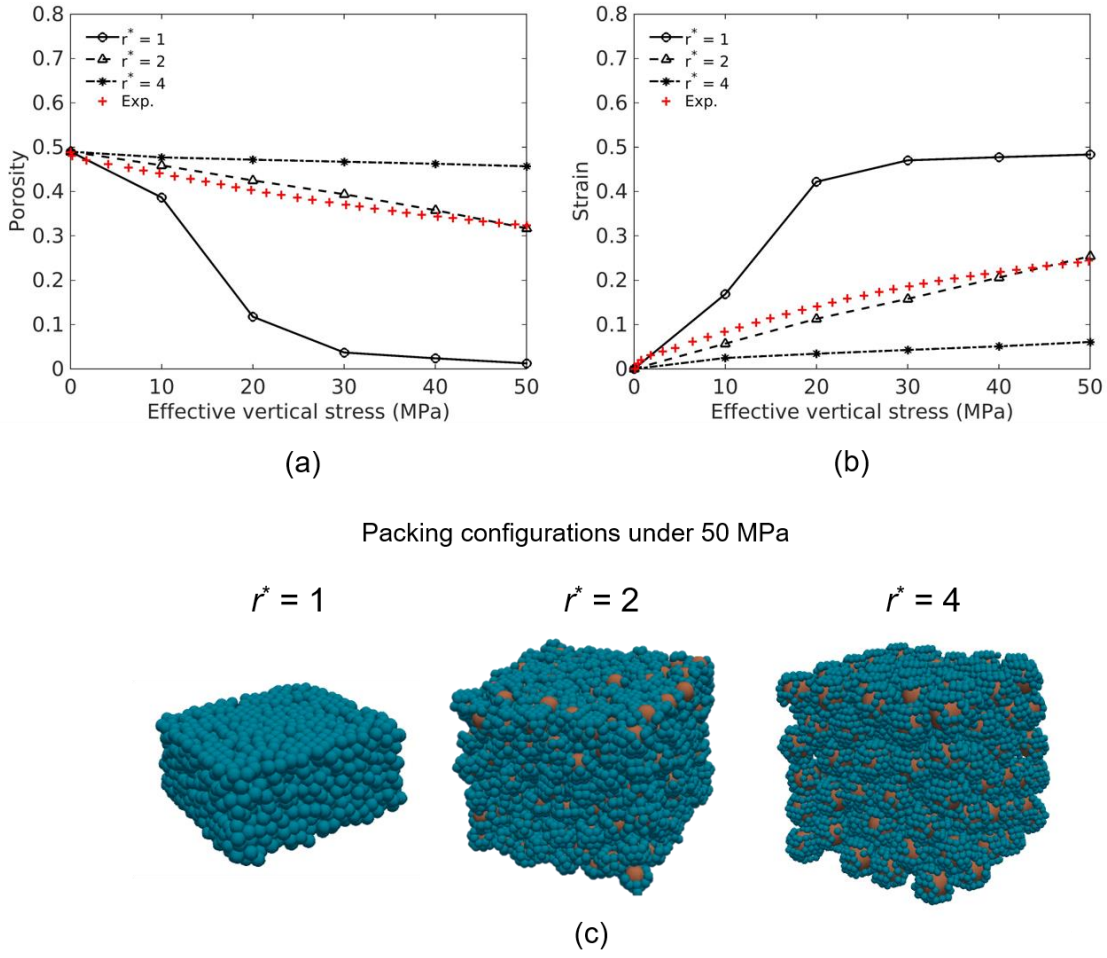

Figure A.5: Validation of the compaction model against experimental results of (a) porosity and (b) vertical strain. Experimental data is from Chuhan et al. (2002). The micro-mechanical parameters are calibrated though a single grain crushing test. (c) Grain packing configurations of various subgrain size ratio r^* when the effective stress is 50 MPa

Fig. A.5a-b shows the comparison between numerical and experimental results of the porosity and vertical strain. The model parameters are the same as shown in Table A.1. Therefore, all digital crushable agglomerates have a characteristic strength similar to the quartz sand grains. The results indicate that the geometrical ratio r^* has a significant impact on the sample deformation behavior. The packings with r^* = 1 and 4 yield incorrect

estimations of strain and the resulting porosity. When $r^* = 1$, the high effective stress results in unrealistically low porosity due to the significant particle overlap. Therefore, subgrain size ratio $r^* = 2$ yields the most appropriate estimation of porosity and vertical strain change. Grain crushing occurs in the forms of corner breakage or particle splitting (Zhao and Song, 2015). A small or large subgrain size ratio r^* cannot simultaneously capture these two mechanisms well. For instance, grains with $r^* = 4$ can only mimic the process of corner breakage due to the large core subgrain. On the contrary, grains with $r^* = 2$ account for the two mechanisms more appropriately and thus reproduce the experimental results.

B. Another Two Benchmark Cases for the Resolved CFD-DEM Approach

In this section, we benchmark the resolved CFD-DEM approach against another two classic problems with analytical solutions. They are (1) a settling single spherical particle in a fluid and (2) steady state fluid flow and pressure drop through a random particle packing. These two cases adopt four-way and one-way coupled CFD-DEM framework, respectively. In other words, we measure the pressure drop for steady state fluid flow with fixed particles

B.1 Settling of single particle

The settling of a single spherical particle in an infinite fluid is described by Stokes's law for very small Reynolds numbers (Re ≤ 2) (Liu et al., 2018b):

$$V_s = \frac{(\rho_p - \rho_f) g d_p^2}{18 \mu_f} \tag{B.1}$$

where V_s is settling velocity, d_p is the particle diameter, particle mass density ρ_p = 2.65 g/cm^3, fluid density ρ_f = 1 g/cm^3, gravity acceleration g = 9.8 m/s^2, and fluid viscosity μ_f = 1 cp.

Accordingly, we use the resolved CFD-DEM approach to model particle settling. Fig. B.1 shows a snapshot of velocity field when the particle is falling. The particle is placed in the center of an unbounded fluid domain. We show a cross-sectional view which exhibits one quarter of the entire simulation domain. We dynamically refine the local meshing around the particle to save computational cost.

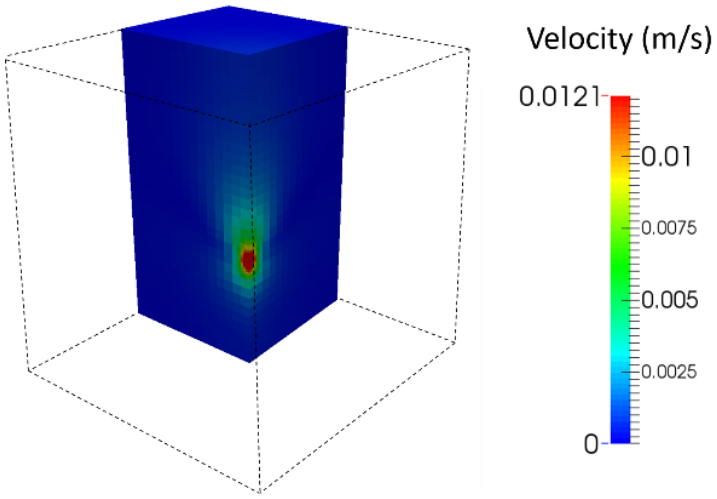

Figure B.1: Velocity field when a single spherical particle is settling. The settling particle is placed in the center. One quarter of the simulation domain is shown.

We measure the settling velocity for different particle diameters d_p. Fig. B.2 shows the comparison between results of the numerical CFD-DEM simulations and the analytical Stokes's law. Simulations are capable of predicting the settling velocity of a single particle.

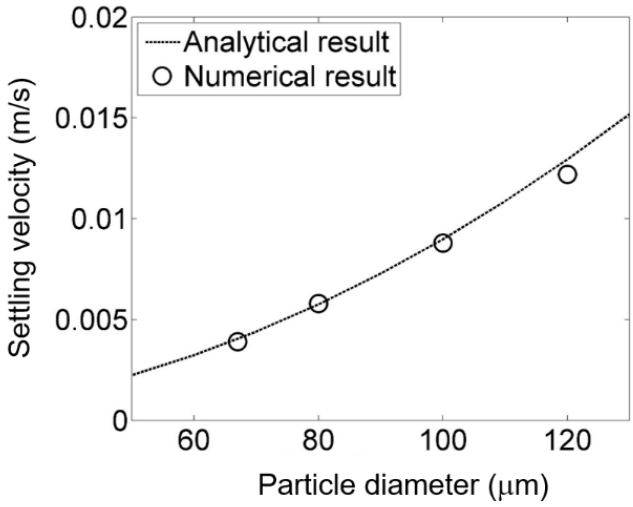

Figure B.2: Settling velocity for different particle diameters obtained from analytical Stokes's equation and numerical resolved CFD-DEM model.

B.2 Pressure drop through random packing

The pressure drop of a laminar and steady state fluid flow through a random packing follows the Kozeny-Carman equation (Carrier, 2003).

$$\frac{\Delta P}{L} = \frac{150\mu_f V_0}{d_p^2}\frac{(1-\phi)^2}{\phi^3} \tag{B.2}$$

where V_0 is the superficial velocity and ϕ is packing porosity.

Fig. B.3 shows the velocity and pressure field through the random particle packing. The 1.5 mm cubic packing has 403 particles of 200 μm diameter. The porosity ϕ is equal to 46%. The fluid viscosity μ_f is 1 cp. CFD domain has a length of 1.3 mm, which is slightly smaller than the packing length (1.5 mm) to avoid boundary effects. We simulate fluid injection with constant flow velocity from the top. The bottom outlet pressure is constant and equal to 100 kPa. We measure the inlet pressure to calculate the pressure gradient.

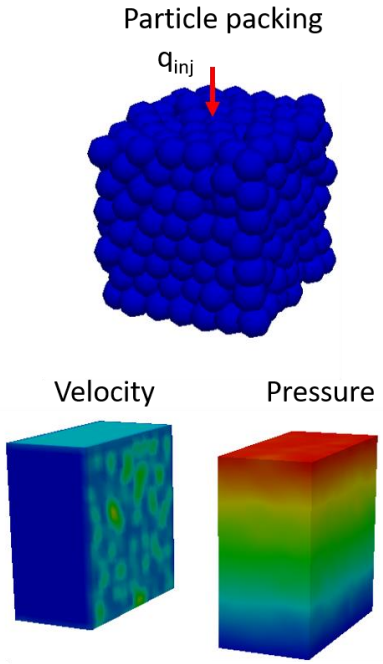

Figure B.3: Fluid pressure drop through a random particle packing by the resolved CFD-DEM approach.

Fig. B.4 shows the change of pressure drop with different fluid injection velocities (Re < 1). We compare the numerical CFD-DEM results with the analytical results based on Kozeny-Carman equation. The results indicate that the resolved CFD-DEM approach is applicable to predict the pressure drop.

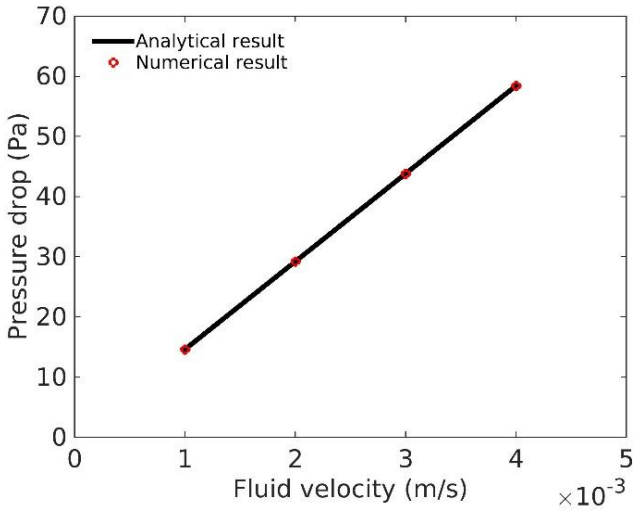

Figure B.4: Verify the numerical resolved CFD-DEM approach against the analytical Kozeny-Carman equation on pressure drop through a random particle packing.

C. Shear Failures Caused by a Stress Anisotropy

This section shows the simulations of shear failure caused by a large stress ratio. The horizontal stress σ_h is constant as 5 KPa and the vertical stress σ_v is defined by the stress ratio. Fig. C.1 shows the displacements of particles in x-direction under a stress state of σ_v/σ_h = 5, 6, 8 and 10. The results indicate that a shear failure will occur under a stress ratio larger than 4. Therefore, the stress ratio used in chapter 7 maintains below this threshold to eliminate the shear failures induced by a stress anisotropy.

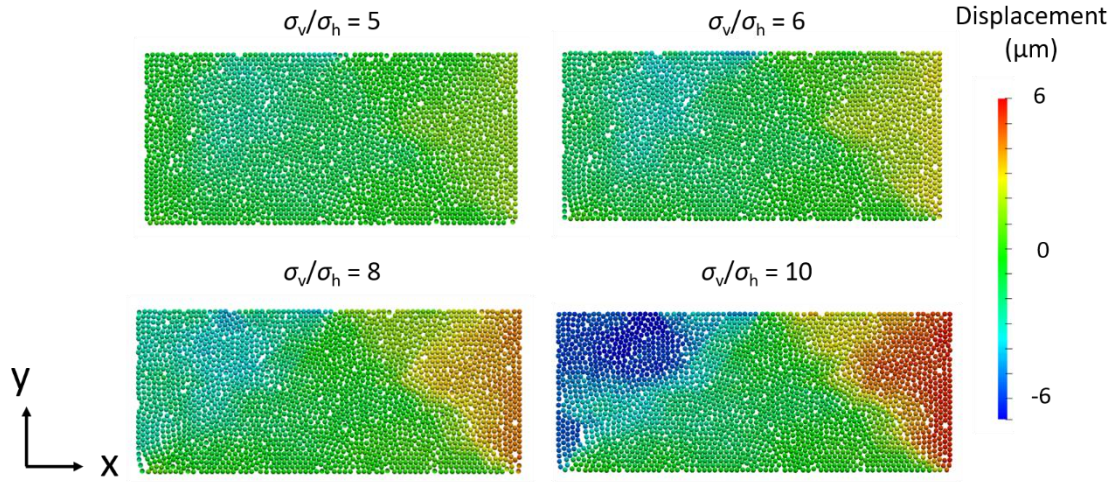

Figure C.1: A stress ratio larger than 4 will induce a localized shear failure. The color represents the displacement of particles in x-direction.

References

Adachi, J. I., and E. Detournay. 2008. Plane strain propagation of a hydraulic fracture in a permeable rock. *Eng. Fract. Mech.* 75:4666–4694.

Adachi, J. I., E. Detournay, and A. Drescher. 1996. Determination of Rock Strength Parameters From Cutting Tests. American Rock Mechanics Association.

Aharonov, E., and D. H. Rothman. 1993. Non-Newtonian flow (through porous media): A lattice-Boltzmann method. *Geophys. Res. Lett.* 20:679–682.

Akono, A.-T., N. X. Randall, and F.-J. Ulm. 2012. Experimental determination of the fracture toughness via microscratch tests: Application to polymers, ceramics, and metals. *J. Mater. Res.* 27:485–493.

Akono, A.-T., and F.-J. Ulm. 2012. Fracture scaling relations for scratch tests of axisymmetric shape. *J. Mech. Phys. Solids* 60:379–390.

Akono, A. T., P. M. Reis, and F. J. Ulm. 2011. Scratching as a fracture process: From butter to steel. *Phys. Rev. Lett.* 106:2–5.

Alehossein, H., E. Detournay, and H. Huang. 2000. An Analytical Model for the Indentation of Rocks by Blunt Tools. *Rock Mech. Rock Eng.* 33:267–284.

Alejano, L. R., and E. Alonso. 2005. Considerations of the dilatancy angle in rocks and rock masses. *Int. J. Rock Mech. Min. Sci.* 42:481–507.

Alonso, E. E., M. Tapias, and J. Gili. 2012. Scale effects in rockfill behaviour. *Géotechnique Lett.* 2:155–160.

Aman, M. D., D. N. Espinoza, A. Ilgen, J. Major, P. Eichhubl, and D. T.A. 2017a. CO2-induced chemo-mechanical alteration in reservoir rocks assessed via batch reaction experiments and scratch testing. *Greenh. Gases Sci. Technol.*

Aman, M., D. N. Espinoza, A. G. Ilgen, J. R. Major, P. Eichhubl, and T. A. Dewers. 2017b. CO2-induced chemo-mechanical alteration in reservoir rocks assessed via batch reaction experiments and scratch testing. *Greenh. Gases Sci. Technol.*

Andreev, G. 1995. Brittle failure of rock materials: test results and constitutive models. Rotterdam: A.A. Balkema.

Assayag, N., J. Matter, M. Ader, D. Goldberg, and P. Agrinier. 2009. Water–rock interactions during a CO2 injection field-test: Implications on host rock dissolution and alteration effects. *Chem. Geol.* 265:227–235.

Åström, J. A., and H. J. Herrmann. 1998. Fragmentation of grains in a two-dimensional packing. *Eur. Phys. J. B - Condens. Matter Complex Syst.* 5:551–554.

Atkinson, B. K., and P. G. Meredith. 1987. The theory of subcritical crack growth with applications to minerals and rocks. *Fract. Mech. Rock*:111–166.

Au, S. K. A., K. Soga, M. R. Jafari, M. D. Bolton, and K. Komiya. 2003. Factors Affecting Long-Term Efficiency of Compensation Grouting in Clays. *J. Geotech. Geoenvironmental Eng.* 129:254–262.

Ayoub, J. A., J. M. Kirksey, B. P. Malone, and W. D. Norman. 1992. Hydraulic Fracturing Of Soft Formations In The Gulf Coast. *SPE Form. Damage Control Symp.* Society of Petroleum Engineers, Lafayette, Louisiana.

Bachu, S. 2008. CO2 storage in geological media: Role, means, status and barriers to deployment. *Prog. Energy Combust. Sci.* 34:254–273.

Bachu, S., and D. B. Bennion. 2009. Experimental assessment of brine and/or CO2 leakage through well cements at reservoir conditions. *Int. J. Greenh. Gas Control* 3:494–501.

Bachu, S., D. Bonijoly, J. Bradshaw, R. Burruss, S. Holloway, N. P. Christensen, and O. M. Mathiassen. 2007. CO2 storage capacity estimation: Methodology and gaps. *Int. J. Greenh. Gas Control* 1:430–443.

Bagherzadeh Kh., A., A. A. Mirghasemi, and S. Mohammadi. 2011. Numerical simulation of particle breakage of angular particles using combined DEM and FEM. *Powder Technol.* 205:15–29.

Bakker, E., S. J. T. Hangx, A. R. Niemeijer, and C. J. Spiers. 2016. Frictional behaviour and transport properties of simulated fault gouges derived from a natural CO2 reservoir. *Int. J. Greenh. Gas Control* 54, Part 1:70–83.

Bauer, R. A., M. Carney, and R. J. Finley. 2016. Overview of microseismic response to CO2 injection into the Mt. Simon saline reservoir at the Illinois Basin-Decatur Project. *Int. J. Greenh. Gas Control* 54:378–388.

Bemer, E., M. T. Nguyen, J. Dautriat, M. Adelinet, M. Fleury, and S. Youssef. 2016. Impact of chemical alteration on the poromechanical properties of carbonate rocks. *Geophys. Prospect.* 64:810–827.

Benson, P. M., S. Vinciguerra, P. G. Meredith, and R. P. Young. 2008. Laboratory Simulation of Volcano Seismicity. *Science (80-.).* 322:249–252.

Benson, S. M., and D. R. Cole. 2008. CO2 Sequestration in Deep Sedimentary

Formations. *Elements* 4:325–331.

Bhatnagar, P. L., E. P. Gross, and M. Krook. 1954. A Model for Collision Processes in Gases. I. Small Amplitude Processes in Charged and Neutral One-Component Systems. *Phys. Rev.* 94:511–525.

Bickle, M. J. 2009. Geological carbon storage. *Nat. Geosci.* 2:815.

Biot, M. A. 1941. General Theory of Three-Dimensional Consolidation. *J. Appl. Phys.* 12:155–164.

Biot, M. A. 1962. Mechanics of Deformation and Acoustic Propagation in Porous Media. *J. Appl. Phys.* 33:1482–1498.

Bolton, M. D., Y. Nakata, and Y. P. Cheng. 2008. Micro- and macro-mechanical behaviour of DEM crushable materials. *Géotechnique* 58:471–480.

Bower, A. F. 2009. Applied mechanics of solids. CRC press.

Byerlee, J. D. 1968. Brittle-ductile transition in rocks. *J. Geophys. Res.* 73:4741–4750.

Canal, J., J. Delgado, I. Falcón, Q. Yang, R. Juncosa, and V. Barrientos. 2012. Injection of CO2-saturated water through a siliceous sandstone plug from the Hontomin test site (Spain): experiment and modeling. *Environ. Sci. Technol.* 47:159–167.

Carrier, W. D. 2003. Goodbye, Hazen; Hello, Kozeny-Carman. *J. Geotech. Geoenvironmental Eng.* 129:1054–1056.

Carroll, S. a, W. W. McNab, and S. C. Torres. 2011. Experimental Study of Cement - Sandstone/Shale - Brine - CO2 Interactions. *Geochem. Trans.* 12:9.

Carroll, S., Y. Hao, M. Smith, and Y. Sholokhova. 2013. Development of scaling parameters to describe CO2–rock interactions within Weyburn-Midale carbonate flow units. *Int. J. Greenh. Gas Control* 16, Supple:S185–S193.

Cha, M., and J. C. Santamarina. 2014. Dissolution of randomly distributed soluble grains: post-dissolution k0-loading and shear. *Géotechnique* 64:828–836.

Chan, A. W.-K. 2004. Production-induced reservoir compaction, permeability loss and land surface subsidence. Stanford.

Chase Jr., C. A., and J. K. Dietrich. 1989. Compaction Within the South Belridge Diatomite. *SPE Reserv. Eng.* 4.

Cheng, Y. P., Y. Nakata, and M. D. Bolton. 2003. Discrete element simulation of

crushable soil. *Géotechnique* 53:633–641.

Cho, N. al, C. D. Martin, and D. C. Sego. 2007. A clumped particle model for rock. *Int. J. Rock Mech. Min. Sci.* 44:997–1010.

Chuhan, F. A., A. Kjeldstad, K. Bjørlykke, and K. Høeg. 2002. Porosity loss in sand by grain crushing—experimental evidence and relevance to reservoir quality. *Mar. Pet. Geol.* 19:39–53.

Ciantia, M. O., M. Arroyo, F. Calvetti, and A. Gens. 2015. An approach to enhance efficiency of DEM modelling of soils with crushable grains. *Géotechnique* 65:91–110.

Cil, M. B., and K. A. Alshibli. 2014. 3D evolution of sand fracture under 1D compression. *Géotechnique* 64:351–364.

Coussy, O. 2004. Poromechanics. John Wiley & Sons.

Cundall, P. A., and O. D. L. Strack. 1979. A discrete numerical model for granular assemblies. *Géotechnique* 29:47–65.

Daigle, H., N. W. Hayman, E. D. Kelly, K. L. Milliken, and H. Jiang. 2017. Fracture capture of organic pores in shales. *Geophys. Res. Lett.* 44:2167–2176.

Davies, J. P., and D. K. Davies. 2001. Stress-Dependent Permeability: Characterization and Modeling. *SPE J.* 6:224–235.

Detournay, E. 2004. Propagation regimes of fluid-driven fractures in impermeable rocks. *Int. J. Geomech.* 4:35–45.

DiMaggio, F. L., and I. S. Sandler. 1971. Material model for granular soils. *J. Eng. Mech.*

Dobrynin, V. M. 1962. Effect of Overburden Pressure on Some Properties Of Sandstones. *Soc. Pet. Eng. J.* 2:360–366.

Dong, H., and M. J. Blunt. 2009. Pore-network extraction from micro-computerized-tomography images. *Phys. Rev. E - Stat. Nonlinear, Soft Matter Phys.* 80:1–11.

Drucker, D. C., and W. Prager. 1952. Soil mechanics and plastic analysis or limit design. *Q. Appl. Math.* 10:157–165.

Duan, K., C. Y. Kwok, and M. Pierce. 2016. Discrete element method modeling of inherently anisotropic rocks under uniaxial compression loading. *Int. J. Numer. Anal. Methods Geomech.* 40:1150–1183.

Economides, M. J., and K. G. Nolte. 1989. Reservoir stimulation. Prentice Hall Englewood Cliffs, New Jersey.

Ergenzinger, C., R. Seifried, and P. Eberhard. 2011. A discrete element model to describe failure of strong rock in uniaxial compression. *Granul. Matter* 13:341–364.

Espinoza, D. N., H. Jung, J. R. Major, Z. Sun, M. J. Ramos, P. Eichhubl, M. T. Balhoff, R. C. Choens, and T. A. Dewers. 2018. CO2 charged brines changed rock strength and stiffness at Crystal Geyser, Utah: Implications for leaking subsurface CO2 storage reservoirs. *Int. J. Greenh. Gas Control* 73:16–28.

Espinoza, D. N., S. H. Kim, and J. C. Santamarina. 2011. CO2 geological storage --- Geotechnical implications. *KSCE J. Civ. Eng.* 15:707–719.

Fatt, I. 1958. Compressibility of Sandstones at Low to Moderate Pressures. *Am. Assoc. Pet. Geol. Bull.* 42:1924–1957.

Fatt, I., and D. H. Davis. 1952. Reduction in Permeability With Overburden Pressure. *J. Pet. Technol.* 4:16–16.

Feng, Y., J. F. Jones, and K. E. Gray. 2016. A Review on Fracture-Initiation and -Propagation Pressures for Lost Circulation and Wellbore Strengthening. *SPE Drill. Complet.* 31:134–144.

Fernandez, A. L., and J. C. Santamarina. 2001. Effect of cementation on the small-strain parameters of sands. *Can. Geotech. J.* 38:191–199.

Finol, A., and S. M. F. Ali. 1975. Numerical Simulation of Oil Production With Simultaneous Ground Subsidence. *Soc. Pet. Eng. J.* 15:411–424.

Fjar, E., R. M. Holt, A. M. Raaen, R. Risnes, and P. Horsrud. 2008. Petroleum related rock mechanics. Elsevier.

Fredrich, J. T., J. G. Arguello, G. L. Deitrick, and E. P. de Rouffignac. 2000. Geomechanical Modeling of Reservoir Compaction, Surface Subsidence, and Casing Damage at the Belridge Diatomite Field. *SPE Reserv. Eval. Eng.* 3:348–359.

Gallagher, J. J., M. Friedman, J. Handin, and G. M. Sowers. 1974. Experimental studies relating to microfracture in sandstone. *Tectonophysics* 21:203–247.

Geertsma, J. 1966. Problems of Rock Mechanics In Petroleum Production Engineering. *1st ISRM Congr.* International Society for Rock Mechanics, Lisbon, Portugal.

Germaine, J. T., and A. V Germaine. 2009. Geotechnical laboratory measurements for engineers. John Wiley & Sons.

Goulty, N. R. 2003. Reservoir stress path during depletion of Norwegian chalk oilfields. *Pet. Geosci.* 9:233–241.

Gowd, T. N., and F. Rummel. 1980. Effect of confining pressure on the fracture behaviour of a porous rock. *Int. J. Rock Mech. Min. Sci. Geomech. Abstr.* 17:225–229.

Griffith, A. A. 1921. VI. The phenomena of rupture and flow in solids. *Philos. Trans. R. Soc. london. Ser. A, Contain. Pap. a Math. or Phys. character* 221:163–198.

Le Guen, Y., F. Renard, R. Hellmann, E. Brosse, M. Collombet, D. Tisserand, and J.-P. Gratier. 2007. Enhanced deformation of limestone and sandstone in the presence of high P co2 fluids. *J. Geophys. Res.* 112.

Gunter, W. ., E. . Perkins, and I. Hutcheon. 2000. Aquifer disposal of acid gases: modelling of water–rock reactions for trapping of acid wastes. *Appl. Geochemistry* 15:1085–1095.

Hager, A., C. Kloss, S. Pirker, and C. Goniva. 2014. Parallel Resolved Open Source CFD-DEM: Method, Validation and Application. *J. Comput. Multiph. Flows* 6:13–27.

Han, Y., and P. A. Cundall. 2013. LBM–DEM modeling of fluid–solid interaction in porous media. *Int. J. Numer. Anal. Methods Geomech.* 37:1391–1407.

Hangx, S., E. Bakker, P. Bertier, G. Nover, and A. Busch. 2015. Chemical–mechanical coupling observed for depleted oil reservoirs subjected to long-term CO2-exposure – A case study of the Werkendam natural CO2 analogue field. *Earth Planet. Sci. Lett.* 428:230–242.

Hawkes, C. D., P. J. McLellan, and S. Bachu. 2005. Geomechanical Factors Affecting Geological Storage of CO2 in Depleted Oil and Gas Reservoirs. *J. Can. Pet. Technol.* 44:10.

Hazzard, J. F., and R. P. Young. 2004. Dynamic modelling of induced seismicity. *Int. J. Rock Mech. Min. Sci.* 41:1365–1376.

He, J., Y. Chen, L. Zhengchun, and R. Samuel. 2016. Global Correlation of Rock Brittleness Indices With Petrophysical and Geomechanical Properties and its Application to the Prediction of Rate of Penetration (ROP). *IADC/SPE Asia Pacific Drill. Technol. Conf.* Society of Petroleum Engineers.

He, Y., S. Cheng, L. Li, G. Mu, T. Zhang, H. Xu, J. Qin, and H. Yu. 2017. Waterflood Direction and Front Characterization With Four-Step Work Flow: A Case Study in Changqing Oil Field, China. *SPE Reserv. Eval. Eng.* 20:708–725.

Hernandez-Uribe, L. A., M. Aman, and D. N. Espinoza. 2017. Assessment of Mudrock Brittleness with Micro-scratch Testing. *Rock Mech. Rock Eng.* 50:2849–2860.

Hettema, M. H. H., P. M. T. M. Schutjens, B. J. M. Verboom, and H. J. Gussinklo. 2000. Production-Induced Compaction of a Sandstone Reservoir: The Strong Influence of Stress Path. *SPE Reserv. Eval. Eng.* 3:342–347.

Hobbs, D. W. 1964. The tensile strength of rocks. *Int. J. Rock Mech. Min. Sci. Geomech. Abstr.* 1:385–396. Elsevier.

Hoek, E., and Z. T. Bieniawski. 1965. Brittle fracture propagation in rock under compression. *Int. J. Fract. Mech.* 1:137–155.

Hoek, E., and C. D. Martin. 2014. Fracture initiation and propagation in intact rock – A review. *J. Rock Mech. Geotech. Eng.* 6:287–300.

Holloway, S., and D. Savage. 1993. The potential for aquifer disposal of carbon dioxide in the UK. *Energy Convers. Manag.* 34:925–932.

Hovorka, S. D., S. M. Benson, C. Doughty, B. M. Freifeild, S. Sakurai, T. M. Daley, Y. K. Kharaka, M. H. Holtz, R. C. Trautz, H. S. Nance, L. R. Myer, and K. G. Knauss. 2006. Measuring permanence of CO2 storage in saline formations: The Frio experiment. *Environ. Geosci.* 13:105–121.

Hovorka, S. D., T. A. Meckel, and R. H. Treviño. 2013. Monitoring a large-volume injection at Cranfield, Mississippi—Project design and recommendations. *Int. J. Greenh. Gas Control* 18:345–360.

Hsieh, Y.-M., H.-H. Li, T.-H. Huang, and F.-S. Jeng. 2008. Interpretations on how the macroscopic mechanical behavior of sandstone affected by microscopic properties—Revealed by bonded-particle model. *Eng. Geol.* 99:1–10.

Huang, H., B. Lecampion, and E. Detournay. 2013. Discrete element modeling of tool-rock interaction I: rock cutting. *Int. J. Numer. Anal. Methods Geomech.* 37:1913–1929.

Huang, H., F. Zhang, P. Callahan, and J. Ayoub. 2012a. Granular Fingering in Fluid Injection into Dense Granular Media in a Hele-Shaw Cell. *Phys. Rev. Lett.* 108:258001.

Huang, H., F. Zhang, P. Callahan, and J. A. Ayoub. 2012b. Fluid Injection Experiments in 2D Porous Media. *SPE J.* 17:903–911.

Huang, X., K. J. Hanley, C. O'Sullivan, and F. C. Y. Kwok. 2014. Effect of sample size on the response of DEM samples with a realistic grading. *Particuology* 15:107–115.

Hucka, V., and B. Das. 1974. Brittleness determination of rocks by different methods. *Int. J. Rock Mech. Min. Sci. Geomech. Abstr.* 11:389–392.

Jaeger, J. C. 1967. Failure of rocks under tensile conditions. *Int. J. Rock Mech. Min. Sci. Geomech. Abstr.* 4:219–227.

Jaeger, J. C., N. G. W. Cook, and R. Zimmerman. 2009. Fundamentals of rock mechanics. John Wiley & Sons.

Jiang, M., H.-S. Yu, and S. Leroueil. 2007. A simple and efficient approach to capturing bonding effect in naturally microstructured sands by discrete element method. *Int. J. Numer. Methods Eng.* 69:1158–1193.

Jing, L., and J. A. Hudson. 2002. Numerical methods in rock mechanics. *Int. J. Rock Mech. Min. Sci.* 39:409–427.

Jing, L., C. Y. Kwok, Y. F. Leung, and Y. D. Sobral. 2016. Extended CFD-DEM for free-surface flow with multi-size granules. *Int. J. Numer. Anal. Methods Geomech.* 40:62–79.

Johnson, K. L. 1970. The correlation of indentation experiments. *J. Mech. Phys. Solids* 18:115–126.

Jurgens, M. 2007. Development and testing of a discrete element model of crushing sand.

Kaszuba, J. P., D. R. Janecky, and M. G. Snow. 2005. Experimental evaluation of mixed fluid reactions between supercritical carbon dioxide and NaCl brine: Relevance to the integrity of a geologic carbon repository. *Chem. Geol.* 217:277–293.

Keehm, Y. 2003. Computational rock physics: Transport properties in porous media and applications.

Khodaverdian, M. F., T. Sorop, S. J. Postif, and P. J. Van den Hoek. 2010. Polymer Flooding in Unconsolidated-Sand Formations: Fracturing and Geomechanical Considerations. *SPE Prod. Oper.* 25:211–222.

Khodaverdian, M., and P. McElfresh. 2000. Hydraulic Fracturing Stimulation in Poorly Consolidated Sand: Mechanisms and Consequences. *SPE Annu. Tech. Conf. Exhib.*:13. Society of Petroleum Engineers, Dallas, Texas.

Kiichi, S., B. J. P., O. Masanobu, I. Kazuyoshi, T. Yutaka, T. Toshitsugu, and K. Toshihiro. 2007. Simulation of Upward Seepage Flow in a Single Column of Spheres Using Discrete-Element Method with Fluid-Particle Interaction. *J. Geotech. Geoenvironmental Eng.* 133:104–109.

Kim, S., and J. C. Santamarina. 2014. CO2 geological storage: hydro-chemo-mechanical analyses and implications. *Greenh. Gases Sci. Technol.* 4:528–543.

Kloss, C., C. Goniva, A. Hager, S. Amberger, and S. Pirker. 2012. Models, algorithms and validation for opensource DEM and CFD-DEM. *Prog. Comput. Fluid Dyn. an Int. J.* 12:140–152.

Kuhn, M. R., and K. Bagi. 2009. Specimen Size Effect in Discrete Element Simulations of Granular Assemblies. *J. Eng. Mech.* 135:485–492.

Kumar, V., C. H. Sondergeld, and C. S. Rai. 2012. Nano to Macro Mechanical Characterization of Shale. *SPE Annu. Tech. Conf. Exhib.* Society of Petroleum Engineers, San Antonio, Texas, USA.

Kutchko, B. G., B. R. Strazisar, G. V Lowry, D. A. Dzombak, and N. Thaulow. 2008. Rate of CO2 Attack on Hydrated Class H Well Cement under Geologic Sequestration Conditions. *Environ. Sci. Technol.* 42:6237–6242.

Kwok, C. Y., and M. D. Bolton. 2013. DEM simulations of soil creep due to particle crushing. *Géotechnique* 63:1365–1376.

Lake, L. W. 1989. Enhanced oil recovery.

Liang, Y., B. Wen, M. A. Hesse, and D. DiCarlo. 2018. Effect of Dispersion on Solutal Convection in Porous Media. *Geophys. Res. Lett.* 45:9690–9698.

Lisjak, A., and G. Grasselli. 2014. A review of discrete modeling techniques for fracturing processes in discontinuous rock masses. *J. Rock Mech. Geotech. Eng.* 6:301–314.

Liteanu, E., A. Niemeijer, C. J. Spiers, C. J. Peach, and J. H. P. de Bresser. 2012. The effect of CO2 on creep of wet calcite aggregates. *J. Geophys. Res. Solid Earth* 117.

Liu, Q., S. Tian, G. Li, M. Sheng, X. Li, T. Wang, and Z. Shen. 2018a. An analytical model for fracture initiation from radial lateral borehole. *J. Pet. Sci. Eng.* 164:206–218.

Liu, Q., S. Tian, Z. Shen, Z. Xu, and Z. Pang. 2018b. A new equation for predicting settling velocity of solid spheres in fiber containing power-law fluids. *Powder Technol.* 329:270–281.

Lockner, D. A., J. D. Byerlee, V. Kuksenko, A. Ponomarev, and A. Sidorin. 1991. Quasi-static fault growth and shear fracture energy in granite. *Nature* 350:39.

Lu, J., Y. K. Kharaka, J. J. Thordsen, J. Horita, A. Karamalidis, C. Griffith, J. A. Hakala,

G. Ambats, D. R. Cole, T. J. Phelps, M. A. Manning, P. J. Cook, and S. D. Hovorka. 2012. CO2–rock–brine interactions in Lower Tuscaloosa Formation at Cranfield CO2 sequestration site, Mississippi, U.S.A. *Chem. Geol.* 291:269–277.

Lu, M., and G. R. McDowell. 2006. Discrete element modelling of ballast abrasion. *Géotechnique* 56:651–655.

MacMinn, C. W., E. R. Dufresne, and J. S. Wettlaufer. 2015. Fluid-driven deformation of a soft granular material. *Phys. Rev. X* 5:11020.

Major, J. R., P. Eichhubl, T. A. Dewers, A. S. Urquhart, J. E. Olson, J. Holder, and others. 2014. The Effect of CO2-Related Diagenesis on Geomechanical Failure Parameters: Fracture Testing of CO2-Altered Reservoir and Seal Rocks From a Natural Analog at Crystal Geyser, Utah. *48th US Rock Mech. Symp.*

Marsh, Dm. 1964. Plastic flow in glass. *Proc. R. Soc. London. Ser. A. Math. Phys. Sci.* 279:420–435.

Mason, H. E., W. L. Du Frane, S. D. C. Walsh, Z. Dai, S. Charnvanichborikarn, and S. A. Carroll. 2013. Chemical and Mechanical Properties of Wellbore Cement Altered by CO2-Rich Brine Using a Multianalytical Approach. *Environ. Sci. Technol.* 47:1745–1752.

McDowell, G. R., and O. Harireche. 2002. Discrete element modelling of soil particle fracture. *Géotechnique* 52:131–135.

McLatchie, A. S., R. A. Hemstock, and J. W. Young. 1958. The Effective Compressibility of Reservoir Rock and Its Effects on Permeability. *J. Pet. Technol.* 10:49–51.

Meakin, P., and A. M. Tartakovsky. 2009. Modeling and simulation of pore-scale multiphase fluid flow and reactive transport in fractured and porous media. *Rev. Geophys.* 47.

Menéndez, B., W. Zhu, and T.-F. Wong. 1996. Micromechanics of brittle faulting and cataclastic flow in Berea sandstone. *J. Struct. Geol.* 18:1–16.

Meng, F., H. Zhou, and C. Zhang. 2015. Evaluation Methodology of Brittleness of Rock Based on Post-Peak Stress-Strain Curves. *Rock Mech. Rock Eng.*:1787–1805.

Michael, K., A. Globab, V. Shulakova, J. Ennis-King, G. Allinson, S. Sharma, and T. Aiken. 2010. Geological storage of CO2 in saline aquifers - A review of the experience from existing storage operations. *I J Greenh. Gas Control* 4.

Minh, N. H., and Y. P. Cheng. 2013. A DEM investigation of the effect of particle-size

distribution on one-dimensional compression. *Géotechnique* 63:44–53.

Mirabolghasemi, M. 2017. Micro-scale Modeling of Formation Damage. the University of Texas at Austin.

Mogi, K. 1966. Pressure dependence of rock strength and transition from brittle fracture to ductile flow. *Bull. Earthq. Res. Inst.* 44:215–232.

Mogi, K. 1971. Fracture and flow of rocks under high triaxial compression. *J. Geophys. Res.* 76:1255–1269.

Mondal, S., C.-H. Wu, and M. M. Sharma. 2016a. Coupled CFD-DEM simulation of hydrodynamic bridging at constrictions. *Int. J. Multiph. Flow* 84:245–263.

Mondal, S., C. H. Wu, and M. M. Sharma. 2016b. Coupled CFD-DEM simulation of hydrodynamic bridging at constrictions. *Int. J. Multiph. Flow* 84:245–263.

Nakata, A. F. L., M. Hyde, H. Hyodo, and Murata. 1999. A probabilistic approach to sand particle crushing in the triaxial test. *Géotechnique* 49:567–583.

Obermayr, M., K. Dressler, C. Vrettos, and P. Eberhard. 2013. A bonded-particle model for cemented sand. *Comput. Geotech.* 49:299–313.

Oliver, W. C., and G. M. Pharr. 2004. Measurement of hardness and elastic modulus by instrumented indentation: Advances in understanding and refinements to methodology. *J. Mater. Res.* 19:3–20.

Olson, J. E., J. Holder, and M. Hosseini. 2011. Soft Rock Fracturing Geometry And Failure Mode In Lab Experiments. *SPE Hydraul. Fract. Technol. Conf.*:9. Society of Petroleum Engineers, The Woodlands, Texas, USA.

Ostermeier, R. M. 1995. Deepwater Gulf of Mexico Turbidites - Compaction Effects on Porosity and Permeability. *SPE Form. Eval.* 10:79–85.

Park, B., and K.-B. Min. 2015. Bonded-particle discrete element modeling of mechanical behavior of transversely isotropic rock. *Int. J. Rock Mech. Min. Sci.* 76:243–255.

Petro, D. R., W.-C. Chu, M. K. Burk, and B. A. Rogers. 1997. Benefits of Pressure Transient Testing in Evaluating Compaction Effects: Gulf of Mexico Deepwater Turbidite Sands. *SPE Annu. Tech. Conf. Exhib.* Society of Petroleum Engineers, San Antonio, Texas.

Pokrovsky, O. S., S. V. Golubev, and J. Schott. 2005. Dissolution kinetics of calcite, dolomite and magnesite at 25 °C and 0 to 50 atm pCO2. *Chem. Geol.* 217:239–255.

Pollard, D. D. 1973. Derivation and evaluation of a mechanical model for sheet intrusions. *Tectonophysics* 19:233–269.

Potyondy, D. O. 2007. Simulating stress corrosion with a bonded-particle model for rock. *Int. J. Rock Mech. Min. Sci.* 44:677–691.

Potyondy, D. O., and P. A. Cundall. 2004. A bonded-particle model for rock. *Int. J. Rock Mech. Min. Sci.* 41:1329–1364.

Prodanović, M., and S. L. Bryant. 2006. A level set method for determining critical curvatures for drainage and imbibition. *J. Colloid Interface Sci.* 304:442–458.

Prodanović, M., J. T. Holder, and S. L. Bryant. 2012. Pore scale coupling of fluid displacement and unconsolidated sediment mechanics. *Int. J. Oil, Gas Coal Technol.* 5:157–181.

Pruess, K. 2008. Leakage of CO2 from geologic storage: Role of secondary accumulation at shallow depth. *Int. J. Greenh. Gas Control* 2:37–46.

Raeini, A. Q., M. J. Blunt, and B. Bijeljic. 2012. Modelling two-phase flow in porous media at the pore scale using the volume-of-fluid method. *J. Comput. Phys.* 231:5653–5668.

Rattia, A. J., and S. M. F. Ali. 1981. Effect of Formation Compaction on Steam Injection Response. *SPE Annu. Tech. Conf. Exhib.* Society of Petroleum Engineers, San Antonio, Texas.

Renard, F., E. Gundersen, R. Hellmann, M. Collombet, and Y. Le Guen. 2008. Numerical modeling of the effect of carbon dioxide sequestration on the rate of pressure solution creep in limestone: Preliminary results. *Oil gas Sci. Technol.* 60:381–399.

Rhett, D. W., and L. W. Teufel. 1992. Effect of Reservoir Stress Path on Compressibility and Permeability of Sandstones. *Annu. Tech. Conf. Exhib.* Society of Petroleum Engineers, Washington, DC.

Richard, T., F. Dagrain, E. Poyol, and E. Detournay. 2012. Rock strength determination from scratch tests. *Eng. Geol.* 147–148:91–100.

Richard, T., E. Detournay, A. Drescher, P. Nicodeme, and D. Fourmaintraux. 1998. The Scratch Test As A Means To Measure Strength of Sedimentary Rocks. *SPE/ISRM Rock Mech. Pet. Eng.* Society of Petroleum Engineers.

Rimmelé, G., V. Barlet-Gouédard, and F. Renard. 2010. Evolution of the Petrophysical and Mineralogical Properties of Two Reservoir Rocks Under Thermodynamic Conditions Relevant for CO 2 Geological Storage at 3 km Depth. *Oil Gas Sci.*

Technol. – Rev. l'Institut Français du Pétrole 65:565–580.

Rinehart, A. J., T. A. Dewers, S. T. Broome, and P. Eichhubl. 2016. Effects of CO2 on mechanical variability and constitutive behavior of the Lower Tuscaloosa Formation, Cranfield Injection Site, USA. *Int. J. Greenh. Gas Control* 53:305–318.

Robertson, D. 2000. Numerical simulations of crushable aggregates.

Rohmer, J., A. Pluymakers, and F. Renard. 2016. Mechano-chemical interactions in sedimentary rocks in the context of CO2 storage: Weak acid, weak effects? *Earth-Science Rev.* 157:86–110.

Rojek, J., E. Oñate, C. Labra, and H. Kargl. 2011. Discrete element simulation of rock cutting. *Int. J. Rock Mech. Min. Sci.* 48:996–1010.

Rubin, A. M. 1995. Propagation of Magma-Filled Cracks. *Annu. Rev. Earth Planet. Sci.* 23:287–336.

Rutqvist, J. 2012. The Geomechanics of CO2 Storage in Deep Sedimentary Formations. *Geotech. Geol. Eng.* 30:525–551.

Rutqvist, J., A. P. Rinaldi, F. Cappa, P. Jeanne, A. Mazzoldi, L. Urpi, Y. Guglielmi, and V. Vilarrasa. 2016. Fault activation and induced seismicity in geological carbon storage – Lessons learned from recent modeling studies. *J. Rock Mech. Geotech. Eng.* 8:789–804.

Rutqvist, J., and C.-F. Tsang. 2002. A study of caprock hydromechanical changes associated with CO2-injection into a brine formation. *Environ. Geol.* 42:296–305.

Rutqvist, J., D. W. Vasco, and L. Myer. 2010. Coupled reservoir-geomechanical analysis of CO2 injection and ground deformations at In Salah, Algeria. *I J Greenh. Gas Control* 4.

Rutqvist, J., Y.-S. Wu, C.-F. Tsang, and G. Bodvarsson. 2002. A modeling approach for analysis of coupled multiphase fluid flow, heat transfer, and deformation in fractured porous rock. *Int. J. Rock Mech. Min. Sci.* 39:429–442.

Schei, G., E. Fjær, E. Detournay, C. J. Kenter, G. F. Fuh, and F. Zausa. 2000. The Scratch Test: An Attractive Technique for Determining Strength and Elastic Properties of Sedimentary Rocks. *SPE Annu. Tech. Conf. Exhib.* Society of Petroleum Engineers.

Schellart, W. P. 2000. Shear test results for cohesion and friction coefficients for different granular materials: scaling implications for their usage in analogue modelling. *Tectonophysics* 324:1–16.

Segall, P. 1989. Earthquakes triggered by fluid extraction. *Geology* 17:942–946.

Segall, P., and S. D. Fitzgerald. 1998. A note on induced stress changes in hydrocarbon and geothermal reservoirs. *Tectonophysics* 289:117–128.

Settari, A. 2002. Reservoir Compaction. *J. Pet. Technol.* 54.

Settari, A., and D. A. Walters. 2001. Advances in Coupled Geomechanical and Reservoir Modeling With Applications to Reservoir Compaction. *SPE J.* 6:334–342.

Sheppard, A. P., R. M. Sok, H. Averdunk, V. B. Robins, and A. Ghous. 2006. Analysis of rock microstructure using high-resolution X-ray tomography. *Proc. Int. Symp. Soc. Core Anal.*

Shimizu, H., S. Murata, and T. Ishida. 2011. The distinct element analysis for hydraulic fracturing in hard rock considering fluid viscosity and particle size distribution. *Int. J. Rock Mech. Min. Sci.* 48:712–727.

Shin, H., and J. C. Santamarina. 2009. Mineral dissolution and the evolution of k 0. *J. Geotech. Geoenvironmental Eng.* 135:1141–1147.

Shin, H., and J. C. Santamarina. 2010. Fluid-driven fractures in uncemented sediments: Underlying particle-level processes. *Earth Planet. Sci. Lett.* 299:180–189.

Shin, H., J. C. Santamarina, and J. A. Cartwright. 2008. Contraction-driven shear failure in compacting uncemented sediments. *Geol.* 36:931–934.

Shirgaonkar, A. A., M. A. MacIver, and N. A. Patankar. 2009. A new mathematical formulation and fast algorithm for fully resolved simulation of self-propulsion. *J. Comput. Phys.* 228:2366–2390.

da Silva, F. V, G. F. Debande, C. A. Pereira, and B. Plischke. 1990. Casing Collapse Analysis Associated With Reservoir Compaction and Overburden Subsidence. *Eur. Pet. Conf.* Society of Petroleum Engineers, The Hague, Netherlands.

Stefanou, I., and J. Sulem. 2014. Chemically induced compaction bands: Triggering conditions and band thickness. *J. Geophys. Res. Solid Earth* 119:880–899.

Streit, J. E., and R. R. Hillis. 2004. Estimating fault stability and sustainable fluid pressures for underground storage of CO2 in porous rock. *Energy* 29:1445–1456.

Suarez-Rivera, R., J. Stenebråten, and F. Dagrain. 2002. Continuous Scratch Testing on Core Allows Effective Calibration of Log-Derived Mechanical Properties for Use in Sanding Prediction Evaluation. *SPE/ISRM Rock Mech. Conf.* Society of Petroleum Engineers.

Sulak, A. M., and J. Danielsen. 1988. Reservoir Aspects Of Ekofisk Subsidence. *Offshore Technol. Conf.* Houston, Texas.

Sun, Y., M. Aman, and D. N. Espinoza. 2016a. Assessment of mechanical rock alteration caused by CO 2--water mixtures using indentation and scratch experiments. *Int. J. Greenh. Gas Control* 45:9–17.

Sun, Y., and H. Huang. 2017. A DEM Strategy for Modeling Fluid Injection in an Unconsolidated Medium. *51st U.S. Rock Mech. Symp.* American Rock Mechanics Association, San Francisco, California, USA.

Sun, Z., M. T. Balhoff, and D. N. Espinoza. 2016b. Pore-Scale Modeling of the Effect of Cementation on Rock Indentation Test. *50th U.S. Rock Mech. Symp.* American Rock Mechanics Association, Houston, Texas.

Sun, Z., M. T. Balhoff, and D. N. Espinoza. 2018a. Fluid Injection Induced Fracture Initiation Based on a Resolved CFD-DEM Approach. *52nd US Rock Mech. Symp.* American Rock Mechanics Association.

Sun, Z., D. N. Espinoza, and M. T. Balhoff. 2016c. Discrete element modeling of indentation tests to investigate mechanisms of CO2-related chemomechanical rock alteration. *J. Geophys. Res. Solid Earth* 121:7867–7881.

Sun, Z., D. N. Espinoza, and M. T. Balhoff. 2018b. Reservoir rock chemo-mechanical alteration quantified by triaxial tests and implications to fracture reactivation. *Int. J. Rock Mech. Min. Sci.* 106:250–258.

Sun, Z., D. N. Espinoza, M. T. Balhoff, and T. A. Dewers. 2017. Discrete Element Modeling of Micro-scratch Tests: Investigation of Mechanisms of CO2 Alteration in Reservoir Rocks. *Rock Mech. Rock Eng.* 50:3337–3348.

Sun, Z., H. Tang, D. N. Espinoza, M. T. Balhoff, and J. E. Killough. 2018c. Pore-to Reservoir-Scale Modeling of Depletion-Induced Compaction and Implications on Production Rate. *SPE Annu. Tech. Conf. Exhib.* Society of Petroleum Engineers, Dallas, Texas, USA.

Sun, Z., H. Tang, D. N. Espinoza, M. T. Balhoff, and J. E. Killough. 2018d. Discrete element modeling of grain crushing and implications on reservoir compaction. *J. Pet. Sci. Eng.* 171:431–439.

Tang, H., J. E. Killough, Z. Heidari, and Z. Sun. 2017. A New Technique To Characterize Fracture Density by Use of Neutron Porosity Logs Enhanced by Electrically Transported Contrast Agents. *SPE J.* 22:1034–1045.

Taylor, J. M. 1950. Pore-Space Reduction in Sandstones. *Am. Assoc. Pet. Geol. Bull.*

34:701–716.

Teeuw, D. 1971. Prediction of Formation Compaction from Laboratory Compressibility Data. *Soc. Pet. Eng. J.* 11:263–271.

von Terzaghi, K. 1923. Die Berechnug der Durchlassigkeit des Tones aus dem Verlauf der hydromechanischen Spannungserscheinungen. *Sitzungsber. Akad. Wiss.(Wien). Math.-Naturwiss. Kl., Abt. Iia* 132:125–138.

Teufel, L. W., D. W. Rhett, and H. E. Farrell. 1991. Effect of Reservoir Depletion And Pore Pressure Drawdown On In Situ Stress And Deformation In the Ekofisk Field, North Sea. *32nd U.S. Symp. Rock Mech.* American Rock Mechanics Association, Norman, Oklahoma.

Thomas, E. C., and S. J. Stieber. 1975. The Distribution Of Shale In Sandstones And Its Effect Upon Porosity. *SPWLA 16th Annu. Logging Symp.*:15. Society of Petrophysicists and Well-Log Analysts, New Orleans, Louisiana.

Thomas, T. C., and F. O. Slate. 1963. Tensile bond strength between aggregate and cement paste or mortar. *J. Proc.* 60:465–486.

Thompson, K. E., C. S. Willson, C. D. White, S. Nyman, J. P. Bhattacharya, and A. H. Reed. 2008. Application of a new grain-based reconstruction algorithm to microtomography images for quantitative characterization and flow modeling. *SPE Annu. Tech. Conf.*

Thornton, C., K. K. Yin, and M. J. Adams. 1996. Numerical simulation of the impact fracture and fragmentation of agglomerates. *J. Phys. D. Appl. Phys.* 29:424.

Tong, S., and K. K. Mohanty. 2016. Proppant transport study in fractures with intersections. *Fuel* 181:463–477.

Tsang, C.-F., J. Birkholzer, and J. Rutqvist. 2008. A comparative review of hydrologic issues involved in geologic storage of CO2 and injection disposal of liquid waste. *Environ. Geol.* 54:1723–1737.

Tsoungui, O., D. Vallet, and J.-C. Charmet. 1999. Numerical model of crushing of grains inside two-dimensional granular materials. *Powder Technol.* 105:190–198.

Utili, S., and R. Nova. 2008. DEM analysis of bonded granular geomaterials. *Int. J. Numer. Anal. Methods Geomech.* 32:1997–2031.

Verdon, J. P., J.-M. Kendall, D. J. White, and D. A. Angus. 2011. Linking microseismic event observations with geomechanical models to minimise the risks of storing CO2 in geological formations. *Earth Planet. Sci. Lett.* 305:143–152.

Vilarrasa, V., and J. Carrera. 2015. Geologic carbon storage is unlikely to trigger large earthquakes and reactivate faults through which CO2 could leak. *Proc. Natl. Acad. Sci.* 112:5938–5943.

Walton, K. 1987. The effective elastic moduli of a random packing of spheres. *J. Mech. Phys. Solids* 35:213–226.

Wang, C., D. Elsworth, and Y. Fang. 2017. Influence of weakening minerals on ensemble strength and slip stability of faults. *J. Geophys. Res. Solid Earth* 122:7090–7110.

Wang, Y.-H., and S.-C. Leung. 2008. A particulate-scale investigation of cemented sand behavior. *Can. Geotech. J.* 45:29–44.

Wang, Y., and F. Alonso-Marroquin. 2009. A finite deformation method for discrete modeling: particle rotation and parameter calibration. *Granul. Matter* 11:331–343.

White, D. 2009. Monitoring CO2 storage during EOR at the Weyburn-Midale Field. *Lead. Edge* 28:838–842.

White, W. B., D. C. Culver, J. S. Herman, T. C. Kane, and J. E. Mylroie. 1995. Karst lands. *Am. Sci.*:450–459.

Wigley, M., N. Kampman, B. Dubacq, and M. Bickle. 2012. Fluid-mineral reactions and trace metal mobilization in an exhumed natural CO2 reservoir, Green River, Utah. *Geology* 40:555–558.

Wong, T., C. David, and W. Zhu. 1997. The transition from brittle faulting to cataclastic flow in porous sandstones: Mechanical deformation. *J. Geophys. Res. Solid Earth* 102:3009–3025.

Wong, T. F., and P. Baud. 1999. Mechanical Compaction of Porous Sandstone. *Oil Gas Sci. Technol. - Rev. IFP* 54:715–727.

Wredenberg, F., and P.-L. Larsson. 2009. Scratch testing of metals and polymers: Experiments and numerics. *Wear* 266:76–83.

Yang, H. 2018. Pore-scale modeling of particle filtration in porous media.

Yang, Y., H. Sone, A. Hows, and M. D. Zoback. 2013. Comparison of Brittleness Indices in Organic-rich Shale Formations. *47th U.S. Rock Mech. Symp.* American Rock Mechanics Association.

Yew, C. H., and X. Weng. 2014. Mechanics of hydraulic fracturing. Gulf Professional Publishing.

Zhai, Z., and M. M. Sharma. 2005. A New Approach to Modeling Hydraulic Fractures in Unconsolidated Sands. *SPE Annu. Tech. Conf. Exhib.*:14. Society of Petroleum Engineers, Dallas, Texas.

Zhang, F., B. Damjanac, and H. Huang. 2013. Coupled discrete element modeling of fluid injection into dense granular media. *J. Geophys. Res. Solid Earth* 118:2703–2722.

Zhang, F., H. Huang, and V. Vajdova. 2011. Discrete Element Modeling of Sphere Indentation In Rocks. *45th U.S. Rock Mech. / Geomech. Symp.*:9. American Rock Mechanics Association, San Francisco, California.

Zhang, J., T.-F. Wong, and D. M. Davis. 1990. Micromechanics of pressure-induced grain crushing in porous rocks. *J. Geophys. Res. Solid Earth* 95:341–352.

Zhang, R., X. Yin, P. H. Winterfeld, and Y.-S. Wu. 2016. A fully coupled thermal-hydrological-mechanical-chemical model for CO2 geological sequestration. *J. Nat. Gas Sci. Eng.* 28:280–304.

Zhang, X.-P., and L. N. Y. Wong. 2012. Cracking processes in rock-like material containing a single flaw under uniaxial compression: a numerical study based on parallel bonded-particle model approach. *Rock Mech. Rock Eng.* 45:711–737.

Zhao, Z., and E. Song. 2015. Particle mechanics modeling of creep behavior of rockfill materials under dry and wet conditions. *Comput. Geotech.* 68:137–146.

Zheng, X., Z. Sun, and D. N. Espinoza. 2019. Uniaxial strain unloading compressibility of Frio Sand: measurements and implications on reservoir pressure management for CO2 storage. *53rd U.S. Rock Mech. Symp.* American Rock Mechanics Association, New York, NY, USA.

Zhou, J., M. Chen, Y. Jin, and G. Zhang. 2008. Analysis of fracture propagation behavior and fracture geometry using a tri-axial fracturing system in naturally fractured reservoirs. *Int. J. Rock Mech. Min. Sci.* 45:1143–1152.

Zhou, R., L. Huang, and J. Rutledge. 2010. Microseismic event location for monitoring CO2 injection using double-difference tomography. *Lead. Edge* 29:208–214.

Zhou, W., L. Yang, G. Ma, X. Chang, Z. Lai, and K. Xu. 2016. DEM analysis of the size effects on the behavior of crushable granular materials. *Granul. Matter* 18:64.

Zhu, H. P., Z. Y. Zhou, R. Y. Yang, and A. B. Yu. 2007. Discrete particle simulation of particulate systems: Theoretical developments. *Chem. Eng. Sci.* 62:3378–3396.

Zinsmeister, L., J. Dautriat, A. Dimanov, J. Raphanel, and M. Bornert. 2013. Mechanical

Evolution of an Altered Limestone Using 2D and 3D Digital Image Correlation (DIC). *47th US Rock Mech. Symp.* American Rock Mechanics Association.

Zoback, M. D., and S. M. Gorelick. 2012. Earthquake triggering and large-scale geologic storage of carbon dioxide. *Proc. Natl. Acad. Sci.* 109:10164–10168.